

---

**Master thesis and internship[BR]- Master's Thesis : Study of the wear behavior of SS316L + WC composites : role of the counter material[BR]- Stage d'insertion professionnelle**

**Auteur :** Serrano Martin, Iñigo

**Promoteur(s) :** Mertens, Anne

**Faculté :** Faculté des Sciences appliquées

**Diplôme :** Cours supplémentaires destinés aux étudiants d'échange (Erasmus, ...)

**Année académique :** 2019-2020

**URI/URL :** <http://hdl.handle.net/2268.2/9971>

---

*Avertissement à l'attention des usagers :*

*Tous les documents placés en accès ouvert sur le site le site MatheO sont protégés par le droit d'auteur. Conformément aux principes énoncés par la "Budapest Open Access Initiative"(BOAI, 2002), l'utilisateur du site peut lire, télécharger, copier, transmettre, imprimer, chercher ou faire un lien vers le texte intégral de ces documents, les disséquer pour les indexer, s'en servir de données pour un logiciel, ou s'en servir à toute autre fin légale (ou prévue par la réglementation relative au droit d'auteur). Toute utilisation du document à des fins commerciales est strictement interdite.*

*Par ailleurs, l'utilisateur s'engage à respecter les droits moraux de l'auteur, principalement le droit à l'intégrité de l'oeuvre et le droit de paternité et ce dans toute utilisation que l'utilisateur entreprend. Ainsi, à titre d'exemple, lorsqu'il reproduira un document par extrait ou dans son intégralité, l'utilisateur citera de manière complète les sources telles que mentionnées ci-dessus. Toute utilisation non explicitement autorisée ci-avant (telle que par exemple, la modification du document ou son résumé) nécessite l'autorisation préalable et expresse des auteurs ou de leurs ayants droit.*

---

# Graduation Studies conducted for obtaining the Master's degree in Aerospace Engineering

**Université de Liège – Universidad del País Vasco**

**Faculté des Sciences Appliquées – Escuela de Ingeniería de Bilbao**

## **MASTER THESIS**

***STUDY OF THE WEAR BEHAVIOR OF SS316L +  
WC COMPOSITES: ROLE OF THE COUNTER  
MATERIAL***

<b>Student</b>	<i>Serrano Martín, Iñigo</i>
<b>Supervisor</b>	<i>Mertens, Anne</i>
<b>Department</b>	<i>Metallic Materials Science, Aerospace and Mechanical Dpt.</i>
<b>Academic year</b>	<i>2019-2020</i>

*Liège, 20<sup>th</sup> August 2020*

## ABSTRACT

The present study focuses on the wear behavior of a laser cladded 316L + 20% WC. Preliminary microstructural characterization was carried out by means of SEM (morphology) and OM (distribution) in order to evaluate how the reinforcement WC particles are embedded into the steel parent matrix. Furthermore, hardness measurements were performed. A pin-on-disc tribometer test campaign was performed considering two different heights of a thick deposit. These results and post-mortem track analysis lead to a deeper comprehension of the wear behavior of the MMC and its wear sequence was elucidated. In addition, a comparison with the previous studies have been made, assessing the role of the counter body on the wear behavior of this complex MMC.

## LIST OF CONTENTS

<b>1</b>	<b>INTRODUCTION.....</b>	<b>12</b>
<b>2</b>	<b>STATE OF THE ART.....</b>	<b>14</b>
2.1	ADDITIVE MANUFACTURING .....	14
2.1.1	<i>Additive manufacturing techniques .....</i>	<i>15</i>
2.1.1.1	Electron Beam Melting .....	15
2.1.1.2	Selective Laser Melting.....	16
2.1.1.3	Laser Metal Deposition.....	17
2.2	COMPOSITE MATERIALS.....	20
2.2.1	<i>Metal Matrix Composites .....</i>	<i>21</i>
2.3	USED MATERIALS .....	22
2.3.1	<i>Stainless Steel 316L.....</i>	<i>22</i>
2.3.2	<i>Tungsten Carbide – WC .....</i>	<i>24</i>
2.4	MICROSTRUCTURE OF LASER CLADDED SS316L + WC .....	27
2.4.1	<i>Microstructure of laser cladded SS316L .....</i>	<i>27</i>
2.4.2	<i>Microstructure of laser cladded SS316L with WC addition .....</i>	<i>29</i>
2.5	WEAR OF MATERIALS.....	35
2.5.1	<i>Types of wear.....</i>	<i>35</i>
2.5.1.1	Abrasive wear .....	35
2.5.1.2	Adhesive wear .....	37
2.5.1.3	Corrosive and oxidative wear .....	39
2.5.1.4	Erosive wear .....	43
2.5.1.5	Fatigue wear .....	44
2.5.1.6	Cavitation wear.....	46
2.5.2	<i>Literature review of wear resistance improvement .....</i>	<i>47</i>
2.5.3	<i>Wear testing methods .....</i>	<i>50</i>
2.5.3.1	Pin-on-disk .....	51
2.5.3.2	Four ball tester .....	51
2.5.3.3	Reciprocating sliding friction .....	52
2.5.3.4	Fretting wear testing machine .....	52

<b>3</b>	<b>MATERIALS AND METHODS.....</b>	<b>54</b>
3.1	SAMPLES.....	54
3.1.1	<i>Samples preparation for microstructural characterization.....</i>	<i>55</i>
3.2	OPTICAL MICROSCOPE.....	56
3.3	SCANNING ELECTRON MICROSCOPE .....	57
3.4	PROFILOMETER.....	58
3.5	HARDNESS TESTING MACHINE.....	59
3.6	TRIBOMETER.....	60
<b>4</b>	<b>RESULTS.....</b>	<b>63</b>
4.1	MICROSTRUCTURE CHARACTERIZATION .....	63
4.1.1	<i>Optical microscopy .....</i>	<i>63</i>
4.1.2	<i>Scanning Electron Microscopy.....</i>	<i>66</i>
4.2	MACRO HARDNESS TEST .....	70
4.3	WEAR TESTS .....	71
4.3.1	<i>Tribometer analysis .....</i>	<i>71</i>
4.3.1.1	Uninterrupted tests.....	71
4.3.1.1.1	10N tests.....	71
4.3.1.1.2	20N Uninterrupted test .....	74
4.3.1.2	Interrupted tests.....	75
4.3.2	<i>Profilometer analysis.....</i>	<i>77</i>
4.3.2.1	Worn tracks .....	77
4.3.2.2	Worn balls.....	84
4.3.3	<i>SEM images .....</i>	<i>86</i>
4.3.3.1	W20.15 H6.3 11mm – Stopped at 4817 laps.....	87
4.3.3.2	W20.15 F1.3 11mm – Stopped at 5629 laps .....	91
4.3.3.3	W20.15 H6.3 8mm – Stopped at 10855 laps.....	94
4.3.3.4	W20.18 H6.3 8mm – Uninterrupted test .....	100
4.3.3.5	W20.15 F1.3 8mm – Uninterrupted test.....	103
4.3.3.6	W20.18 H6.3 11mm – Uninterrupted test – 20N.....	105
<b>5</b>	<b>DISCUSSION .....</b>	<b>107</b>

5.1	INFLUENCE OF THE COUNTERPART ON THE WEAR BEHAVIOR.....	107
5.2	ELUCIDATION OF THE WEAR SEQUENCE.....	110
<b>6</b>	<b>CONCLUSIONS.....</b>	<b>116</b>
<b>7</b>	<b>PERSPECTIVES.....</b>	<b>118</b>
<b>8</b>	<b>REFERENCES.....</b>	<b>119</b>

## LIST OF FIGURES

Figure 1. Electron Beam Melting scheme [8] .....	16
Figure 2. Selective Laser Melting scheme [9] .....	16
Figure 3. Different configurations of Laser Metal Deposition. a) Lateral powder injector. b) Discrete coaxial nozzle. c) Continuous coaxial nozzle. [15] .....	17
Figure 4. Lateral overlap between tracks [19].....	19
Figure 5. Laser Metal Deposition scheme. Detail on powder flow, gas flow and laser focusing. Coaxial and lateral nozzles [4].....	20
Figure 6. Example of combination of strength-elongation in a proper composite [24].	21
Figure 7. W-C phase diagram [34] .....	25
Figure 8. W-C present phases. a) Higher $\delta$ -WC hexagonal structure. b) Hexagonal structure of the $\beta$ -W <sub>2</sub> C carbide. Tungsten atoms ( ) form a hcp hexagonal structure and carbon atoms occupy grey interstitial spots ( ) with a probability of 1/2. c) Cubic structure of the $\gamma$ -WC <sub>1-x</sub> carbide [35] .....	26
Figure 9. a) Optical macrostructure of a laser deposited SS316L. [39] b) Arc-shaped forms. Different tracks can be observed [42]. c) Fine and columnar cells [39]. d) Dislocations located in subgrain cell boundaries [41]. e) Segregation of heavy additive elements of 316L steel [43] .....	28
Figure 10. a) Different microstructure and microhardness within a single track. b) Heat flux and consequent solidification of a track [40] .....	29
Figure 11. Morphology of eutectic M <sub>6</sub> C carbides [48] .....	31
Figure 12. Morphology and classification of M <sub>2</sub> C eutectic carbides [47] .....	31
Figure 13. Morphology and classification of MC eutectic carbides [47] .....	32
Figure 14. Morphology of M <sub>7</sub> C <sub>3</sub> carbides [51].....	33
Figure 15. M <sub>23</sub> C <sub>6</sub> carbide distribution in grain boundaries of two samples of 316L [52] .....	33
Figure 16. a) SEM obtained microstructure of 316L+20%WC composite.. White WC carbides embedded into the reinforced matrix. b) Overview of a localized WC carbides showing the transition zones (TZ). c) Magnification of the TZ of b) showing the solidification carbides coming from the partially dissolved WC particulate. d) Higher magnification showing the lamellar structure of the carbides and the carbide crown created near the WC particulate. [53].....	34
Figure 17. Abrasive wear mechanisms. a) Cutting. b) Fracture. c) Ploughing. d) Grain pull-out. [54].....	36
Figure 18. Abrasive wear mechanisms seen by SEM. a) Cutting. b) Wedge-forming. c) Ploughing. [55].....	36
Figure 19. Two-body abrasive wear scheme [54] .....	37

Figure 20. Three-body abrasive wear scheme [54] .....	37
Figure 21. Adhesive wear scheme [55] .....	38
Figure 22. i) Progressive adhesive wear stages. ii) Growth of transfer particle with mix of debris of two surfaces [56].....	39
Figure 23. Four possible behavior of corrosive wear [57].....	40
Figure 24. Oxidative wear scheme [57].....	41
Figure 25. Oxidative wear stages. a) Formation of plateaus. b) Oxide development on plateaus. c) Oxide expansion. d) Oxide breaking up to form wear debris. [58] .....	42
Figure 26. Oxidative wear stages at slow sliding speeds [57] .....	43
Figure 27. Possible mechanisms of erosive wear. a) Abrasion at low impact angles. b) Crack formation due to high angle impact and low speed. c) Plastic deformation or brittle breakage due to high angle impact and a considerable speed. d) Melting of the surface due to high speed impacts. e) Effect of the large particle in an erosive impact. f) Effect of tiny particle in erosive impact (atoms impact), atomic erosion. [54] .....	44
Figure 28. Wave-shaped plastic deformation caused by continuous sliding in early stages of fatigue wear [59] .....	45
Figure 29. Crack formation and propagation mechanism due to wave-shaped plastic deformation [58] .....	45
Figure 30. Cavitation phenomena [61].....	46
Figure 31. Different stages of a cavitation damage in a surface at different times. a) 1h. b) 3h. c) 5h. d) 8h. [62] .....	47
Figure 32. Carbide particles. a) After cladding. b) After machining. c) After first wear test [73].....	50
Figure 33. Pin-on-disk testing machine scheme [76] .....	51
Figure 34. Four ball tester scheme [77].....	52
Figure 35. Reciprocating sliding test scheme. Data specific of [78] .....	52
Figure 36. Fretting wear testing machine scheme. Data specific of [79].....	53
Figure 37. Zigzag technique used for samples fabrication [4] .....	55
Figure 38. a) Struers CitoPress-1. b) Struers Tergamin-30 [81].....	56
Figure 39. Olympus BX60 optical microscope [82].....	56
Figure 40. Philips XL30 ESEM FEG. Courtesy of <a href="https://www.mtm.kuleuven.be/equipment/ESEM-XL30-FEG/ESEM-XL30-FEG">https://www.mtm.kuleuven.be/equipment/ESEM-XL30-FEG/ESEM-XL30-FEG</a> .....	57
Figure 41. Alicona InfiniteFocus G5 plus profilometer [84] .....	58
Figure 42. EMCO Test M1C010 hardness testing machine [85].....	59
Figure 43. Sample denomination system. Obtained from [1].....	60
Figure 44. HTH Tribometer 01-04611. Obtained from [1] .....	62



Figure 45. W20.24 section 3 sample after macro hardness test. 5x overview via OM..	63
Figure 46. Layers 1, 2 and 3 on W20.24 section 3. 2.5x magnification .....	64
Figure 47. 5x overview in upper layers on W20.24 section 3 .....	65
Figure 48. "Traffic jam" of big WC particles in 17th layer .....	65
Figure 49. "Carbide tails" observable via 10x magnification on W20.24 section 3 .....	66
Figure 50. a) SEM micrograph related to Figure 46. High carbide density can be observed on the 2nd layer. b) SEM micrograph of W20.24 section 3 of upper layers showing more homogenization in WC carbides.....	66
Figure 51. Carbides distribution from the carbide crown to the outside part of the transition zone.....	67
Figure 52. HAZ carbides differentiation .....	68
Figure 53. SEM micrograph of a traffic jam of carbides area.....	69
Figure 54. Carbide tails observable by SEM micrograph.....	69
Figure 55. Macro hardness test results for W20.24 section 3 .....	70
Figure 56. Interest points chosen for posterior tests. Based upon W20.18 H6.3 8mm	71
Figure 57. Coefficient of friction and penetration depth for W20.15 F1.3 8mm.....	73
Figure 58. Coefficient of friction and penetration depth for W20.18 H6.3 11mm.....	74
Figure 59. Coefficient of friction and penetration depth for W20.15 H6.3 11mm.....	75
Figure 60. Coefficient of friction and penetration depth for W20.15 F1.3 11mm.....	76
Figure 61. Coefficient of friction and penetration depth for W20.15 H6.3 8mm.....	76
Figure 62. W20.18 H6.3 worn tracks (8 and 11mm) overview.....	77
Figure 63. W20.18 H6.3 8mm worn track 3D overview .....	78
Figure 64. W20.18 H6.3 11mm worn track 3D overview .....	78
Figure 65. W20.15 F1.3 worn tracks (8 and 11mm) overview .....	79
Figure 66. W20.15 F1.3 8mm worn track 3D overview.....	80
Figure 67. W20.15 F1.3 11mm worn track 3D overview.....	80
Figure 68. W20.15 H6.3 worn tracks (8 and 11mm) overview.....	81
Figure 69. W20.15 H6.3 8mm worn track 3D overview .....	82
Figure 70. W20.15 H6.3 11mm worn track 3D overview .....	82
Figure 71. Worn volume of tracks as a function of duration of the test.....	83
Figure 72. Wear rate of tracks as a function of the duration of the test .....	84
Figure 73. Calibration of the shape of worn balls .....	85
Figure 74. Worn balls volume as a function of the duration of the test.....	86

Figure 75. W20.15 H6.3 11mm (Int. at 4817 laps) worn track obtained by a) BSE and by b) SE. ....	87
Figure 76. Mechanical Mixed Layer observation on W20.15 H6.3 11mm .....	88
Figure 77. Different track width observed obtained by a) BSE and b) SE modes .....	90
Figure 78. Early tribolayer signs on W20.15 H6.3 11mm. Spectra rectangles 03 and 04 for chemical composition .....	91
Figure 79. Magnification on a debris zone on one side of the track of W20.15 F1.3 11mm.....	92
Figure 80. Magnification on different type of oxidized debris on W20.15 F1.3 11mm by a) BSE and b) SE modes .....	93
Figure 81. Plastic deformation and delamination on W20.15 F1.3 11mm .....	94
Figure 82. General overview of the W20.15 H6.3 8mm track.....	95
Figure 83. Magnification of a hole in front of the solidification carbides.....	96
Figure 84. Compact tribolayer observation on W20.15 H6.3 8mm .....	97
Figure 85. Spectra points in the tribolayer observation on W20.15 H6.3 8mm .....	97
Figure 86. Composition zones of different parts of the mix of debris and tribolayer present on W20.15 H6.3 8mm .....	98
Figure 87. Cracked carbide observation.....	99
Figure 88. Track overview on W20.18 H6.3 8mm .....	100
Figure 89. Two carbides magnification. a) BSE and b) SE modes of a cracked carbide with a hole in front. c) BSE and d) SE modes of a carbide with a hole in front.....	101
Figure 90. Track width change overview along with a tribolayer overview .....	101
Figure 91. Cracked tribolayer observation with b) 4 points selected for composition	102
Figure 92. Delamination sign on W20.18 H6.3 8mm .....	103
Figure 93. a) Track overview. b) Magnification on a carbide showing the path of the three-body abrasion .....	103
Figure 94. Composition map of a hole in front of a solidification carbide.....	104
Figure 95. Tribolayer zones for chemical composition analysis.....	105
Figure 96. Track overview in different areas in both a) & c) in SE mode and b) & d) in BSE mode.....	106
Figure 97. Coarse and fine debris on W20.18 H6.3 11mm track side.....	106
Figure 98. Worn volume as a function of the duration of the test, with D. Mario's uninterrupted test [1] (W20.14 F6.3 11mm) .....	108
Figure 99. Wear rate as a function of the duration the test, with D. Mario's uninterrupted test [1] (W20.14 F6.3 11mm) .....	108

Figure 100. Wear sequence for F faces (Based on W20.15 F1.3 8mm and W20.15 F1.3 11mm)..... 111

Figure 101. Wear sequence for H faces (Based on W20.15 H6.3 11mm, W20.15 H6.3 8mm and W20.18 H6.3 8mm) ..... 113

## LIST OF TABLES

Table 1. Chemical composition of 316 & 316L stainless steels [31].....	23
Table 2. SS316L properties [32].....	24
Table 3. WC properties [32].....	26
Table 4. 316L powder chemical composition in wt% [1,80].....	54
Table 5. WC powder chemical composition in wt% [1,80].....	54
Table 6. Samples fabrication process parameters and final characteristics .....	55
Table 7. Preliminary tribometer parameters of wear tests .....	61
Table 8. Worn volume of tracks obtained by the profilometer. NOTE: W20.18 H6.3 11mm belongs to the 20N test.....	83
Table 9. Worn volume of WC balls obtained by the profilometer. W20.18 H6.3 11mm belongs to the 20N test .....	85
Table 10. Chemical composition in wt% obtained from 4 points on Figure 66 .....	89
Table 11. Chemical composition in wt% of 03 and 04 rectangles from Figure 68 .....	91
Table 12. Chemical composition in wt% of 01 2, 01 3, 01 4 and 01 5 rectangles in Figure 79 .....	93
Table 13. Chemical composition in wt% of 01 and 02 rectangles on Figure 80.....	94
Table 14. Chemical composition in wt% of 01, 02, 03, 04 and 05 rectangles in Figure 75 .....	98
Table 15. Chemical composition in wt% of zones 01, 02, 03 and 05 selected on Figure 76 .....	99
Table 16. Chemical composition in wt% of points 1, 2, 3 and 4 from Figure 91b.....	102
Table 17. Chemical composition in wt% for zones selected on Figure 85 .....	105

## 1 INTRODUCTION

Additive manufacturing (AM) is a relatively modern technique that has been emerging to fulfill new industries' requirements. New challenges need newer techniques for better part reliability. It has some advantages over the traditional techniques such as one-step manufacturing and complex geometries manufacturing. Consequently, aerospace, automotive, energy, biomedical and other industries have pushed the development throughout the last years. More homogeneous finishes and better post-manufactured quality result in better parts reliability during service. An improved repairability is also introduced with AM allowing a better part maintenance. Furthermore, enhanced mechanical properties can be achieved by these technologies due to high cooling rates and thus refined microstructure in comparison to traditional means.

Currently only few alloys are only used for AM such as TiAl6V4, Inconel 718, some stainless steels and AlSi10Mg. Most of the traditional alloys do not withstand additive manufacturing requirements since parts manufactured with these materials exhibit cracks, low mechanical properties or the feedstock is complicated to obtain. However, materials researchers and metallurgists around the world are focusing on the development of new materials and composites in order to exploit these technologies on the materials science point of view. Here composites arise as the possible short-time new solutions for AM fabricated parts, and specifically Metal Matrix Composites (MMC). Among the many technologies in the market, Laser Metal Deposition (LMD) or laser cladding, among AM techniques, is particularly suitable for the MMC fabrication. Indeed, multiple powder feeds are allowed in laser cladding, enabling an exact compounds quantity varying the process parameters. These MMCs may improve classical alloys fabricated by AM, hence achieving parts with better mechanical properties such as hardness, corrosion resistance and wear resistance. 316L Stainless Steel, which is widely used in many engineering approaches from biomedical, energy to aerospace, civil and automotive industries. Hard ceramic particles as WC, TiC and SiC are being introduced as the reinforcement for 316L that enhance its hardness along with its weak wear resistance.

The purpose of his thesis is to assess the role of the counter body on the wear behavior of a laser clad 316L + 20% WC deposit. Preliminary microstructural and mechanical characterization were performed in order to know how the reinforcement affects to the parent steel changing its mechanical properties. Based on previous works (that use alumina balls as counterpart) [1,2] and pin-on-disc test campaign using WC balls as counterpart, better comprehension on how the material is behaving with respect to the counterpart is achieved. Scanning Electron Microscopy and Optical Microscopy were used to recognize the wear features in the post-mortem samples along with profilometer analysis to obtain their worn volume. After comparing the results in respect to the counterpart, the wear stages of the material were elucidated.

## 2 STATE OF THE ART

### 2.1 Additive manufacturing

Additive manufacturing (AM) is the process of making objects by joining materials from 3D precomputed data. This is obtained forming multiple layers which finally conform the desired shape. In opposition to traditional manufacturing techniques, where material is removed in order to obtain the final shape, AM provides the creation of the object from scratch. Currently it can be included into the Industry 4.0, as new methodologies – Big Data analysis, cloud computing etc. – for manufacturing from which the traditional industry can evolve into the fourth industrial revolution. These innovative techniques provide such type of pieces that are required in several industries such as automotive, aerospace, biomedical, energy... [3]. This process has already replaced traditional manufacturing in those areas as they require special characteristics only achievable by modern means. In this respect, there are several advantages seized by these industries, which implies an optimization in the process and in the product. Reduction in process time, manufacturing of complex geometries (holes, curved surfaces etc.), less waste of material and economic resources and elaboration of smart structures – embedding sensors inside the object, for example – are among these advantages [4]. Besides, it can provide a unique step of multi-material fabrication.

Concerning AM of metals and its derivatives (alloys and metal matrix composites – MMC), it provides different properties compared to the ones obtained by the traditional subtractive manufacturing techniques. Therefore, a good knowledge of the process parameters and the obtained results is required to achieve a compromise between them. For instance, high solidification rate is an intrinsic characteristic related to AM and it can achieve cooling rates  $>10^6$  K/s depending on the method used [5]. Whereas by traditional means these cooling rates are very difficult to achieve, the properties of parts obtained by AM change, resulting in improvements in mechanical properties caused by microstructural differences. By different AM techniques different results are obtained, thus good comprehension of the process is required.

### 2.1.1 Additive manufacturing techniques

Several techniques have been used today in AM of metals which are based on different technologies available. These technologies have evolved until today and three remain as the main ones: powder bed and powder feed systems and wire feed systems [6]. In this respect, three main techniques are the ones that are used the most nowadays and the ones which are being developed and investigated in numerous universities and institutes through the scientific community. These are Laser Metal Deposition (LMD) or Laser Cladding, Electron Beam Melting (EBM) and Selective Laser Melting (SLM) [3].

#### 2.1.1.1 Electron Beam Melting

It is based on the powder bed principle. Powder hoppers feed the metallic powder and a rake or a roller (depending on the design of the machine) distributes it across the flat surface. This is called the *powder bed*, which is situated inside a vacuum chamber in order to avoid oxidizing environments. An electron beam is focused in the powder bed thanks to an optic system and it scans the surface following the CAD file introduced into the computer of the machine. A fine layer is melted and then solidified. Immediately after the building plate is descended and the powder hoppers introduce new powder to the chamber. The process is repeated until the final shape is achieved. In this respect, the principal advantages of this process are the following ones:

- The vacuum chamber provides almost an inert environment where oxidation is less possible to occur.
- The powder that is not melted can be reused, but it has to be recycled with newer powder [7].



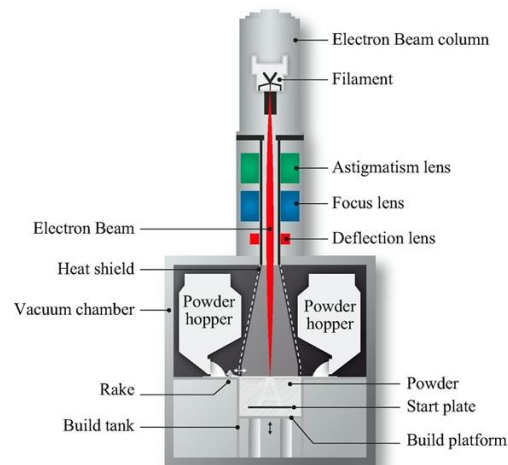


Figure 1. Electron Beam Melting scheme [8]

### 2.1.1.2 Selective Laser Melting

It is a similar process compared to EBM, based on the powder bed technology. However, the difference is that the energy source is a laser rather than an electron beam. Similarly to EBM, the powder is fed into a building substrate plate where the laser focuses and melts that powder. The building plate is then descended and new powder is fed, iterating the process until the object is completed. Instead of the fabrication happening inside a vacuum chamber, this process requires an inert gas chamber – generally argon or nitrogen – with the smallest content of oxygen possible in order to reduce the unwanted oxidation of tracks. In a variation of this technique, called Selective Laser Sintering (SLS), the powder is sintered and not melted.

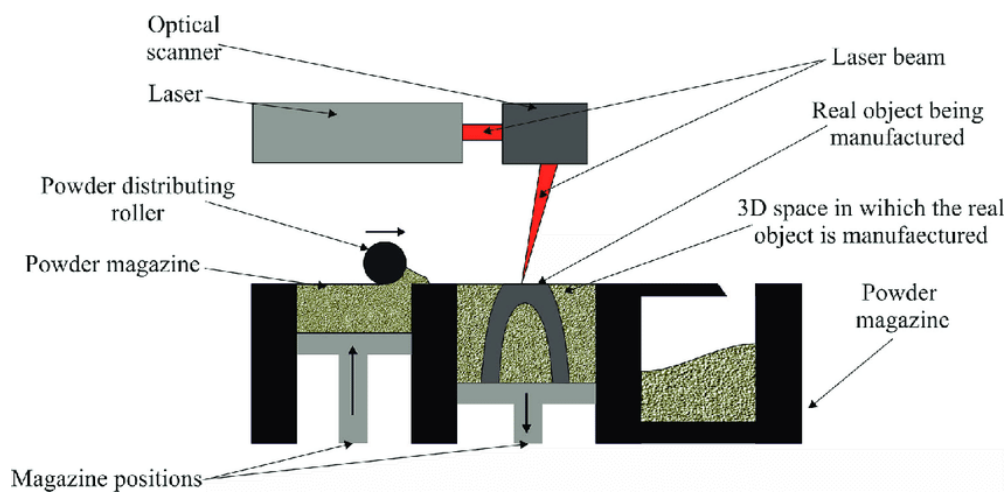


Figure 2. Selective Laser Melting scheme [9]

### 2.1.1.3 Laser Metal Deposition

Laser Metal Deposition is a powder feed or wire feed based technology, thus the principle is partially different from the previous methods. It is also known as laser cladding. The energy source is the laser which is focused by mirrors into a single spot and by its energy it melts the material generating single tracks firstly onto the substrate. Then, those tracks are superposed generating the desired shape. In this respect, powder injection based laser cladding is the most used one. The powder is fed via the nozzle and carried by an inert gas – generally argon [10] – which acts as a shielding gas too. A non-oxidative environment is generated then on the laser spot, the powder is injected and melted and with the combination of several axis movement of the nozzle the track is generated [11]. The use of the powder injection allows more flexibility on the geometry and conformability of the track as well as the possibility of building metal alloys' and metal matrix composites' parts [12,13]. Furthermore, this technology is also used for repair due to its possibility of building complex geometries in short time [14].

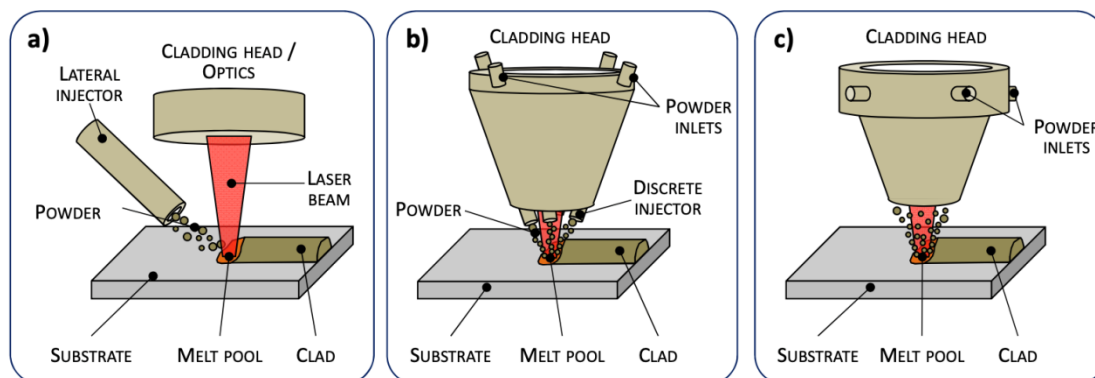


Figure 3. Different configurations of Laser Metal Deposition. a) Lateral powder injector. b) Discrete coaxial nozzle. c) Continuous coaxial nozzle. [15]

The flexibility is obtained by the variability of parameters that this process avoids. In this way, different results are obtained but keeping the intrinsic one-step fabrication intact. The interconnection between these parameters and the achieved properties is therefore a wide area to develop this technology. The most important parameters are:

- **Laser power.** Laser must be of high frequency in order to get the less possible variations of the nominal laser power. Higher powers affect more in the melted zone and thus achieving higher temperatures affecting the mechanical properties of the parts [12]. It is recommendable to have an upper limit of 5 KW.
- **Powder flow rate.** The powder is injected from powder hoppers and carried by the inert gas through the nozzle. As obvious, the higher the powder rate the taller and wider are the tracks. However, the excess of rate combined with a low power can result in not achieving the melting of the whole flow, causing porosities and heterogeneity in the tracks [16].
- **Inert gas rate.** There are generally two main entrances of the gas: the carrier gas and the shielding gas. As previously mentioned, this gas is generally argon but some studies have been carried out, for example, on the utilization of helium gas as carrier gas and observing the influence of a mix of these gases when producing tracks [10]. Furthermore, the two different flow rates affect on the distribution of the powder into the melt pool. Consequently, an inappropriate gas flow would result in the powder not melting completely and therefore the appearance of porosity of the built parts [17]. Given that, appropriate gas rate will create the required inert atmosphere in the melt pool avoiding the oxidation and a considerable powder feed rate concluding in better tracks.
- **Scanning speed.** As it is common in all types of manufacturing, the scanning speed is an important parameter to take into account. The nozzle moves with this scanning speed and the tracks properties are changed with the speed variation. As obvious, if the scanning speed decreases with all the other parameters constant, tracks become wider and taller. In addition, the interaction time between the powder and the laser spot increases and thus the tracks are solidified more slowly, resulting in changes in the microstructure and altering the mechanical properties [18].

- **Overlap.** Multilayer deposition requires the overlapping between consecutive layers in order to not obtain extreme roughness of the surface accomplished. The overlap is defined as the ratio of the overlap by width (lateral overlap) or height (vertical overlap) in percentage. As [19] states, the most recommendable range when deposition takes place is between 13 and 25%.

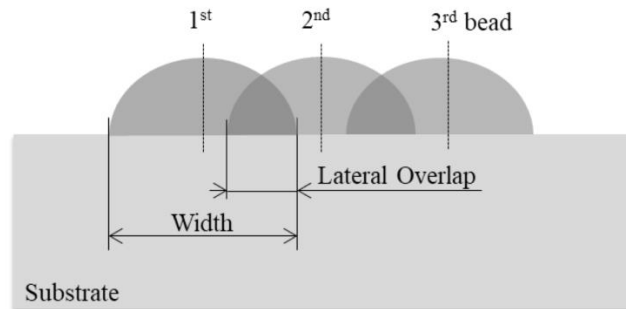


Figure 4. Lateral overlap between tracks [19]

The optimal calibration of these parameters concludes with the desired results, shape and properties depending on the situation. These parameters affect on the outputs of the results and can be characterized with characteristics of the tracks, such as wettability, dilution, mechanical properties, roughness, porosity, cracks and the microstructure.

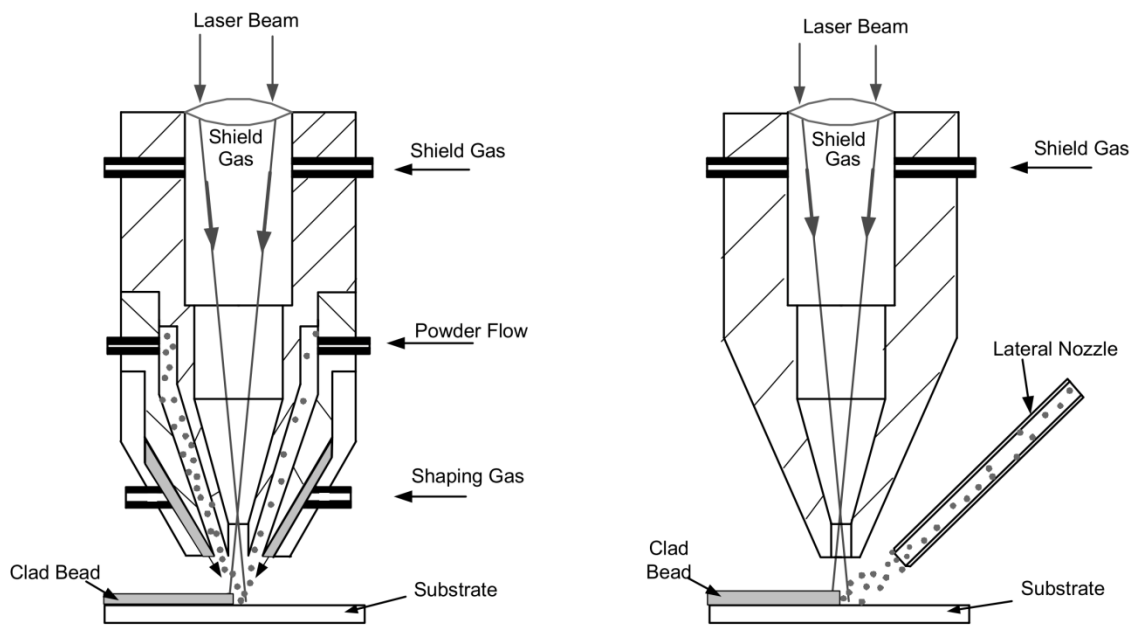


Figure 5. Laser Metal Deposition scheme. Detail on powder flow, gas flow and laser focusing. Coaxial and lateral nozzles [4]

## 2.2 Composite materials

Pure materials are poorly used nowadays. They are very hard to obtain and their properties alone cannot fulfill the needs of the market. In this respect, there has been development of every material since they were discovered in order to meet the requirements of their use in service. New engineering industries such as automotive, medical, aerospace etc. require very specific behaviors and technologies only acquired by the development of new type of materials. Consequently, the mechanical properties of these new materials must remain the same with improvements for the working requirements [20–23]. Development of these materials have been achieved by combination of multiple materials in order to create composites.

Composite materials are classified as: composites reinforced by particles, composites reinforced by fibers and structural composites. In this respect, composites are composed by two main phases: one continuous phase called matrix and the dispersed phase embedded into the matrix called reinforcement [24]. In between these two phases the interphase is located achieving the required bonding between them.

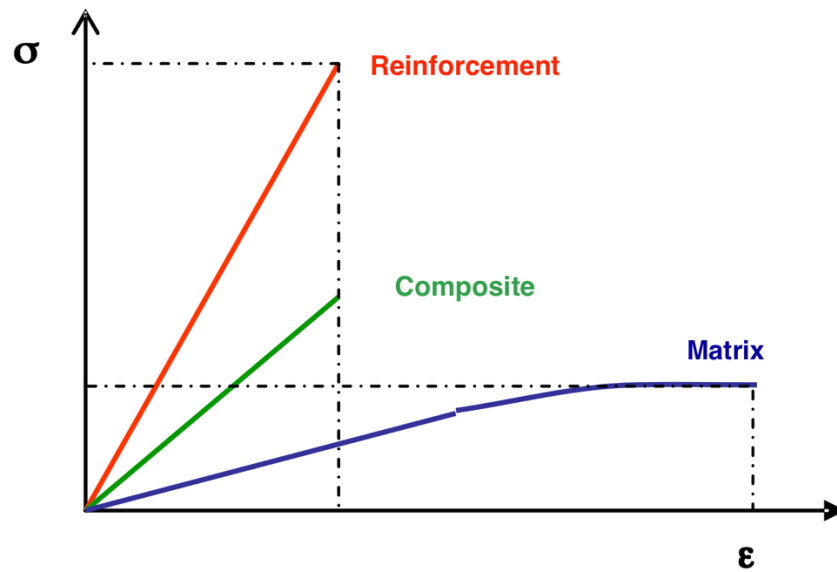


Figure 6. Example of combination of strength-elongation in a proper composite [24].

### 2.2.1 Metal Matrix Composites

Metal Matrix Composites (MMCs) are a type of composites where the matrix is constituted by a metal. These are fabricated in a way that the resulting material is capable to withstand high temperature operations, excellent abrasion resistance and tolerate minimal attack from corrosive environments. Currently mainly MMC which are being produced and used in different industries are aluminum alloys, magnesium alloys, titanium alloys, nickel based superalloys and steel matrices reinforced with several ceramic particulates as the dispersed phase [25]. These reinforcement ceramic particulates are nowadays generally SiC, TiC, Al<sub>2</sub>O<sub>3</sub>, W, WC, C, graphite, TaC, TiB, TiB<sub>2</sub>, NbC, Mo and B<sub>4</sub>C [26]. Indeed, these ceramic particles introduce the hardening on the softer metallic matrices, improving properties such as harder surfaces and higher wear resistance. Regarding additive manufacturing of MMCs, the particulates need to have a reasonable wettability in order to obtain the desired MMC for not losing the perfect embeddedness causing a not perfect matching of the mechanical properties. In addition, graphite, SiC, TiC and WC are the most commonly used particulate reinforcements in AM [27].

Concerning laser cladding of MMCs, the reinforcements particulates withstand higher temperatures than the ductile metallic matrix. Therefore, in the event of depositing the

clad, a melt pool of the matrix is created, with the reinforcement particles dispersed. The powder injection allows more homogeneous distribution of these particulates on the solidified clad, contributing to more isotropy in terms of mechanical properties [28]. Introducing those ceramic particles increase the abrasive wear resistance of surfaces, all depending on how those particulates are distributed on the surface: the more homogeneous the distribution, the better wear resistance they achieve [29].

### 2.3 Used materials

For the experimental work which is wanted the used materials are in accordance with desired performances of the MMCs. The matrix used is the easy printable SS316L reinforced with WC particulates. These two materials are powder injected through a nozzle and deposited in tracks via Laser Metal Deposition technique.

#### 2.3.1 Stainless Steel 316L

Stainless steels appeared in the materials field when common steel began to oxidize in its multiple services forms working in corrosive environments. Currently, stainless steels are the most used steels in several industries such as automotive, tool, aerospace, construction, energy industries where harsh environments need to be withstood. In this respect, stainless steels are considered as such when the content of chromium inside the additive elements of a steel is 10,5% in weight as a minimum. Consequently, if not precipitated at grain boundaries, it leads to the creation of an oxide layer that protects the steel from the general corrosion of it.

There are four types of stainless steels: austenitic, ferritic, martensitic and duplex stainless steels. They differ in the carbon content and the additive elements which are introduced when alloying. Stainless Steel 316L corresponds to an austenitic steel. Indeed, austenitic stainless steels are the most used and most common steels nowadays in every industry. They offer a great ductility and strength combined with the better corrosive resistance of the steels. They are denominated as such as they have austenitic microstructure at room temperature since they have nickel and manganese acting as austenitic phase stabilizers. Nickel is a austenitic phase stabilizer and it is the reference

to compute how much austenite phase is going to be in the final alloy. The calculation of austenitic phase stabilizers can be computed by [30]:

$$Ni\ equivalent\ (\%wt) = Ni + Co + 0.5Mn + 0.3Cu + 25N + 30C$$

Different grades of steels inside the austenitic steels can be found. In this respect, 304 is the most fabricated stainless steel (50% of the total stainless steels production) followed by the 316. Therefore, the 316 is a very studied steel but it even allows more development. The L of 316L stands for *Low carbon*. This decrease in the carbon content of the steel prevents the creation of chromium carbides in the grain boundaries – a phenomena called sensitization. Therefore, the amount of intergranular carbides decreases. Then, low carbon stainless steels perform better corrosion resistance than normal composition stainless steels. Low carbon steels were developed to withstand corrosive resistance when welding. Indeed, 316 has better corrosion resistance than the 304, and so has 316L. The composition of both 316 and 316L are the following ones as given by Sandmeyer Steel Company:

		Fe	C	Mn	Ni	Cr	Mo	S	Si	P	N
<b>316</b>	min.	Bal.	-	2.00	10.0	16.0	2.00	0.03	0.75	0.045	0.10
	max.		0.08		14.0	18.0	3.00				
<b>316L</b>	min.	Bal.	-	2.00	10.0	16.0	2.00	0.03	0.75	0.045	0.10
	max.		0.03		14.0	18.0	3.00				

Table 1. Chemical composition of 316 & 316L stainless steels [31]

Table 2 main properties of 316L are reported:



Density	7870 – 8070 kg/m <sup>3</sup>
Melting point	1380 – 1400 °C
Specific heat capacity	490 – 530 J/kg·°C
Latent heat of fusion	260 – 285 kJ/kg
Thermal conductivity	13 – 17 W/m·°C
Vickers hardness	170 – 220 HV
Yield Tensile Strength	170 – 310 MPa
Young's modulus	190 – 205 GPa
Elongation (% strain)	30 – 50%
Poisson's coefficient	0,265 – 0,275
Fracture toughness	53 – 72 MPa·m <sup>0.5</sup>
Maximum service temperature	750 – 925 °C
Electrical resistivity	69 – 81 μΩ·cm
Electrical conductivity	2,13 – 2,5 %IACS
Price	3,11 – 3,49 €/kg

Table 2. SS316L properties [32]

### 2.3.2 Tungsten Carbide – WC

A carbide is a compound based on the union of a metal and carbon. In this case, the union of tungsten and carbon forms the denominated tungsten carbide. It is found in the nature as the mineral qusongite. This mineral is mainly WC with some other impurities such as chromium, nickel and titanium [33]. The W-C phase diagram gives as a conclusion that the W-C union may result in the formation of two different compounds: WC carbide and W<sub>2</sub>C carbide. These two phases can be observed on that diagram:

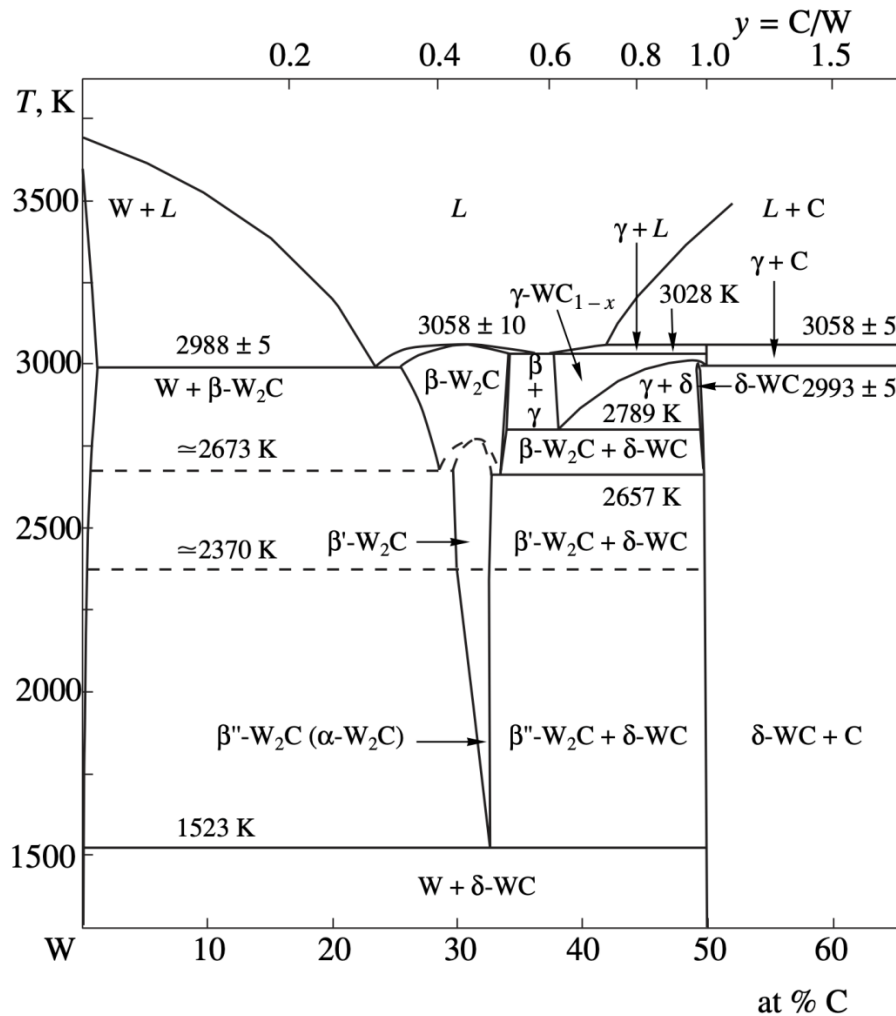


Figure 7. W-C phase diagram [34]

At lower temperatures the most stable phase is the  $\delta\text{-WC}$ , which is the most common phase. At higher temperatures, as the diagram shows,  $\beta\text{-W}_2\text{C}$  phase appears regarding low concentrations of C. In this respect, the  $\beta\text{-W}_2\text{C}$  phase exhibits a hexagonal atomic structure and the  $\delta\text{-WC}$  phase exhibits a hexagonal structure too. In between these two phases the  $\gamma\text{-WC}_{1-x}$  intermediate phases appears, only at high temperatures up to 2500 °C, and it exhibits a cubic structure.

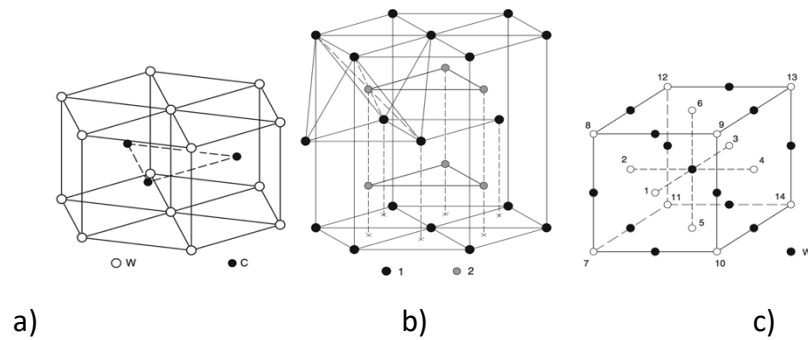


Figure 8. W-C present phases. a) Higher  $\delta$ -WC hexagonal structure. b) Hexagonal structure of the  $\beta$ - $W_2C$  carbide. Tungsten atoms ( $\bullet$ ) form a hcp hexagonal structure and carbon atoms occupy grey interstitial spots ( $\circ$ ) with a probability of 1/2. c) Cubic structure of the  $\gamma$ - $WC_{1-x}$  carbide [35]

Table 3 reports the main properties of WC:

Density	15300 – 15900 kg/m <sup>3</sup>
Melting point	2820 – 2920 °C
Specific heat capacity	184 – 190 J/kg·°C
Latent heat of fusion	330 – 370 kJ/kg
Thermal conductivity	28 – 88 W/m·°C
Vickers hardness	3100 – 3600 HV
Yield Tensile Strength	373 – 530 MPa
Young's modulus	600 – 670 GPa
Elongation (% strain)	0,06 – 0,09%
Poisson's coefficient	0,2 – 0,22
Fracture toughness	7,4 – 9 MPa·m <sup>0.5</sup>
Maximum service temperature	750 – 925 °C
Electrical resistivity	63,1 – 100 $\mu\Omega$ ·cm
Electrical conductivity	1,72 – 2,73 %IACS
Price	16 – 24,9 €/kg

Table 3. WC properties [32]

## 2.4 Microstructure of laser cladDED SS316L + WC

### 2.4.1 Microstructure of laser cladDED SS316L

The characteristics of the process of laser cladding is different from traditional methods, and as it has been stated in section 2.1 and subsection 2.1.1.3, it has different results compared to traditional fabrication techniques. In this sense, laser cladding achieves higher cooling rates than for example forging, casting and annealing, as well as providing the possibility of producing the part from scratch even with complex geometries. Whereas with traditional fabrication techniques post-treatment of parts is almost inevitable, with subtractive methods such as turning and milling to achieve the desired shape, other post-treatments are needed for AM, such as hot isostatic pressing or spark plasma sintering [36]. Therefore, the results achieved differ from the traditional ones.

LMD and generally all AM techniques obtain finer microstructures in every built part as a consequence of the high solidification rate this technology provides, up to  $10^6$  K/s. Generally, the finer microstructure, the more enhanced mechanical properties has the material built [37–39]. Some studies have been taken out to study the microstructure of laser cladDED 316L parts. Durejko et al. [39] and Yadollahi et al. [40] for instance have studied the evolution of the microstructure creation from the melt pool and the final results achieved. The results show the *arc-shaped* forms created by continuous scans of the laser. This configuration is due to different layers being overlapped and partially remelted when a successive scan passes by. This shape is characteristic of the process and can be observed in other metal deposits. In both studies the intragranular cellular structure could be observed with the segregation of the alloying heavy elements such as chromium, molybdenum, etc. shown in Figure 9. As a consequence, since those mentioned elements are alpha stabilizers (ferritic phase), ferritic phase appears in cell boundaries, not perfectly achieving a 316L austenitic steel. However, this can be solved with a posterior heat treatment of the parts [40]. Not only heavy elements segregate in those subgrain cell boundaries, but also dislocations are located there [41].

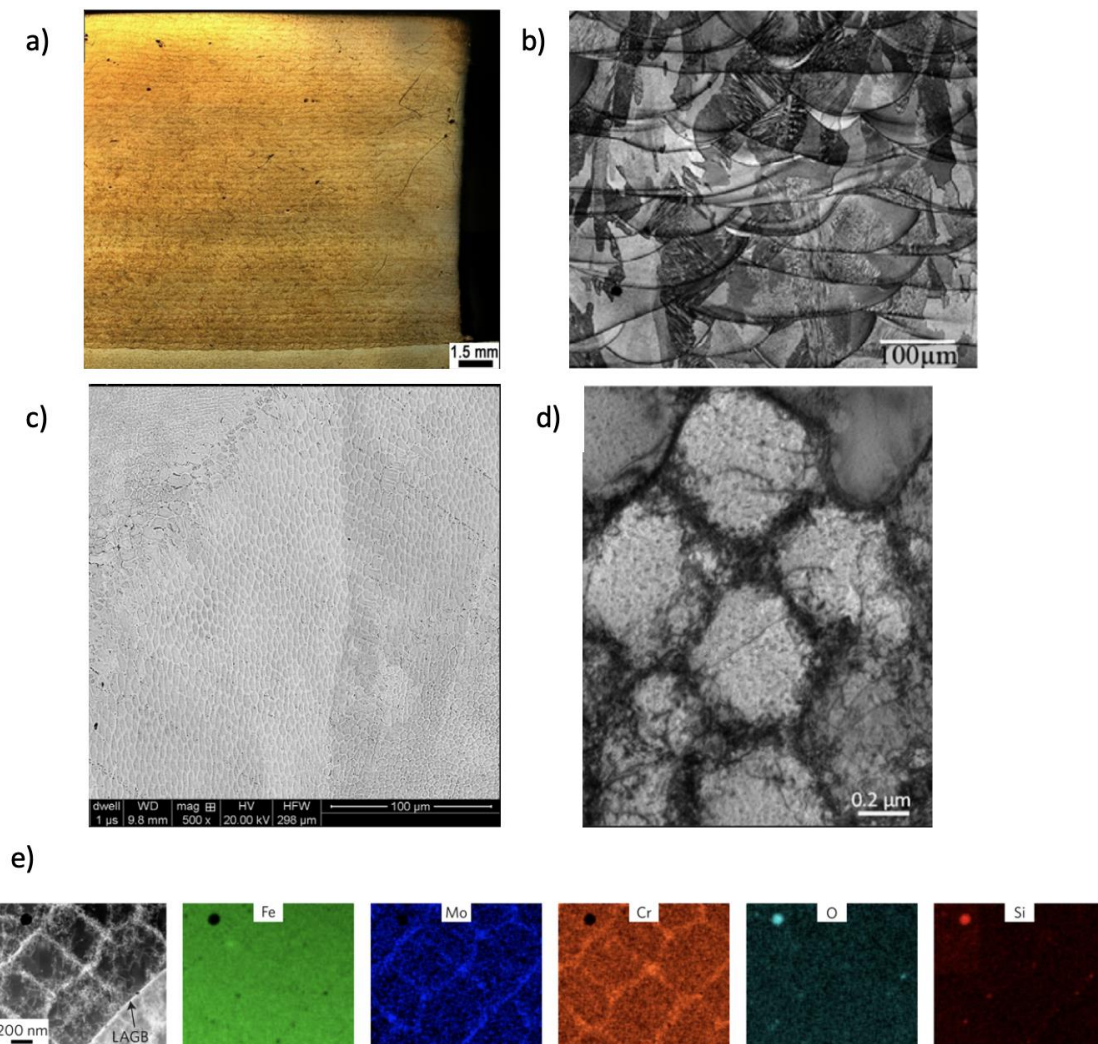


Figure 9. a) Optical macrostructure of a laser deposited SS316L. [39] b) Arc-shaped forms. Different tracks can be observed [42]. c) Fine and columnar cells [39]. d) Dislocations located in subgrain cell boundaries [41]. e) Segregation of heavy additive elements of 316L steel [43]

The solidification direction affects the microstructure. Generally epitaxial growth of grains happens in LMD. This can be observed in Figure 10. As the heat flow caused by the laser gets into the melt pool, solidification happens from the edges to the core point where the laser moves away causing different solidification rates to occur and thus the appearance of different structures within a single track. In addition, following scans affect the previously solidified tracks as well, obtaining different microstructures and affecting properties at that scale such as microhardness. As a consequence, some parts of the microstructure show dendritic growth and some other might show columnar growth [40]. The last part of the track to be solidified, as it might result obvious, is the laser line zone.

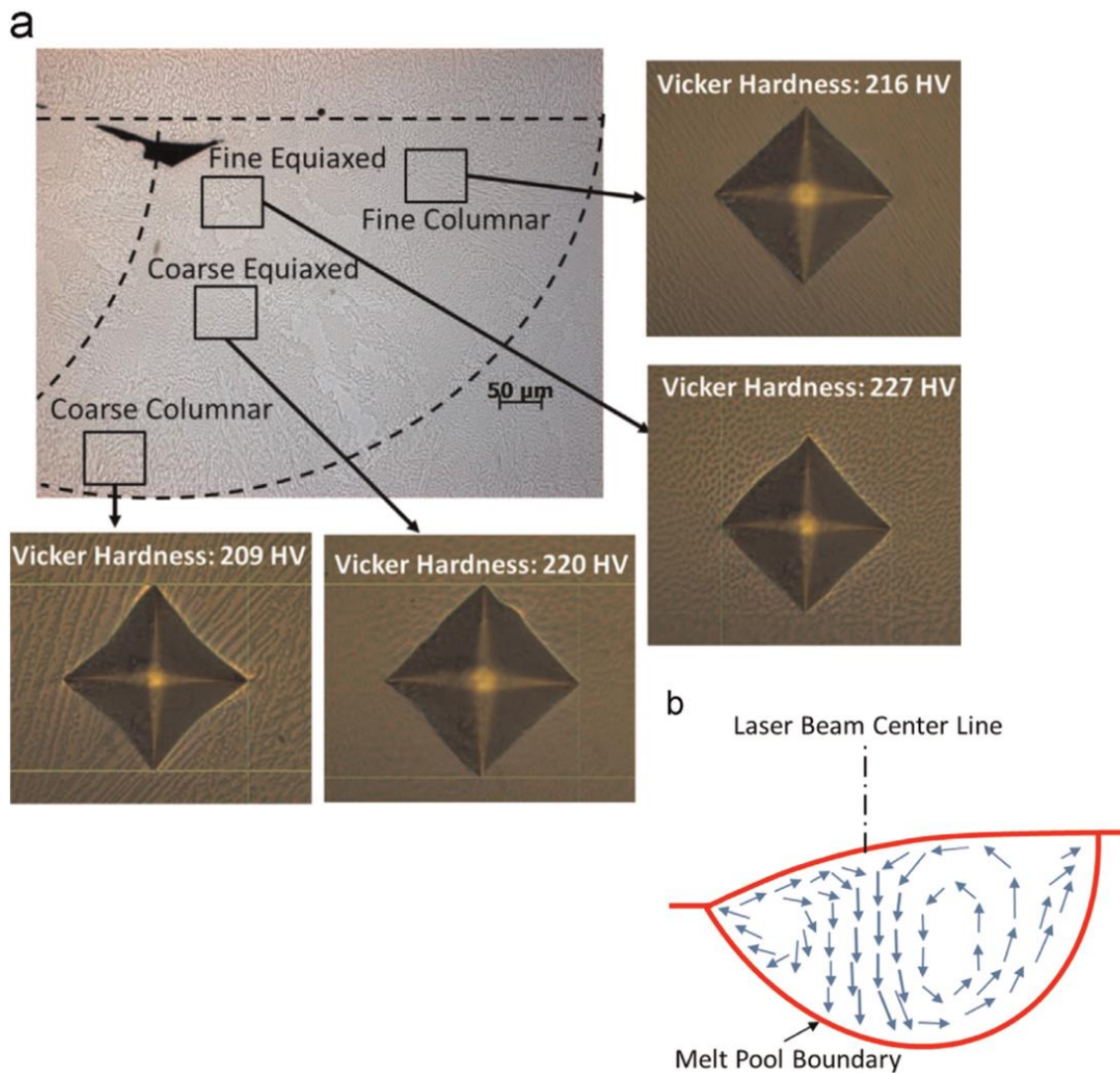


Figure 10. a) Different microstructure and microhardness within a single track. b) Heat flux and consequent solidification of a track [40]

#### 2.4.2 Microstructure of laser clad SS316L with WC addition

Addition of WC particulates on the deposition of the 316L provides better properties to the solidified part as a MMC is created. As previously mentioned, these MMC are commonly very good wear resistant materials, as the WC introduces hard ceramic carbides to the softer matrix given by the steel. In this sense, the tungsten carbides sink onto the melt pool of the steel, are dissolved in the liquid (as they have higher melting point, they do not achieve a total melting) and when solidification happens complex microstructure is created between the austenitic steel matrix and the ceramic tungsten carbide. These carbides do not only come from the addition of WC, but also from the steel's own solidification if the conditions are satisfied (i.e. the carbon content is

sufficient) because alloying elements have more affinity for carbon rather than for iron [44]. Therefore, there is a good knowledge of carbides formation within a steel since steels have been manufactured for a long time. In this respect, three types of carbides can be analyzed depending on when they were formed during the solidification [44]:

- **Primary carbides.** They are the first carbides to solidify. They precipitate from the liquidus and they set the liquidus temperature.
- **Eutectic carbides.** Since they are the last to solidify, they set the solidus temperature. They segregate in cell boundaries as well as in grain boundaries.
- **Secondary carbides.** These carbides precipitate when the solidification is complete and do not segregate in boundaries but they appear inside cells or grains. These are more common when eutectic carbides precipitate when suffering a heat treatment [45].

Concerning the addition of WC onto the 316L matrix, there is a reaction between them that results in a partial dissolution of the WC particulates and the formation of a different structure between the particulates and the matrix. Consequently, an enriched MMC is obtained in terms of the carbides solidification [46]. However, as LMD's characteristic fast cooling rates the WC are less dissolved onto the melt pool and thus the wear resistance can be influenced for the better. Hereafter the phases created during the solidification of the tracks are going to be analyzed:

- **M<sub>6</sub>C.** These eutectic carbides show a characteristic central platelet from which secondary ones of the carbide split with austenite grains. At faster cooling rates secondary platelets are less separated between each other. M stands for the additive elements such as W, Mo, V, Cr and generally Fe. They have a face cubic centered (fcc) structure and reach up to 1500 HV [47].



Figure 11. Morphology of eutectic  $M_6C$  carbides [48]

- $M_2C$ .**  $M_2C$  eutectic carbides depend strongly on the chemical composition and the cooling rate. In this respect, there is the need of a classification of these carbides for knowing differences in morphology and terminology, and in the end, knowing how they are formed. There are two types of eutectic  $M_2C$ : complex-regular and irregular, also called rod-like and lamellar respectively [49]. The morphologies can be seen in Figure 12. At high temperatures between 900 °C and 1150 °C when heat treatment is done these carbides are unstable and decompose in  $M_6C$  and  $MC$  eutectic carbides [47,50]. They exhibit a hexagonal structure.

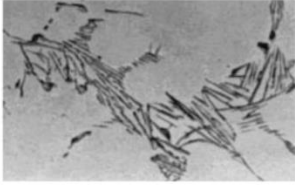
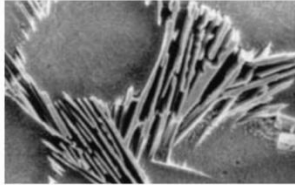
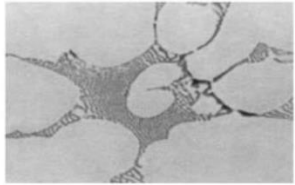
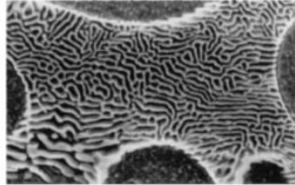
Optical	SEM	
		Irregular
		Complex regular

Figure 12. Morphology and classification of  $M_2C$  eutectic carbides [47]



- MC.** MC eutectic can be found in three ways: divorced which precipitates as isolated crystals, irregular which has a petallike morphology and is poorly eutectic coupled and complex regular (also known as lamellar) which is coupled eutectic and has a branched petallike morphology. This classification can be observed in Figure 13.

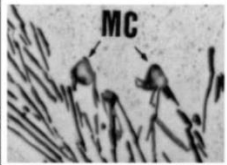
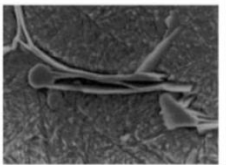
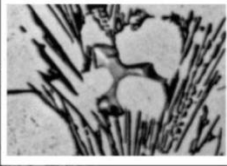
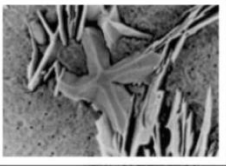

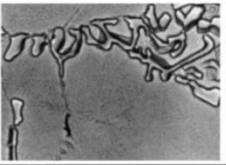
Optical	SEM	Carbide morphology	Eutectic classification
		Idiomorphic	Divorced
		Petallike	Irregular
		Branched petallike	Complex regular

Figure 13. Morphology and classification of MC eutectic carbides [47]

- M<sub>7</sub>C<sub>3</sub>.** These carbides are generally formed due to the presence of high amounts of chromium in stainless steels and by high solidification rates. They exhibit a rod- or blade-like morphology with a hexagonal shape. The morphology can be seen in Figure 14. Liu et al. [51] had shown how is the growth mechanisms of these type of carbides.

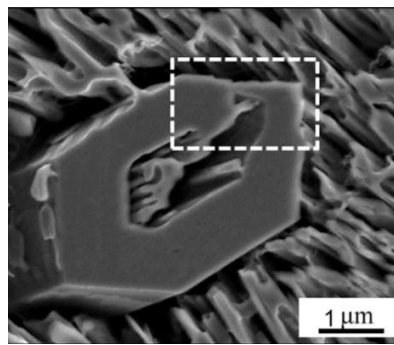


Figure 14. Morphology of  $M_7C_3$  carbides [51]

- $M_{23}C_6$ . It is a secondary carbide which precipitates when the steel is solidified. Segregation on grain boundaries – sensitization – of heavier element such as chromium generates these carbides on that area.

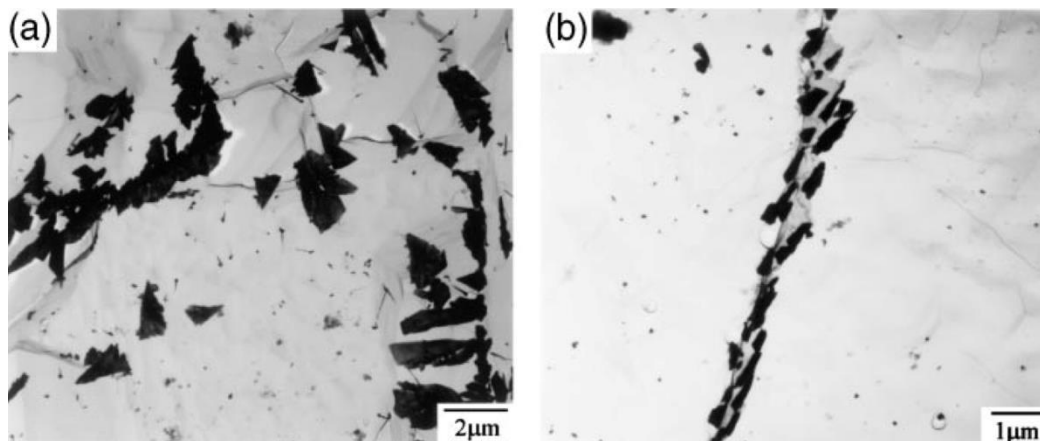


Figure 15.  $M_{23}C_6$  carbide distribution in grain boundaries of two samples of 316L [52]

These carbides are generally obtained in the steel when solidified, although they do not belong specifically to laser clad 316L+WC composite. Thus, the study of T. Maurizi Enrici et al. [53] allows showing great results from the microstructural characterization of a 316L+WC composite.

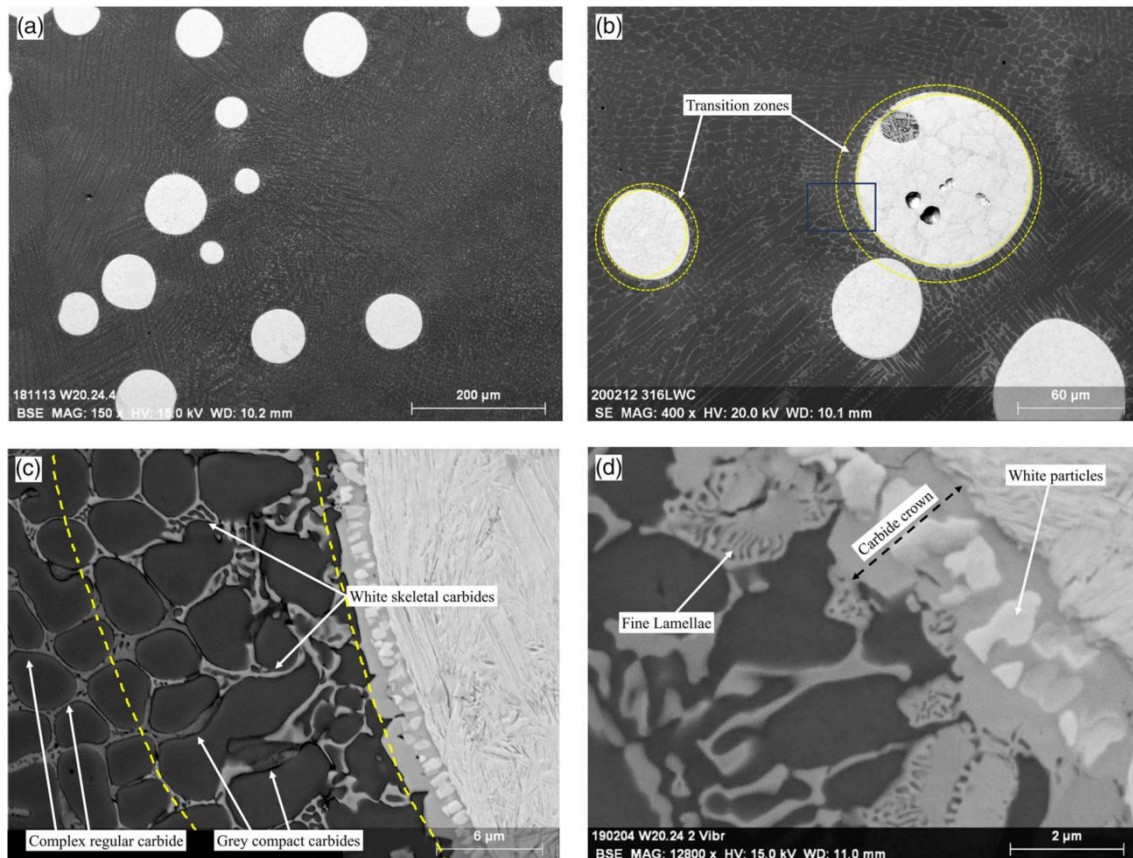


Figure 16. a) SEM obtained microstructure of 316L+20%WC composite. White WC carbides embedded into the reinforced matrix. b) Overview of a localized WC carbides showing the transition zones (TZ). c) Magnification of the TZ of b) showing the solidification carbides coming from the partially dissolved WC particulate. d) Higher magnification showing the lamellar structure of the carbides and the carbide crown created near the WC particulate. [53]

Figure 16 shows the microstructure of a laser cladded 316L+20% WC composite. It can be observed a cellular-dendritic structure caused by the partially dissolved WC particulates into the matrix due to the reaction between the matrix and those particulates (Figure 16b). Close to the carbides a transition zone is recognized in which white skeletal carbides have more presence than in further parts from the particle. These with carbides come directly from the dissolution of the WC particle causing them to be richer in tungsten. This is easily reasoned as they show a brighter color in the SEM obtained images. Grey carbides appear as well which are mainly chromium carbides generated due to the chromium presence in the matrix (Figure 16c). Adding to these white carbides, near the WC carbides a carbide crown is generated composed by white crystal particles surrounding the WC core which has not been dissolved. The carbide crown thickness depends on the size of the WC particle: the larger the particle, the

narrower the carbide crown. The white lamellar carbides are grown from the carbide crown.

## 2.5 Wear of materials

Among the mechanical properties of interest for industrial applications, this thesis is mainly focused on studying the mechanical wear of the materials and how they can be improved with the mentioned new techniques and new materials. Surfaces of materials are the first part to be affected by hazardous environments and exactly in that moment tribology takes place as the main phenomena to study. Indeed, machines lose reliability due to removal of surface material and thus a way to monitor this wear is necessary in new material approaches. In that sense, development has been made in multiple materials by combining them in order to achieve better results, making composites. In the end of the development the testing is an obligatory step for identifying the advantages and disadvantages and how to exploit the best properties of the material with process parameters variation; after all, trial-and-error. The next subsection will consist in what wear is about and which are the available tests for testing materials.

### 2.5.1 Types of wear

Wear is the loss of surface material due to several mechanisms which are going to be explained below.

#### 2.5.1.1 Abrasive wear

Abrasion consists in the loss of material due to the continuous passing over the surface containing that material. It is necessary for abrasive wear that the particles which are affecting the surface are harder than the material of the surface. More inclined surfaces allow an easier abrasion as the particles make contact with those parts and may pull the material from the surface. There are multiple mechanisms of abrasive wear: cutting, fracture, ploughing and grain pull-out [54]. These mechanisms, in fact, depend on the properties of the material they are attacking. If the material is ductile, cutting or ploughing are more common. If the material is brittle, fracture or grain-pull out are more

likely to occur. Consequently, those mechanisms can be classified as a plastic deformation outcome in ductile materials and very little deformation in brittle materials. However, this is not true always as some ductile materials can have brittle areas in part of surfaces. In Figure 17 and Figure 18 those mechanisms can be observed.

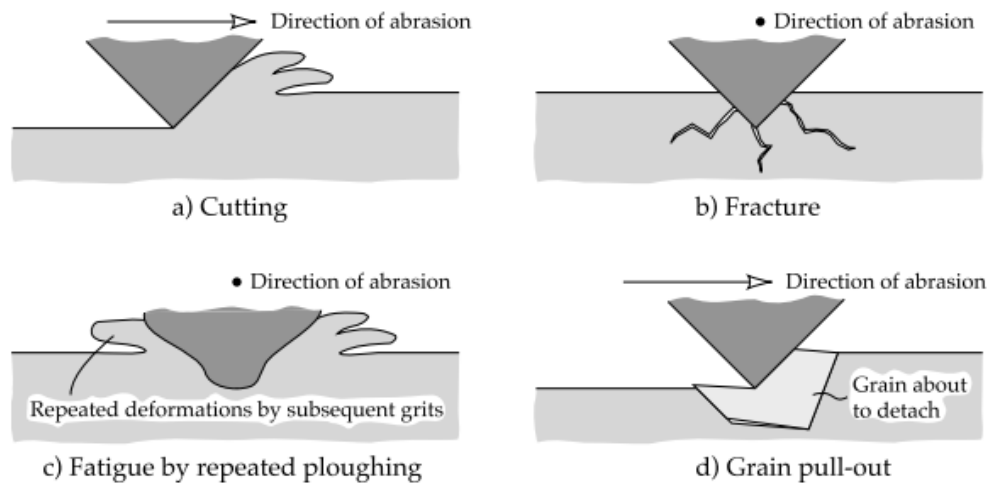


Figure 17. Abrasive wear mechanisms. a) Cutting. b) Fracture. c) Ploughing. d) Grain pull-out. [54]

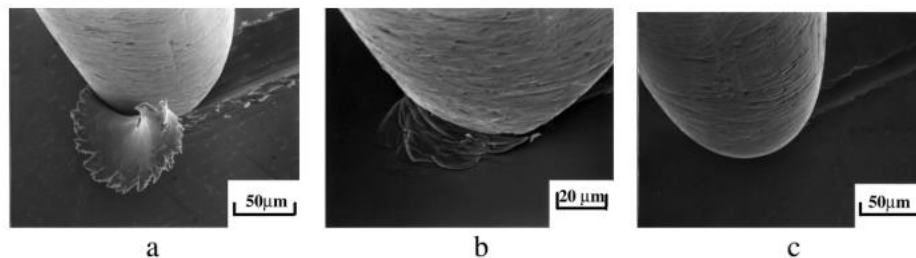


Figure 18. Abrasive wear mechanisms seen by SEM. a) Cutting. b) Wedge-forming. c) Ploughing. [55]

Abrasive wear can be given in two forms taking into consideration how the contact between exterior particles and the surface: two-body problem and three-body problem. In this respect the affecting particles fixed in a rigid setting to another body is what the two-body problem is considered. This can be exemplified by the sandpaper or the grinding wheel used surface finish and polishing in traditional fabrication.

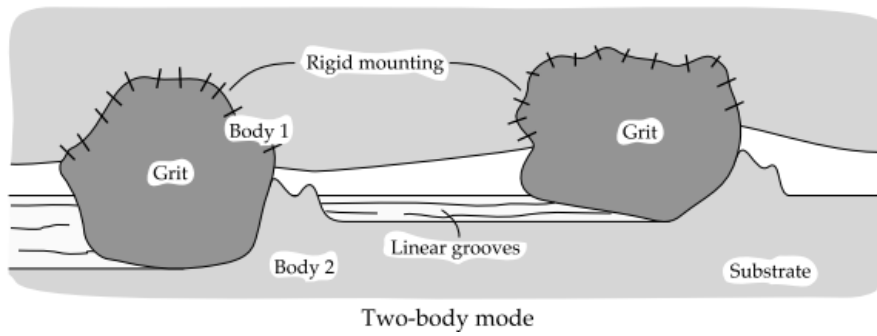


Figure 19. Two-body abrasive wear scheme [54]

In the case of three-body abrasion, however, abrasive grains are free sliding, rolling and contacting over the surface. This three-body abrasion can happen after first stages of abrasive wear, when wear debris appear and impede the natural track of the grits.

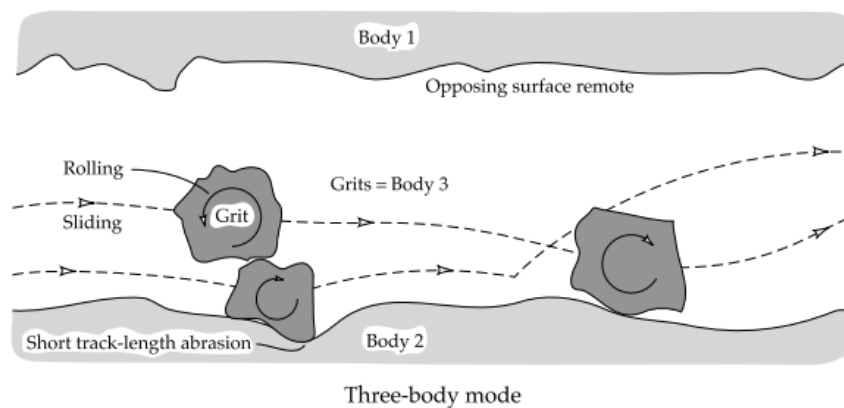


Figure 20. Three-body abrasive wear scheme [54]

### 2.5.1.2 Adhesive wear

In contrary to abrasive wear, where abrasive grains affect a softer surface, two contacting surfaces will adhere, given the needed conditions, causing removal of material due to high adhesion forces. Those conditions need to be satisfied and are very specific ones, because generally two surfaces do not adhere: oxide layers, liquids (such as water and lubricant oil) or even adsorbed gases affect in that interaction. Indeed, that surface contamination decreases real contact between the surfaces.

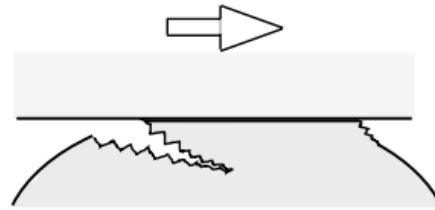


Figure 21. Adhesive wear scheme [55]

In that case, if interaction based on plastic contact is capable of avoiding sliding of both surfaces, adhesive bonding causes high plastic deformation causing the removal of material from one of the surfaces. Hence, friction loads and shear strength are important parameters to know in the event of adhesive wear. Moreover, the contact has to be evaluated depending on which type of materials are being put in contact: metal-polymer, metal-metal, metal-ceramic, polymer-polymer... Therefore, different friction loads will appear depending on these contacts and the adhesion will be different.

Regarding the adhesion wear follow up with time, some stages can be differentiated. Firstly, whereas it does not consist on material pulling off, the creation of the bonding between two surfaces is done only if the conditions to that bonding are satisfied. Secondly, this bond will suffer from huge plastic deformation and hardening of both materials will happen. Then, first material removal will occur and cracks will propagate; material removal from the weaker adhesive bonding will occur and it will be attached to the stronger material. This is known as material transfer occurring continuously during the whole adhesive wear process. Sometimes, the material transferred can be particles of debris mix of both materials. The process is illustrated in Figure 22.

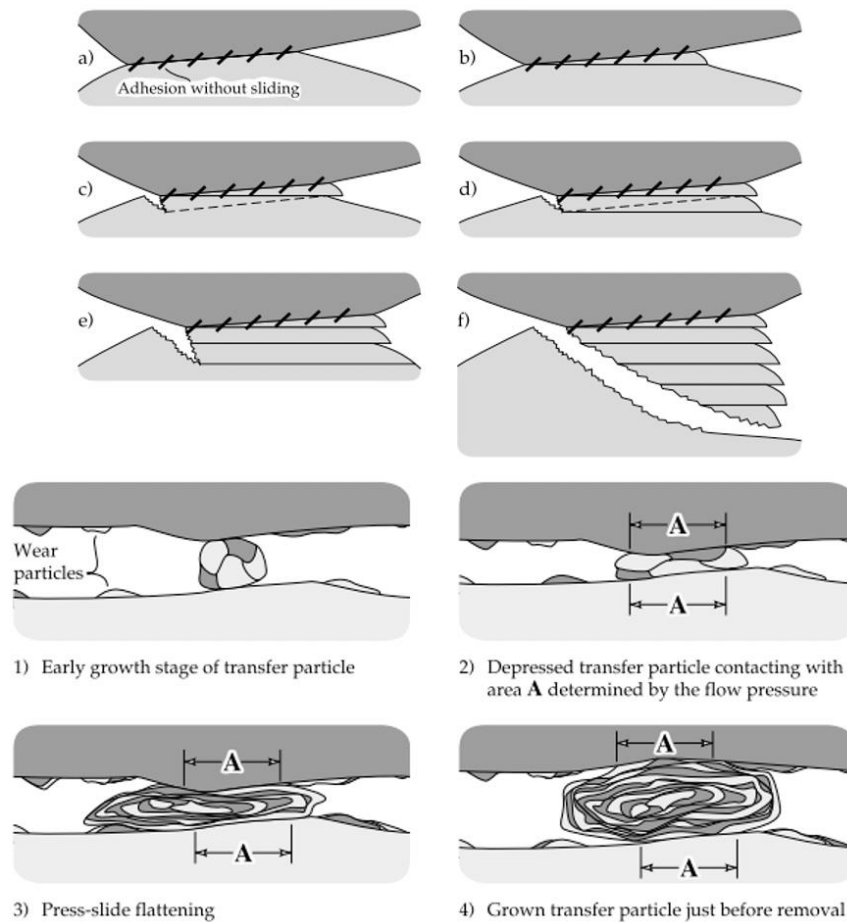


Figure 22. i) Progressive adhesive wear stages. ii) Growth of transfer particle with mix of debris of two surfaces [56]

### 2.5.1.3 Corrosive and oxidative wear

Although it might result to be the same concept, there are differences in the meaning of corrosive and oxidative wear. While corrosive wear consists in a combination of any type of mechanical wear (adhesive, abrasive...) with a corrosive reaction, oxidative wear is due to the wear affected by that material reaction with oxygen (usually in air), generating oxide layers. Some metallic elements are very likely to link with oxygen and affect the properties of the metal. Then, it is crucial to control these two types of wear as it might weaken the material more than expected.

#### **Corrosive wear**

As stated, corrosive wear is any type of wear (generally sliding) combined with corrosive reactions by the surface. In corrosive wear the corrosive reaction products act as different material from the substrate and thus the wear is mainly dominated by



them [51]. In that respect, there are four situations in which corrosive wear is acting as the main wear mode:

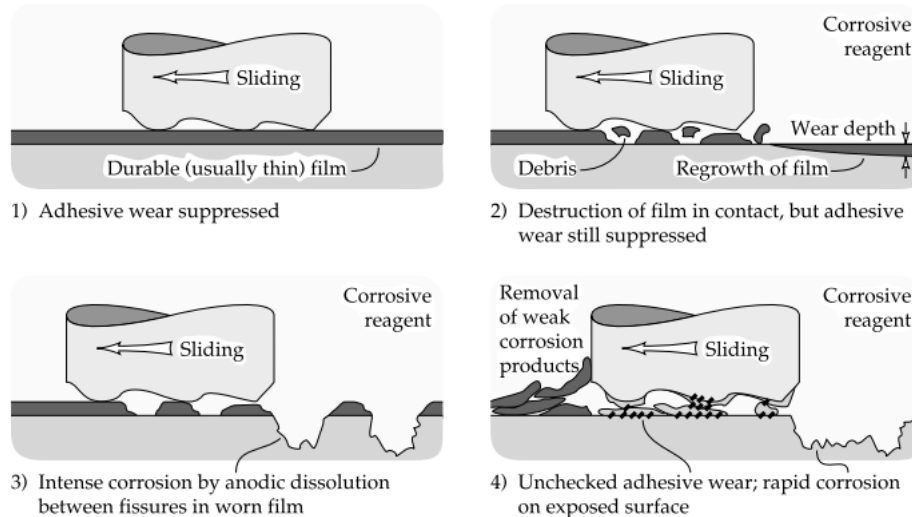


Figure 23. Four possible behavior of corrosive wear [57]

1. A layer inhibits the wear and corrosion to be formed, generally due to lubricants or contamination which act as a lubrication impeding the mechanism to occur.
2. The lubricant layer is destroyed due to its weakness and the sliding and then a considerable wear rate is likely to happen as the contact between the substrate and the contacting pin is made. In that case, the wear debris is both the protective layer and the substrate. After that, a growth of the film happens where there has been material removal.
3. The protective layer is intermediately worn and there is coupling between the remaining layers and the substrate, resulting in very highly corroded zones with high wear rates.
4. Corrosive and mechanical wear processes act separately and the result is a total combination of both of them. The wear rates are the maximum of the four situations.

### Oxidative wear

It happens more commonly in unlubricated metals which are located in corrosive environments, i.e. generally air. All metals react with oxygen resulting in very thin but protective oxide films with different characteristics depending on their affinity with oxygen. However, when a metal is subjected to sliding contact at high speed, due to the friction, a great amount of heat is generated, elevating the surface temperature and favoring the generation of a thicker oxide layer. This is because oxidation is a simple chemical reaction which kinetics depend as every other one on the Arrhenius equation:

$$k(T) = Ae^{\frac{-Ea}{RT}}$$

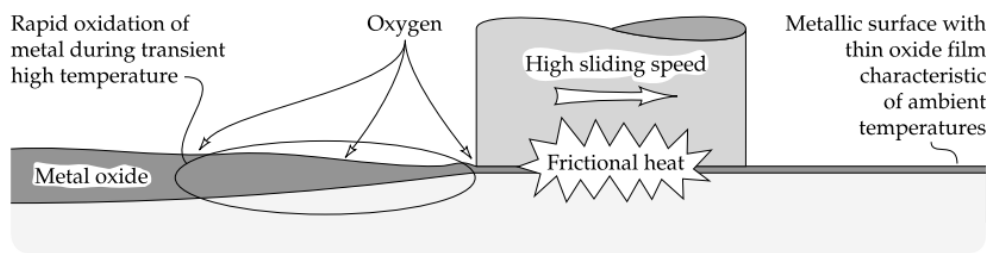


Figure 24. Oxidative wear scheme [57]

Quinn, who studied the oxidative wear, proposed this relation of the corrosive wear coefficient as [55]:

$$K_c = \frac{dA}{\xi^2 \rho^2 v} e^{\frac{-Ea}{RT}}$$

being,  $\xi$  the distance along which the wearing contact is made,  $\rho$  the oxide density,  $v$  the sliding velocity and  $A$  Arrhenius kinetic constant. As it can be observed, an increment in temperature enables the reaction to be faster and thus a thicker oxide creation. The increment comes from the friction heat generated during the sliding, so the higher the sliding the higher the temperature the contact will reach. However, it does not mean that at lower sliding speeds does not appear as a wear mechanism.

In the first stages of oxidative wear surfaces are put in contact and slid where severe wear occurs and the surfaces achieve a quasi-perfect bonding. This contact will not be perfect in the whole surface as every surface has its roughness causing higher contact areas while other areas do not contact at all. In this early contact the *plateaus* begin to form. Oxide starts to develop in those zones caused by the dry-sliding contact and the metal reacting with oxygen, ruled by the above mentioned relations. This stage of the oxidative wear act as a mild wear mechanism, as it reaches a growing but stationary stage with the oxide film formation. After many passes the oxide layer grows and extends as well, reaching the critical film thickness. If more oxide is created above that thickness due to the continuous contact and sliding, the oxide layer breaks and the wear volume rapidly increases. It can even happen that second hard phases appear into the metallic substrate altering wear properties in following passes of the pin, and thus altering the contact in future wear [55]. At this ending stage, the contact is established in other parts of the surface and the process become repetitive.

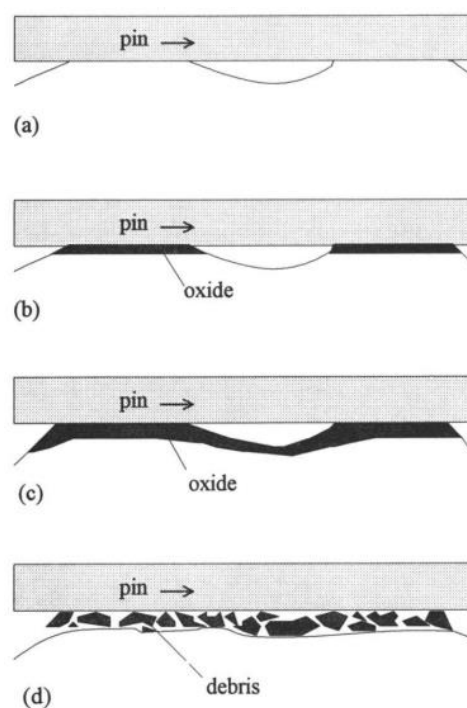


Figure 25. Oxidative wear stages. a) Formation of plateaus. b) Oxide development on plateaus. c) Oxide expansion. d) Oxide breaking up to form wear debris. [58]

At slow sliding speeds, however, even though the oxide film is generated as well, the rate of generation is reduced. Consequently, the previous formed oxide is deformed, which may result in adhesive wear between the two surfaces. Indeed, the wear debris is a mix of oxide debris and fractured oxidized metallic particles and can form a new oxide *plateau* in some specific parts. In that context, worn debris is continuously forming and deforming generating, first in plateau and then expanding, the oxide layer, which exhibits a smooth surface. This slow sliding oxidative wear can be observed in Figure 26.

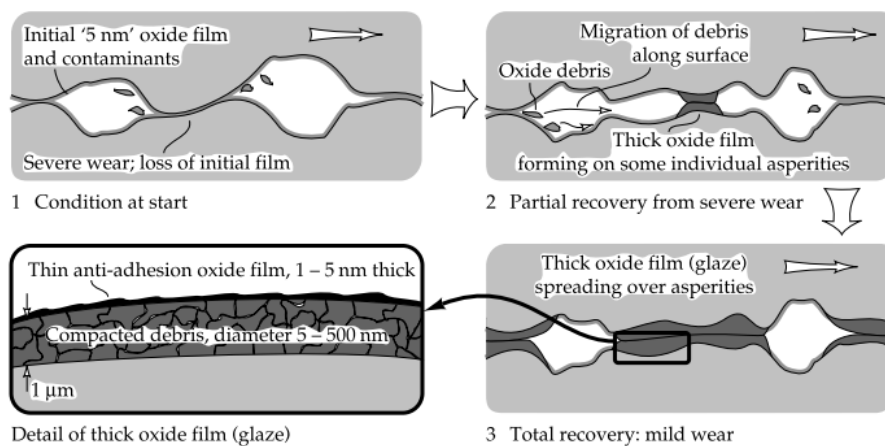


Figure 26. Oxidative wear stages at slow sliding speeds [57]

#### 2.5.1.4 Erosive wear

Erosive wear differs from abrasive because the main phenomena here is the impact of liquid or solid particles over a surface rather than the continuous passing of them. As every type of wear, the characteristics of erosive wear depends on the particle and the surface in interaction. The key in erosive wear is the word “impact”, as it wraps every type of wear which involve in particle impacting into surfaces and could not be categorized in any other mode of wear. These possible types can be seen in Figure 27. As it states, the angle and the speed of the particles determine which mechanisms of wear will appear, as well as the particle size. Low angles will induce in abrasive wear, as the trajectory is nearly perpendicular. High angles will act more as pure impacts and depending on the speed and size it will result in more plastic deformation or in a brittle breakage, or even melting and embedding of the particle. An example of erosive wear can be observed on LEO satellites [54].

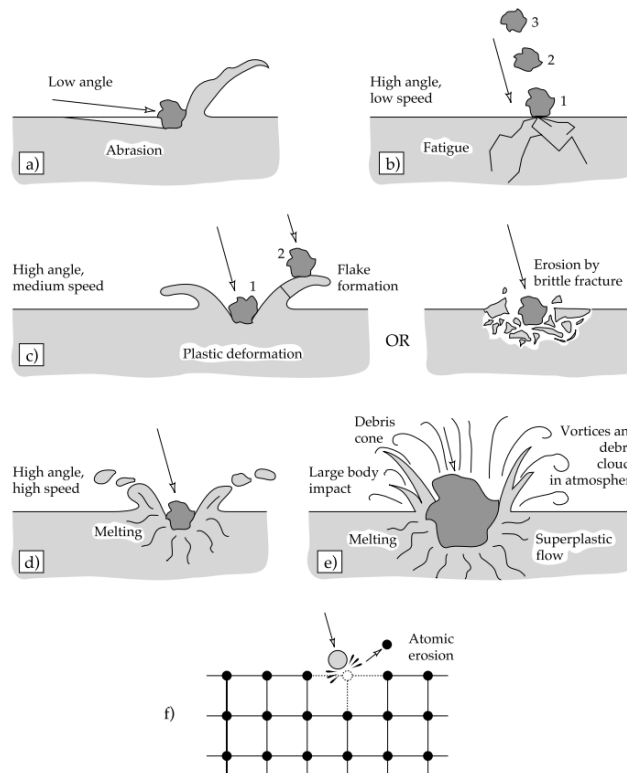


Figure 27. Possible mechanisms of erosive wear. a) Abrasion at low impact angles. b) Crack formation due to high angle impact and low speed. c) Plastic deformation or brittle breakage due to high angle impact and a considerable speed. d) Melting of the surface due to high speed impacts. e) Effect of the large particle in an erosive impact. f) Effect of tiny particle in erosive impact (atoms impact), atomic erosion. [54]

### 2.5.1.5 Fatigue wear

Sometimes, even when the contact between two alternating contacting surfaces is well lubricated some asperities contact can happen. If this contact becomes repetitive because, for example, a rotating shaft is touching the casing where it is located, this can cause localized high stresses and a fatigue failure in elements, as cracks are propagated. Another example of this are bearings since they require specific tolerances between surfaces and smooth contact surfaces to work reliably. In this respect, sliding and contact are the main cause of fatigue wear.

Under sliding conditions shear stress is generated in the surface where it reaches its maximum point. As one goes deeper into the material, less shear stress is withstood by the material. The shear stress causes the most exposed surfaces to suffer a plastic deformation, forming a wave-shaped surface finishes.

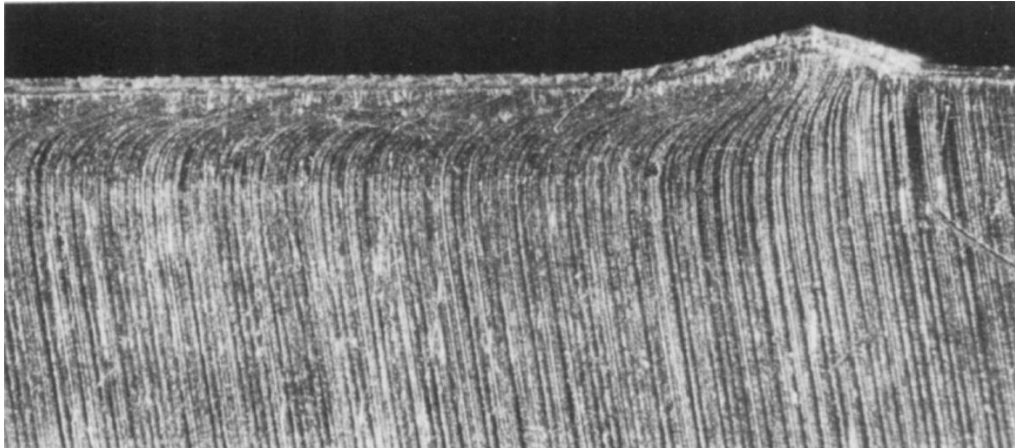


Figure 28. Wave-shaped plastic deformation caused by continuous sliding in early stages of fatigue wear [59]

When the wave propagates through the surface and a limit is reached, the wave can result in a crack that possibly could propagate as all the exposing surface has been deformed and affected by the continuous sliding. The mechanism of this crack appearance and its posterior extension due to the wave-shaped plastic deformation can be observed in Figure 29.

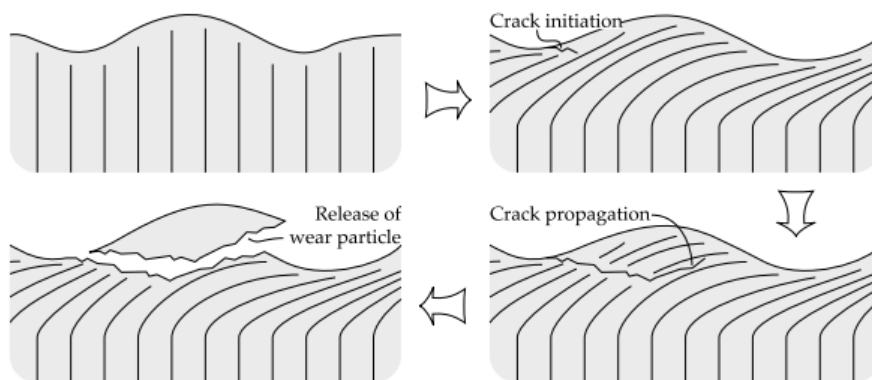


Figure 29. Crack formation and propagation mechanism due to wave-shaped plastic deformation [58]

It can be concluded that the accumulation of that plastic deformation causes fatigue wear as cracks begin to appear and propagated in localized areas of the surface. These cracks may result in delaminated parts of the surface. However, these cracks can be created even in subsurface parts of the material and then propagate from them due to the deformation that is embedded into it. Therefore, dislocations will appear at

microscopic scales and finally cause the generation of a crack. The final release of the worn particle can also induce following cracks into the material since the material left in that zone stays weaker. Other mechanisms of wear can be combined with fatigue wear – a common one in metals is oxidative wear. Formed cracks form tribolayers that prevent the wear volume to increase and even prevent crack propagation as in the end they act as a protective film. However, this can avoid the cracks to be reclosed by affinity. In other cases, when the crack has just been generated affinity between very close crack surfaces can rejoin by an adhesive mechanism [60].

#### 2.5.1.6 Cavitation wear

Cavitation is a phenomena caused via fluid collapse in contact with solid surfaces. It is a very usual behavior in turbine and compressor blades as well as in pumps. It is caused when a fluid achieves a zero pressure or negative pressure (in relative terms) in main situations due to divergent geometries in general. If this pressure reaches a value below the vapor pressure (dependent on the temperature of the fluid), small bubbles are formed due to the evaporation of gas, implode and impact with units' walls causing removal of material.

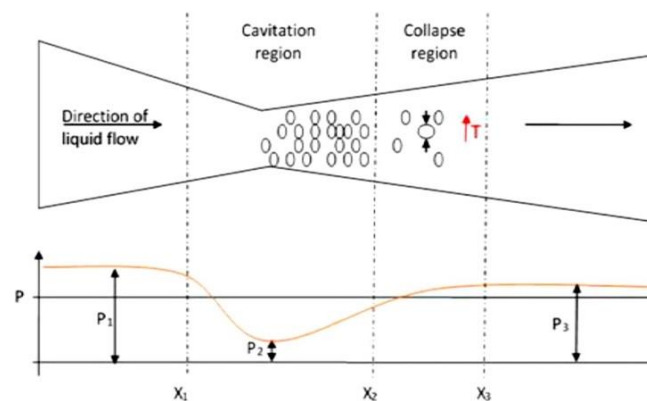


Figure 30. Cavitation phenomena [61]

In case of rotating units such as compressor or turbines, it might happen that in localized parts cavitation is likely to occur cyclically. In such event, the liquid surrounding bubbles is quickly accelerated, the bubble implodes and suddenly the liquid rapidly decelerates and impacts the walls (blades, casing...). That big implosion causes the material to be

pulled off the surface as very high stresses are reached and wear begins. It can even hole the surface.

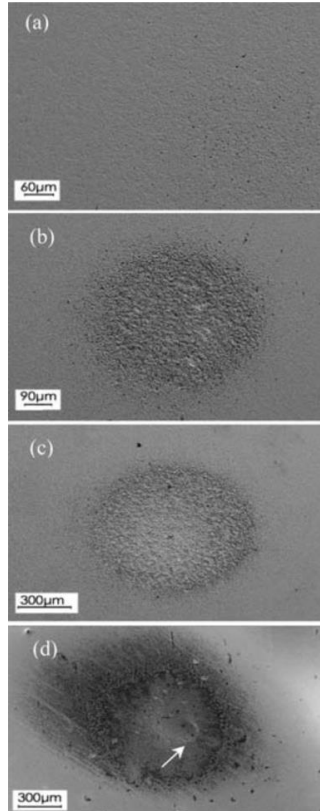


Figure 31. Different stages of a cavitation damage in a surface at different times. a) 1h. b) 3h. c) 5h. d) 8h. [62]

### 2.5.2 Literature review of wear resistance improvement

Once wear mechanisms have been established, the up-to-date wear resistance development and research will be exposed. In the area of metallic fabrication, although every type of possible combination has been tried, alloys coatings and MMCs appear as the best solution. As far as steel is concerned, as for other metals, a softer steel has generally been used as a substrate with harder coatings such as oxides, carbides, nitrides, borides and carbon-based compositions [63]. In that respect, laser-based processes have proven an excellent choice for new coatings and composites. Below some researches about steels, and more particularly 316L and WC coatings, will be discussed with respect to their wear behavior.



- L. J. O' Donnell et al. [64], in addition to building a wear map for carburized 316L, showed that the poor wear resistance that 316L possesses can be improved by low temperature carburization due to increasing yield stress given by the carbon interstitially embedded. Moreover, that reinforcement allows that the wear is improved in a wide range of dry-sliding conditions, increasing the material tribological behavior.
- S. Q. Wang et al. [65] proposed a new approach in oxidative wear of steels as a new wear map was developed with a new transition area between the oxidative mild wear and severe wear. Since oxidative wear in steels is an elastic wear phenomena, the region of transition is difficult to find. However, it begins from the very slight plastic deformation of the substrate but with a primary oxidative wear behavior. Then, with increasing load and speed, the transition zone gradually appears.
- D. Gu et al. [66] studied the wear behavior of SLMed specific steel with WC particulates reinforcement, observing that the resulting microstructure enhanced the mechanical properties of the bulk steel with WC to matrix graded carbide microstructure. A graded material with good bonding between both compounds was also obtained. Consequently, optimal parameters were obtained with reduced coefficient of friction and low wear rate in comparison to other parameters and bulk steel, with better results with the composite solution.
- X. Tong et al. [67] proved Laser Surface Alloying (LSA) to be a very good choice for reinforcing materials in order to improve its wear properties. This is obtained as the laser provided very fast solidification and fine microstructure along with the reinforcement particulates. WC particles of different size were used. It was concluded that the bigger the WC particles the better wear resistance was obtained. However, there is a size top limit in where the wear resistance is enhanced, and bigger size particles than that size do not improve more.

- Wear behavior of bulk 316L was studied by A. Jouraini et al. [68] by abrasive papers and sandpapers. It was observed a transition from adhesive wear to abrasive wear depending on the size of the abrasive grains, having more adhesive wear in fine sandpapers. In that respect, the friction coefficient decreases with the increasing normal load. This is seen in sandpapers: the normal load is decreased and the friction increased. It was also obtained that the smaller the grains, the higher wear resistance.
- D. Mario's master thesis [1] consisted in studying the wear of laser cladded 316L with WC particles reinforcement. It was possible to study all the wear mechanisms and behavior with respect to an alumina counter body. Abrasive, adhesive and delamination wear were observed with interrupted wear tests as well as the appearance of the tribolayer during the wear test.
- F. Li et al. [69] were capable to apply Plasma Transferred Arc (PSA) technology to build steel based coatings reinforced with WC particles. Higher density of WC particles caused them to concentrate at the bottom of the coating not achieving a homogeneous distribution. In spite of that, it was possible to conclude that the addition induces an increase in microhardness and an improvement in the wear behavior. This wear was predominantly adhesive and oxidative wear, with slight behavior of abrasive wear. Furthermore, they observed that increasing percentage of WC particulates will cause brittleness to the composite and three-body abrasive wear would be the main mechanism due to a higher amount of WC particles being pulled off and fractured.
- F. Bartolomeu et al. [70] made a comparison between conventional cast, hot pressed and selective laser melted 316L. In every mechanical properties tested (yield strength, tensile strength, hardness and wear rate) the SLMed sample was the best.

- The DC plasma nitriding (DCPN) was tried in 316L substrate by G. Li et al [71]. A CrN nitride layer was obtained preventing the steel to be affected and the wear behavior was improved, changing the main mechanisms that appear in the nitrided sample (plastic deformation and little abrasion) in comparison to the not nitrided one (abrasive, adhesive and oxidative wear).
- 304 steel reparation was made possible by L. Song et al. [72] via laser cladding. The repair material was a 316L steel powder combined with WC powder. The results indicate that all the mechanical properties of the repaired zone were improved with respect to wear behavior. The best results were obtained in the sample with higher WC content (24,4% wt.). Furthermore, abrasive wear became the main wear mechanism as the higher hardness of the WC compared to the softer steel substrate.
- A tool steel was coated by Domitner et al. [73] first by a nickel intermediate layer cladded onto the surface and secondly with a MMC as the top layer containing WC particulates into the nickel matrix, leading to better wear performance. The carbide particles were observed in different stages of the process along with their brittle fracture in comparison to the softer matrix (Figure 32).

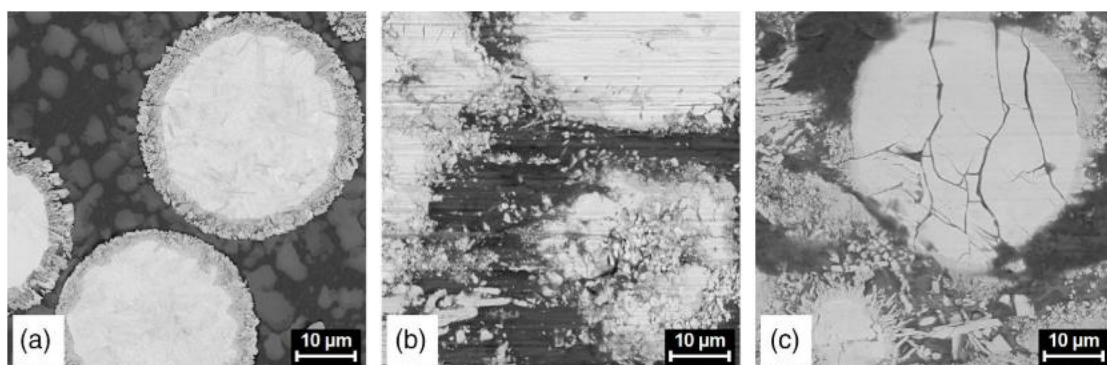


Figure 32. Carbide particles. a) After cladding. b) After machining. c) After first wear test [73]

### 2.5.3 Wear testing methods

The need of establishing the wear behavior of a given material has developed different apparatus and techniques. Those techniques try to approximate the working conditions

in terms of wearing the surfaces. In that respect, they differ in many aspects so that the results obtained are those for which the test was performed. These machines are also known as tribometers.

### 2.5.3.1 *Pin-on-disk*

It is the method used in this thesis and it is the most used testing machine available in the market. The sample, being rotated and acting as the disk, is worn by a fixed ball/pin that generates a wear track. A wide variety of materials is available for the balls: sapphire, ruby, alumina, SiN, SiC, zirconia, WC and stainless steel are the most used [74]. The choice of which material is being used depends on the sample testing but generally it is common to choose a material that is supposed to be worn less than the sample. V. Saikko [75] developed a rotating translating pin-on disk which allows to test at a time multiple samples with translating unique pin arms.

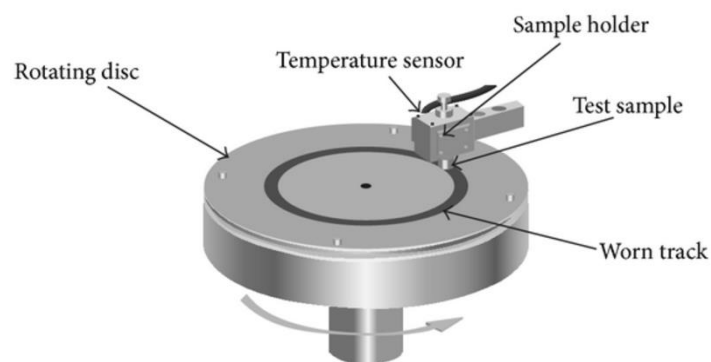


Figure 33. Pin-on-disk testing machine scheme [76]

There are several variations of the pin-on-disk common one: disk-on-disk, ball-on-disk, roll-on-roll and even ring-on-boost.

### 2.5.3.2 *Four ball tester*

Load is applied in the top ball while it rotates. The other three balls are fixed and sunk in lubricant. The aim of this test is to study the antiwear properties of the lubricant rather than to know the wear behavior of the ball material.

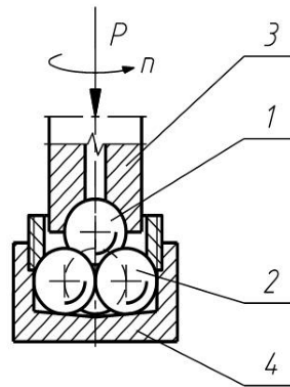


Figure 34. Four ball tester scheme [77]

### 2.5.3.3 Reciprocating sliding friction

It is a similar concept to the pin-on-disk test: the ball slides into one longitudinal direction and the contrary every time, having a reciprocating sliding that causes the material to be worn.

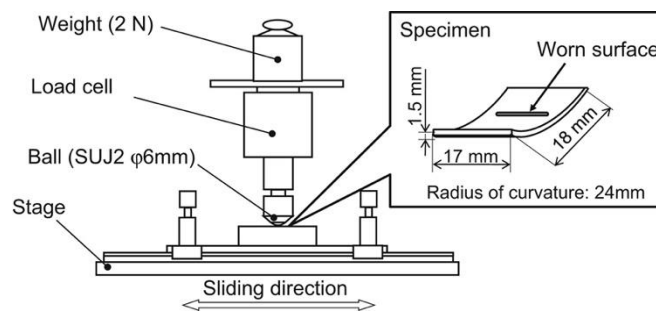


Figure 35. Reciprocating sliding test scheme. Data specific of [78]

### 2.5.3.4 Fretting wear testing machine

Fretting is a wear caused by minute displacements under load sustained by two fractioned surfaces, caused for instance by very low-amplitude vibrations. In that respect, this apparatus needs high accuracy as the displacements have to be very small and exact.

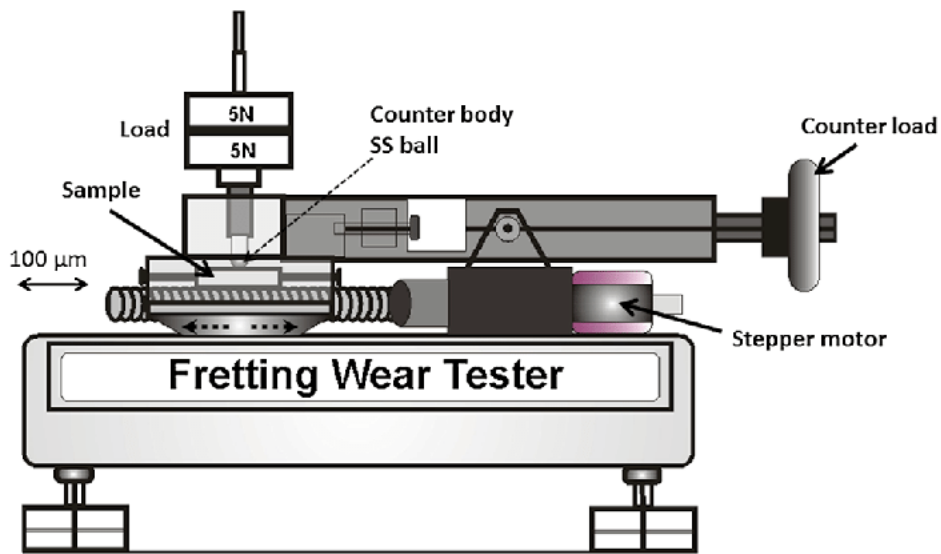


Figure 36. Fretting wear testing machine scheme. Data specific of [79]

### 3 MATERIALS AND METHODS

#### 3.1 Samples

15mm thick deposits were produced by laser cladding combining the WC powder and the 316L powder and fabricated at the Sirris based in Seraing. Both powders were provided from Höganäs [80]. In this respect, both powders' chemical compositions are given in Table 4 and Table 5, with the data sheets in D. Mario's thesis [1].

	<b>Fe</b>	<b>C</b>	<b>Cr</b>	<b>Mo</b>	<b>Ni</b>	<b>Mn</b>	<b>Si</b>
<b>min.</b>	Bal.	-	16.0	2.0	10.0	1.0	-
<b>max.</b>		0.03	18.0	3.0	14.0	2.0	1.0

Table 4. 316L powder chemical composition in wt% [1,80]

	<b>W</b>	<b>C</b>	<b>Fe</b>	<b>Others (Total)</b>
<b>min.</b>	Bal.	3.5	-	-
<b>max.</b>		4.2	0.5	0.2

Table 5. WC powder chemical composition in wt% [1,80]

As data sheets show, the range of particle size for 316L varies between 45 and 150  $\mu\text{m}$  and between 45 and 180  $\mu\text{m}$  for the WC powder. Both annexes in D. Mario's thesis [1] provide the percentage of the variability of the size with a majority between 63 and 125  $\mu\text{m}$  for the 316L and between 45 and 150  $\mu\text{m}$  for the WC powder. Regarding the shape of the particles, it was ensured that all the particles have a spherical shape in order to avoid any type of abrasion by the particles and a consequent damage of the cladding machine's nozzle, deposits and pipes.

The samples were fabricated in a parallelepipedal shape, with variations in height (depending on the process parameters) but similar among them. The technique used for tracks fabrication was a zigzag one and is illustrated in Figure 37.

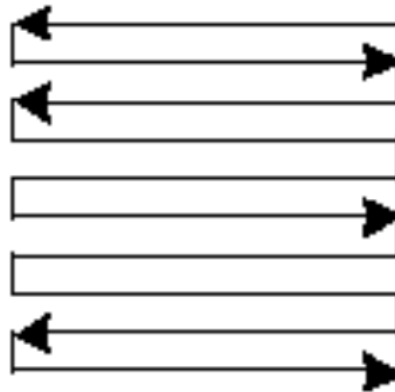


Figure 37. Zigzag technique used for samples fabrication [4]

In Table 6 fabrication process parameters and final height is given:

Sample name	316L powder rate [g/min]	WC powder rate [g/min]	Total powder rate [g/min]	WC vol% in the final sample	Height [mm]
W20.15	14,7	7,6	22,3	20	15
W20.18	14,9	7,3	22,2	19,2	14,6

Table 6. Samples fabrication process parameters and final characteristics

All the samples were tested with a load of 10N, except for one in W20.18 whose test was performed under a load of 20N to determine the differences in the wear process among the results. These samples were studied as well by means of profilometer and observed by the SEM to get insights in the wear mechanisms. W20.24 section 3 [1] was considered for microstructure characterization.

### 3.1.1 Samples preparation for microstructural characterization

The sample used for microstructural characterization was cut from the bulk deposit. Cross-section 3 was analyzed in order to state the quality of the deposition. The cut part is embedded in bakelite by means of a STRUERS Citopress-1. After that, the cross section surface is polished, etched and cleaned in order to observe the microstructure by optical microscope. The polishing was made on a STRUERS Tegramin-30. The etching consists in aqua regia, a mix of 60 ml of HCl and 20 ml of HNO<sub>3</sub> during 5 seconds. The final



preparation is made on the PRESI vibrometer in order to remove the work-hardening layer formed by the previous preparation steps. This final step is mandatory as a colloidal solution containing silicon dioxide that cleans microimpurities present on the surface even after all the previous preparation.

a)



b)



Figure 38. a) Struers CitoPress-1. b) Struers Tergamin-30 [81]

### 3.2 Optical microscope

The optical microscope used for microstructural characterization purposes was the Olympus BX60. The magnifications used for the samples characterization were 2.5x, 5x and 10x. Different magnifications induce different scales at the microstructural grade: different magnifications are required due to different objectives of observation.



Figure 39. Olympus BX60 optical microscope [82]

### 3.3 Scanning Electron Microscope

Apart from the previous mentioned optical microscope, the Philips XL30 ESEM FEG scanning electron microscope (SEM) was also used. As for the optical microscopy, the previous polishing, etching and cleaning is the same for SEM analyses. Different modes were used by this microscope and its unified software for different purposes:

- Energy Dispersive Spectrometry (EDS) served to obtain the chemical composition (in atomic and weight %) of a localized part of the sample (for instance, gradual composition between the carbides and the matrix).
- Back Scattered Electrons (BSE) mode, by which high energy electrons are reflected from the surface they are being beamed at, due to an alteration of these reflected: heavier atoms in the surface reflect stronger the electrons, and thus these atoms are shown brighter in the image obtained and darker for lighter atoms.
- Secondary Electrons (SE) mode, which allows to have a better visual of the topography of the sample studied. Therefore, it is very useful for track analyses.



Figure 40. Philips XL30 ESEM FEG. Courtesy of <https://www.mtm.kuleuven.be/equipment/ESEM-XL30-FEG/ESEM-XL30-FEG>

Furthermore, the SEM also was used for characterizing the worn tracks of the tested samples and observing the possible appearance of the tribolayer.

### 3.4 Profilometer

The profilometer is used every time after a surface is completely tested and the sample is properly cleaned of wear debris (which is removed and then kept in a recipient for SEM purposes) and any kind of dust which can appear after the test. Once done, the worn surface is analyzed by the profilometer available in the lab: Alicona InfiniteFocus G5 profilometer, observable in Figure 41. It uses a non-contact, optical, 3D measurement principle based on Focus-Variation technology. Citing Alicona's product website, *"Focus-Variation combines the small depth of focus of an optical system with vertical scanning to provide topographical and color information from the variation of the focus"*. [83,84].



Figure 41. Alicona InfiniteFocus G5 plus profilometer [84]

It reaches up to a 100x magnification, but for our testing purposes only 5x, 10x and 20x magnifications were used. This machine allows to perform 3D images of the worn tracks which are really visual, as well as being capable of measuring depth of those tracks and the computation of the worn volume in the counter body ball and in the surface of the

sample. Even if the counter body ball does not wear as much as the surface, the profilometer, with a proper analysis with its software tools and the use of the volume equation of a spherical cap, can compute the worn volume of the ball.

$$V = \frac{\pi h^2}{3} (3r - h)$$

Where  $h$  the height of the spherical cap worn and  $r$  the radius of the ball, this latter value being in all cases 3mm. In some cases, the calculation of the profile of the ball was compromised as the machine uses light to get the images and the high reflectivity of the balls prevented some of them to be fully usable. However, good results with repeatability and calibration was obtained.

### 3.5 Hardness testing machine

Hardness measures were taken in order to evaluate its variation as function of the height and its relationship with the carbides distribution observed by optical and electron microscopy, based on the work done on [1]. Hardness measurements were performed the EMCO M1C 010 digital low-hardness testing machine was used.

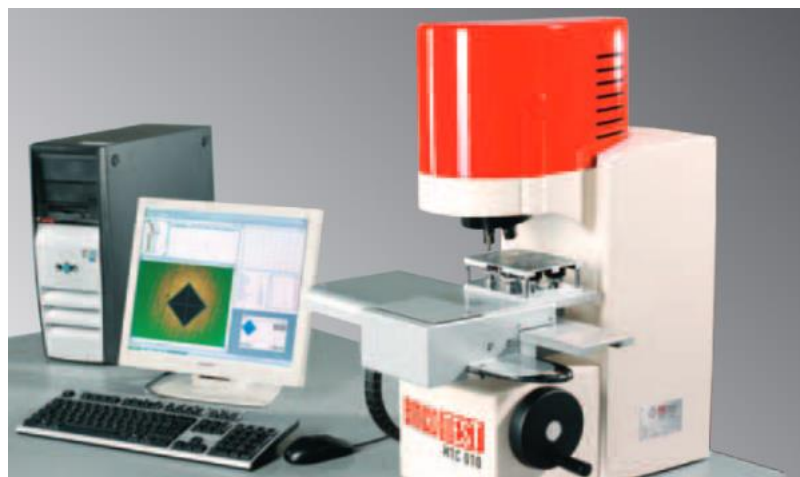


Figure 42. EMCO Test M1C010 hardness testing machine [85]

For this characterization, instead of a indents grid with a required standard separation as in [1,2], the indents were carried out at each layer without considering the perturbed volumes. For the studied samples, the separation between indentations was of 2mm.

### 3.6 Tribometer

After characterization of the microstructure of W20.24 3, wear tests were performed by the tribometer. The wear samples used for wear tests were obtained by cutting the bulk deposit at specified heights [1]. These cuts, then, were grinded and their surfaces were cleaned with ethanol before introducing them into the tribometer machine. The designation used for them was:

- **Name of the sample** (W20.xx), where 20 means 20% volume of WC and xx is the sample number.
- **F or H**, which states from where was the sample obtained by cutting, at **Feet** or **Head** starting from the substrate. It is visually interpreted by Figure 43.
- Distance from the substrate at where the surface is obtained by cutting. In our case **1.3**, **6.3** and **11.3** mm are the measures reached by compromise. In this case it can be visually interpreted better on Figure 43 as well.

As an example, one sample can be named as W20.18 H6.3, which means that it is the sample number 18 of the group of 20% vol of WC and the top sample (head sample) whose face is 6.3mm from the substrate.

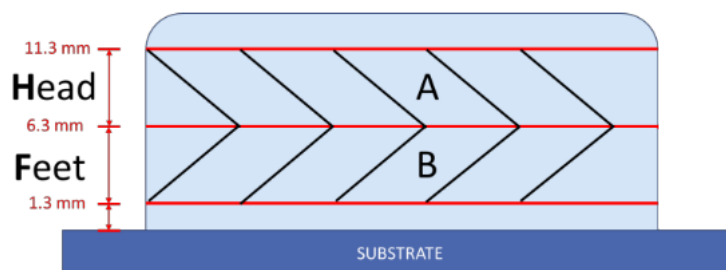


Figure 43. Sample denomination system. Obtained from [1]

In that respect, from every bulk samples four surfaces are obtained.

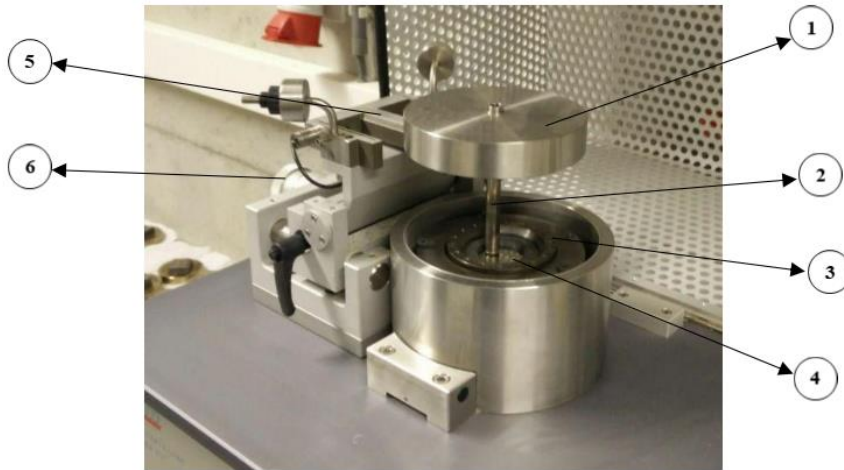
The tribometer used to perform these tests is the High Temperature Tribometer 01-04611 manufactured by CSM Instruments [74], which has a pin-on-disk configuration, having all the samples tested at room temperature but with different characteristics. The different tests parameters are given in Table 7:

Test N.	Name of the sample	Speed [cm/s]	Load [N]	Radius [mm]	Interruption cycles
1	<b>W20.18 H6.3</b>	10	10	8	22000 (uninterrupted)
2	<b>W20.18 H6.3</b>	10	20	11	220000 (uninterrupted)
3	<b>W20.15 F1.3</b>	10	10	8	22000 (uninterrupted)
4	<b>W20.15 F1.3</b>	10	10	11	11000
5	<b>W20.15 H6.3</b>	10	10	8	8000
6	<b>W20.15 H6.3</b>	10	10	11	16000

*Table 7. Preliminary tribometer parameters of wear tests*

The interruption points were chosen after three preliminary uninterrupted tests at 22000 cycles. The points were chosen analyzing the variation of the friction coefficient ( $\mu$ , CoF) and the penetration depth.

The counter body used in the tests are WC balls of 3mm of radius, which are located into the pin holder [74], which allows perpendicular contact between the ball and the surface. In that respect, these balls were analyzed after tests with the profilometer as well in order to compute the worn volume for each wear test.



- |                        |  |
|------------------------|--|
| 1. Adjustable weight;  | 4. Sample;   |
| 2. Pin or ball holder; | 5. Tribometer arm;   |
| 3. Locker ring;        | 6. Crank-handle for the adjustment of the friction radius. |

Figure 44. HTH Tribometer 01-04611. Obtained from [1]

## 4 RESULTS

### 4.1 Microstructure characterization

W20.24 section 3 sample was considered for microstructure characterization. The cross section prepared for observations is parallel to scanning direction. Each layer may be distinguished from others if well cleaned and etched. Both Optical Microscopy and the Scanning Electron Microscopy were used for this characterization, in order to take considerations for further analyses.

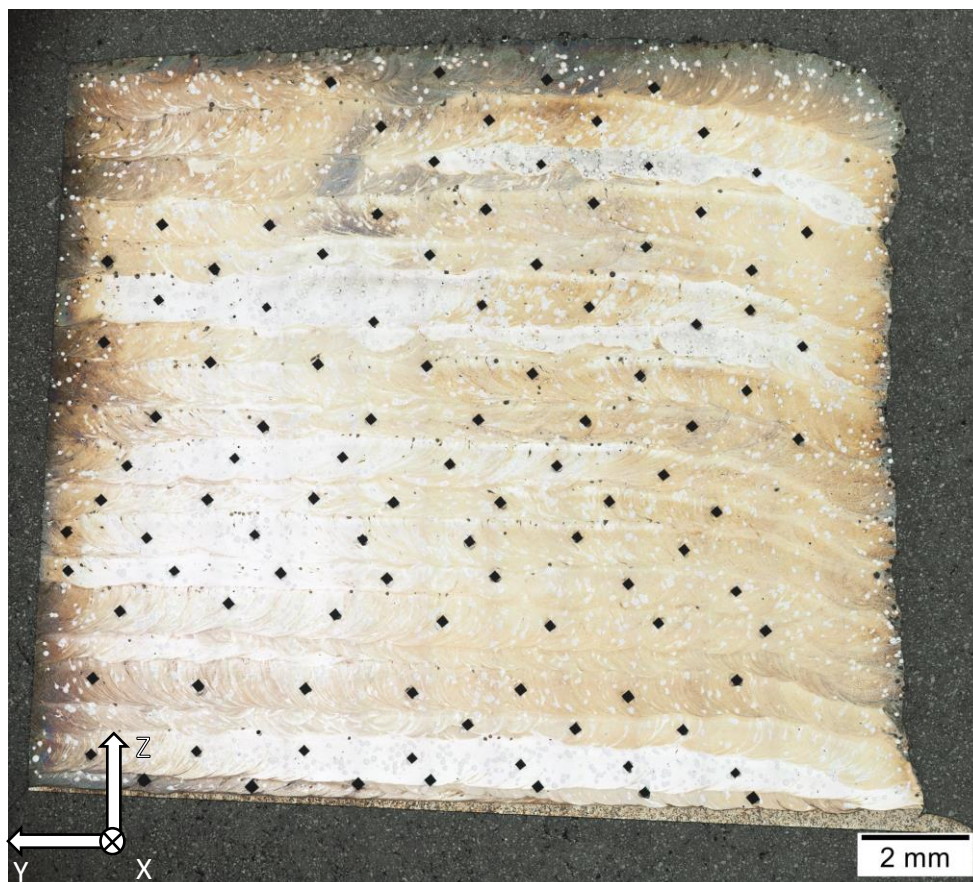


Figure 45. W20.24 section 3 sample after macro hardness test. 5x overview via OM

#### 4.1.1 Optical microscopy

Figure 45 shows a general overview of the W20.24 section 3 sample, in the YZ direction. As mentioned in [1], Y is the building direction and allows observing almost entirely the 19 tracks overlaid one over the another. Some layers may be partially hidden by others



due to the overlaying of the deposition strategy. Several observations were made in different parts of the cross section.

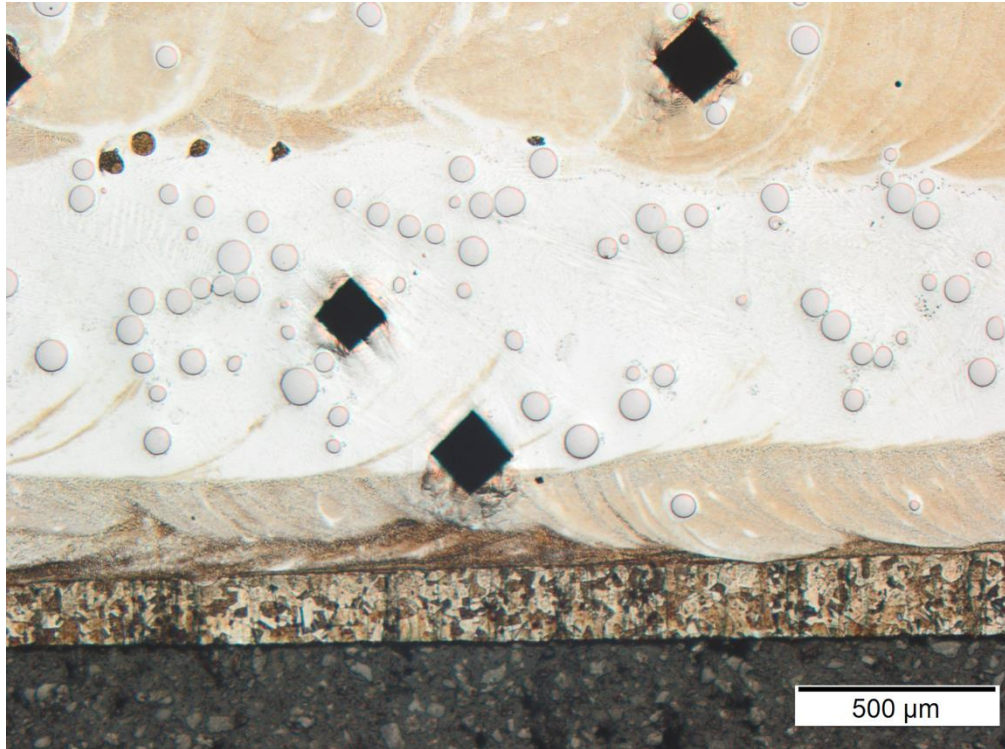


Figure 46. Layers 1, 2 and 3 on W20.24 section 3. 2.5x magnification

Figure 46 shows the layers closer to the substrate and a high carbide presence at the second layer. As reported in [86], this is due to not reaching stable values in the powder stream in the early moments on the deposition or a sudden high quantity of large WC particles, thus leading to heterogeneities in lower layers of the deposit. Indeed, as shown in Figure 48, at the top of the cross-section, another layer is observed with a large quantity of reinforcements. Nevertheless, this problem is rare and most of the microstructure in the sample exhibits WC carbides are well-distributed in the matrix, as shown in Figure 47.

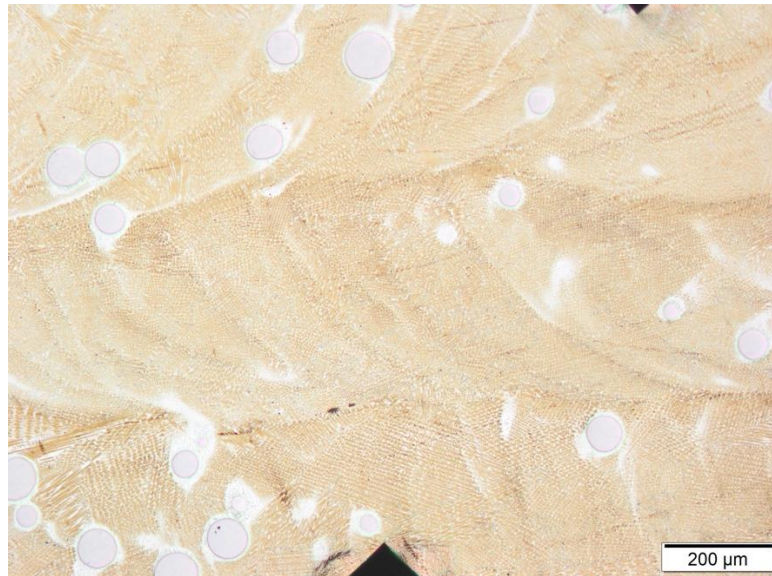


Figure 47. 5x overview in upper layers on W20.24 section 3

The color of the layer after etching also shows brighter colors.

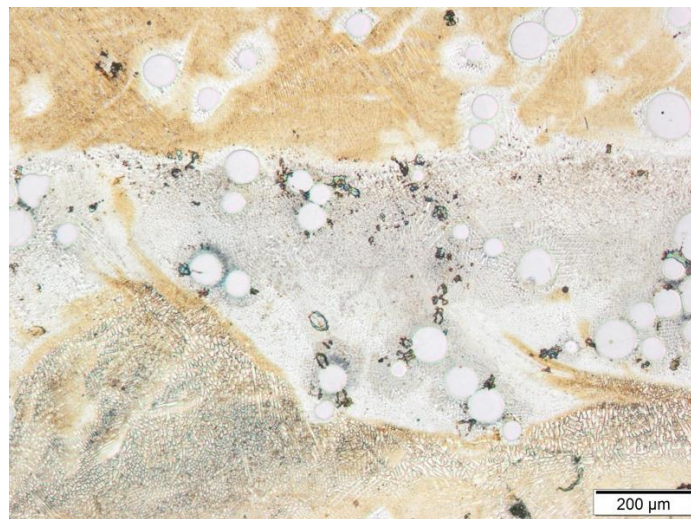


Figure 48. "Traffic jam" of big WC particles in 17th layer

Figure 47 also exhibits some white surrounding zones near the WC particles. As commented on 2.4.2 section about the cladded 316L+WC microstructure, the white zone surrounding the particles is associated to the carbide crown formed around the WC particles. However, as reported in [86], there are long white zones which end in the carbide crown that can be associated to "carbide tails" (Figure 49), which are created during the solidification and indicate the movement the particle has done in that process.

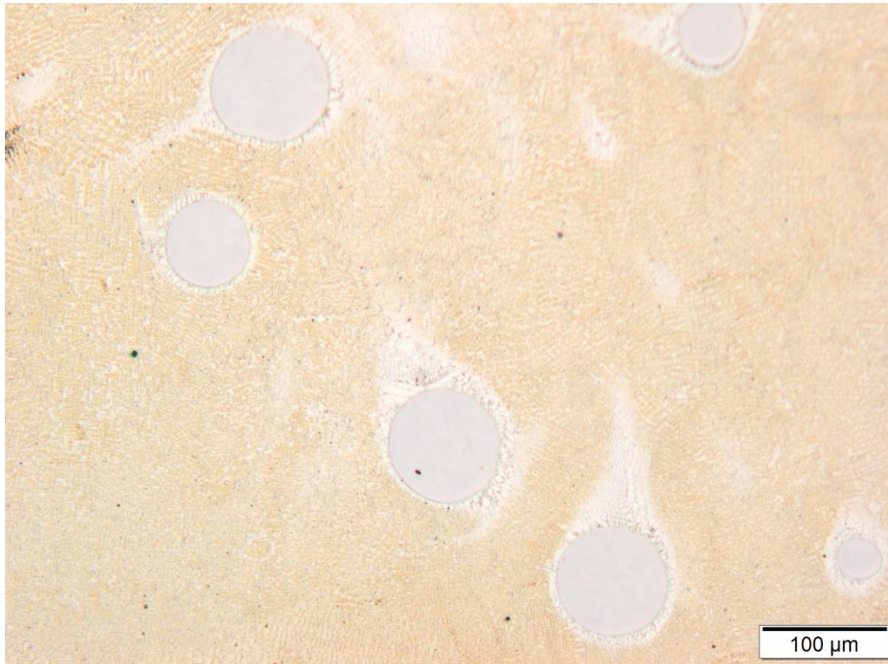


Figure 49. "Carbide tails" observable via 10x magnification on W20.24 section 3

#### 4.1.2 Scanning Electron Microscopy

The morphology of the carbides created due to the partial dissolution of the WC particles is observed by means of SEM observations. Figure 50a shows the same area reported in Figure 46.

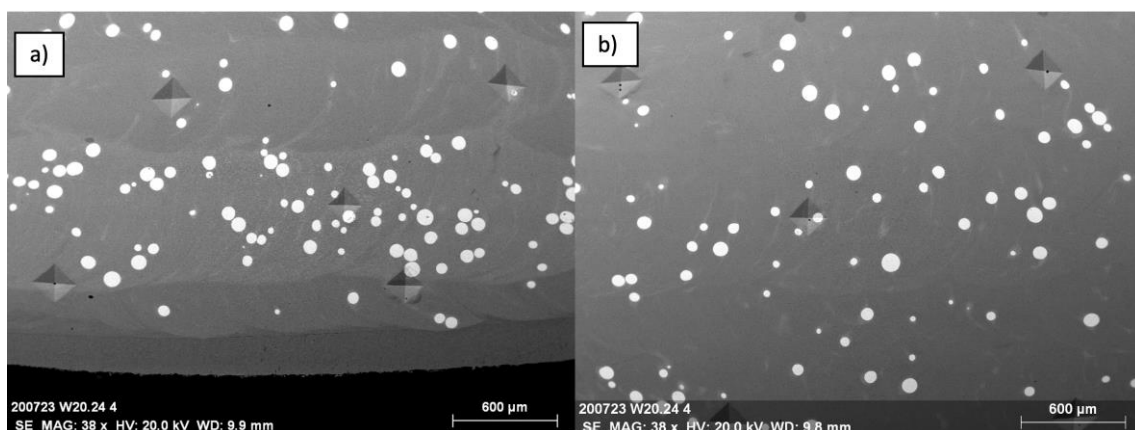
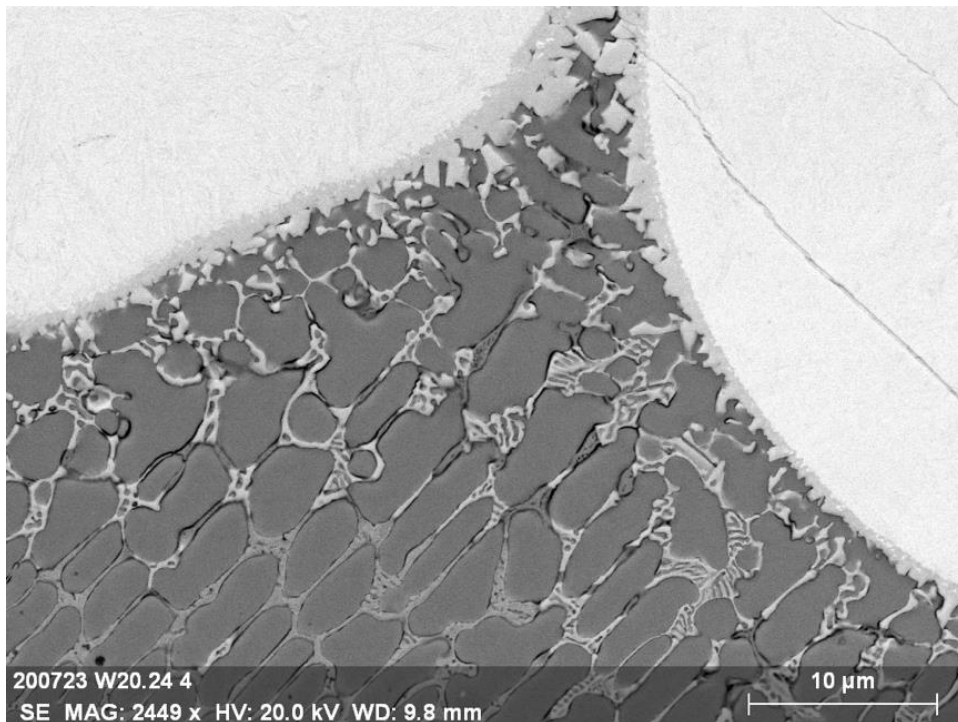


Figure 50. a) SEM micrograph related to Figure 46. High carbide density can be observed on the 2nd layer. b) SEM micrograph of W20.24 section 3 of upper layers showing more homogenization in WC carbides

The WC carbides are partially dissolved during the solidification and this enriches the composition of the parent 316L, leading to the precipitation of solidification carbides during the solidification, as mentioned on section 2.4.2. The carbides here show the transition zone observed on [1,53], containing the carbide crown and following lamellar skeletal carbides. Complex regular carbides are observed out of that transition zone Figure 51.



*Figure 51. Carbides distribution from the carbide crown to the outside part of the transition zone*

As shown in [1,2], the HAZ exhibits different carbide morphology: white rodlike and grey eutectic [53]. They are formed due to different thermal history of this zone (Figure 52). A peculiar spot is observed in this figure as well: one WC carbide particle is completely affected by the next track deposition, having its upper part completely deformed and dissolved.

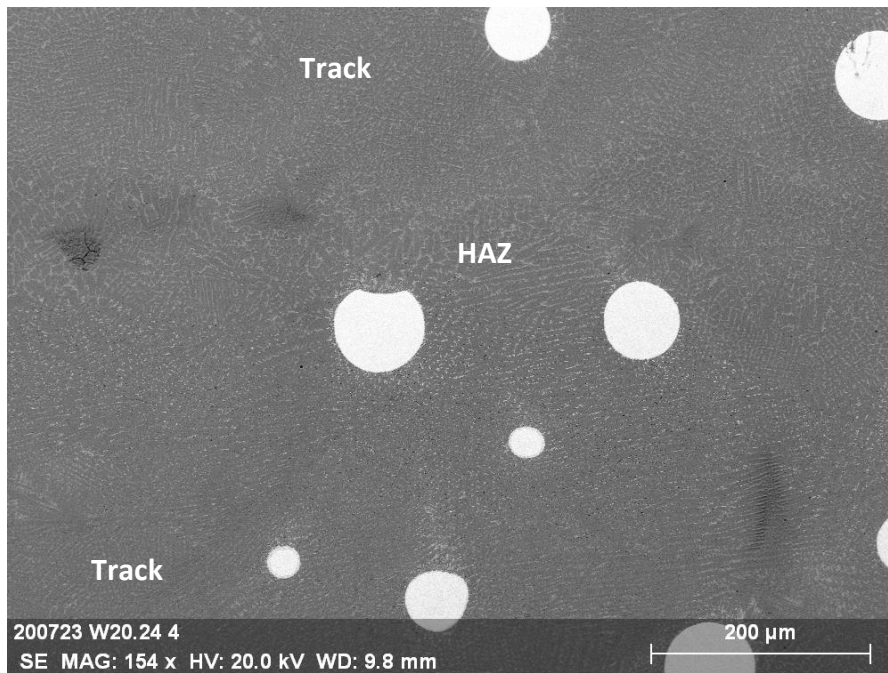


Figure 52. HAZ carbides differentiation

As mentioned in 4.1.1, the microstructure is generally homogeneous. Nevertheless, few areas with heavy “traffic jams” and thus high number of WC carbides exhibit very complex and variable carbide structures near those zones (Figure 53).

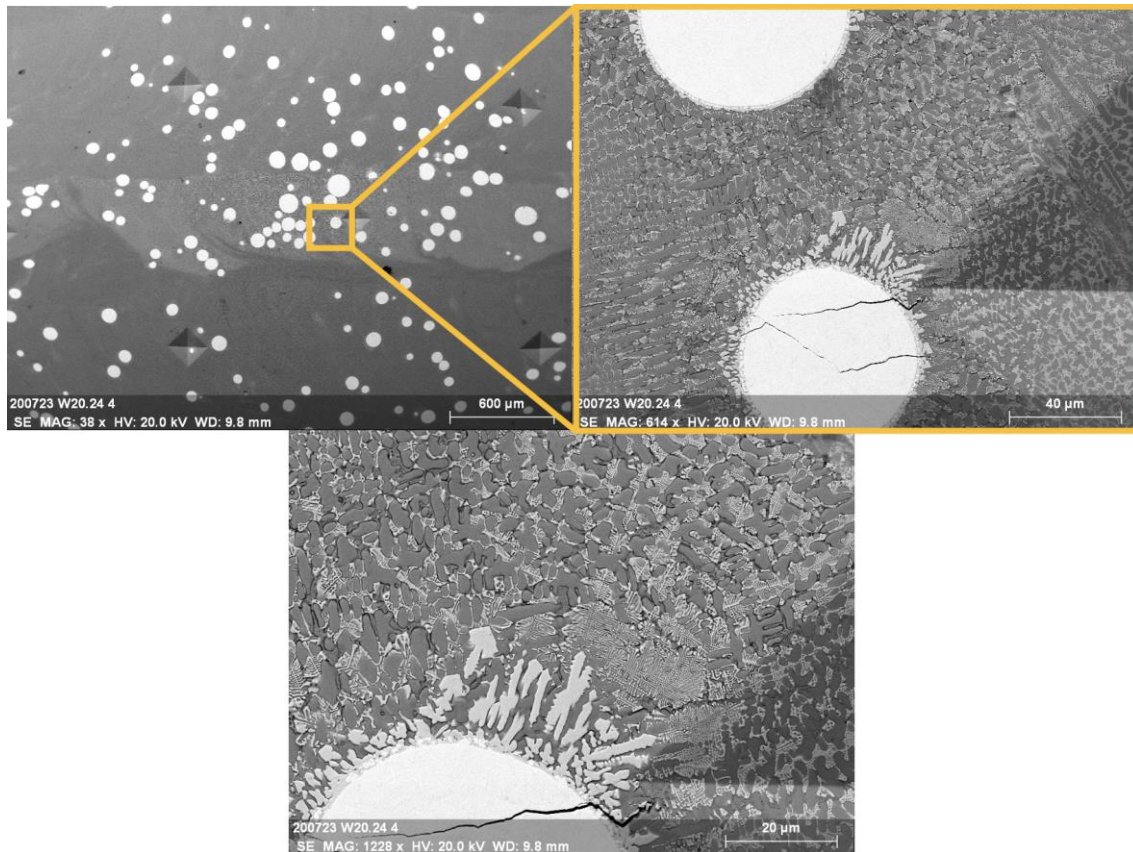


Figure 53. SEM micrograph of a traffic jam of carbides area

The carbide tails can be also observed with SEM micrographs, showing the path the carbides had followed and how they have affected the matrix in that path (Figure 54), as reported in [86].

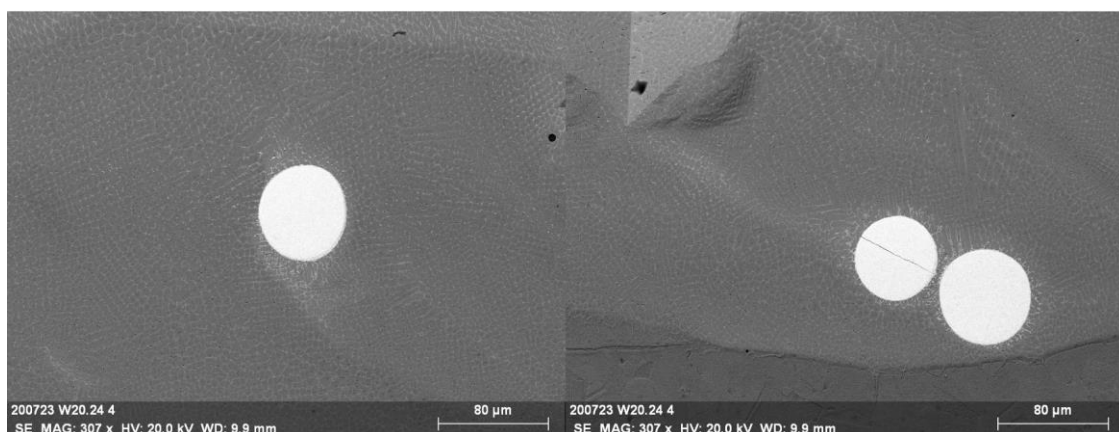


Figure 54. Carbide tails observable by SEM micrograph

## 4.2 Macro hardness test

Figure 45 exhibits the W20.24 section 3 sample post-hardness test. A distance of 2mm was set horizontally in order to avoid overlapping of the affected zones by previous indentations. The purpose was to assess the hardness of the different layers. Indentations do not show a perfect alignment between them though. Moreover, if well analyzed, 2 layers of the sample were not indented since, in this cross-section, they were hidden by the overlapping of the deposition strategy.

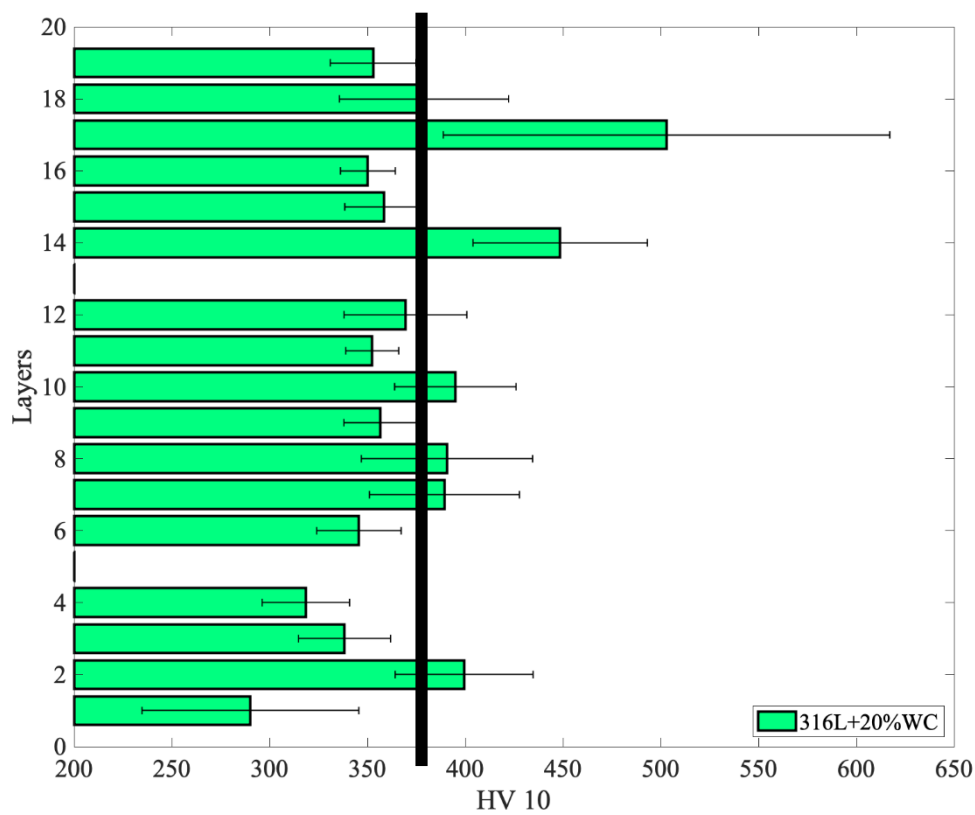


Figure 55. Macro hardness test results for W20.24 section 3

The results of the test are given in Figure 55. Some specific layers exhibit higher hardness values than the overall mean value (layers 2, 14 and 17). Observing the overview in Figure 45, those layers have a larger quantity of carbides and exhibit brighter colors. As shown in section 4.1.1, layer 17 contains a large amount of big WC particles, resulting in such high values of hardness observable in Figure 55. Nonetheless, the general trend of the hardness is an increase from the first layers up to the 8<sup>th</sup> layer, and a slight decrease

upon increasing the height of the sample. The average hardness value obtained is of 372 HV.

### 4.3 Wear tests

As previously mentioned, several tests were taken out in order to obtain the wear behavior of the laser clad 316L + 20% WC against WC ball as a counter body. The results obtained in [1] can be used and will be further compared with the results of this work in the section 5 since the parameters of the tests are the same.

#### 4.3.1 Tribometer analysis

Both uninterrupted and interrupted tests were carried out, hence a split between both types of test will be shown for a better understanding.

##### 4.3.1.1 Uninterrupted tests

###### 4.3.1.1.1 10N tests

The first test was taken out on the W20.18 H6.3 sample at 8mm radius. This test was used as reference for the next tests.

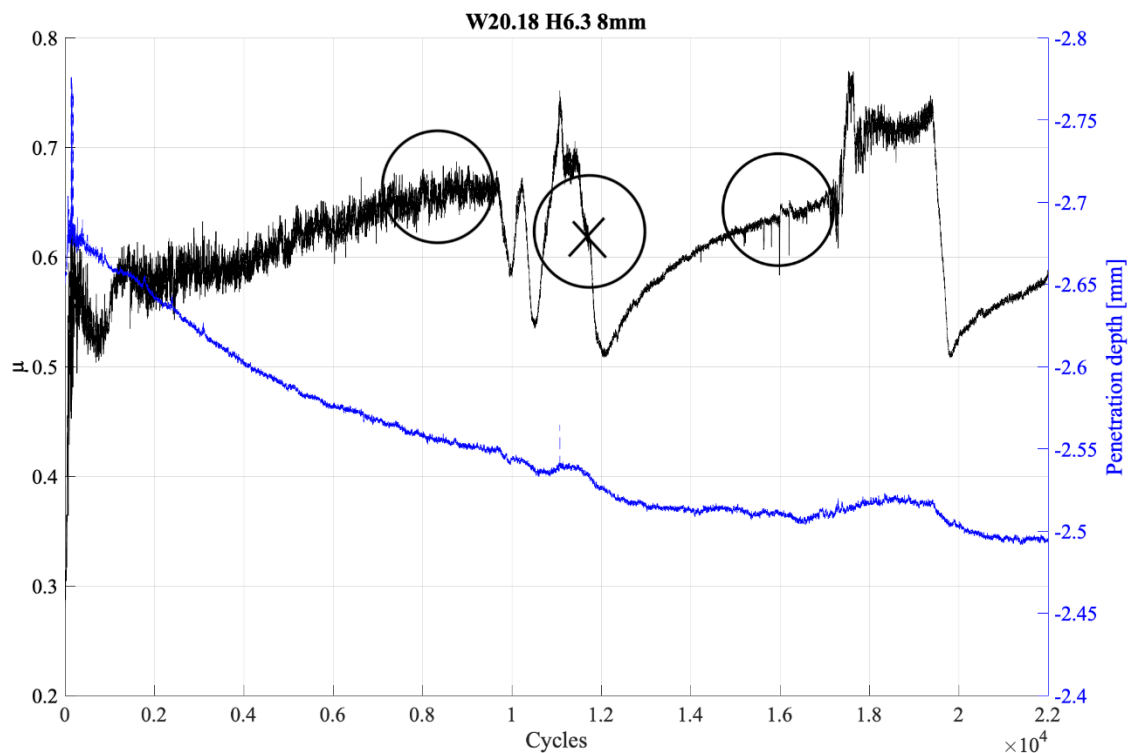


Figure 56. Interest points chosen for posterior tests. Based upon W20.18 H6.3 8mm



Three interest points (i.e. before first peak, in a continuous stable increasing of CoF etc.) were chosen based on previous works [1,2] and peculiar variations of both CoF and penetration depth (i.e. growing of CoF, constant penetration depth etc.). With increasing number of cycles, the chosen interrupted tests are:

1. At the continuous increase of CoF, before the sharp changes of CoF at ~ 9500 laps.
2. At the first sharp changes of CoF, where the penetration depth remains constant and before the decrease in the depth restarts. The point is approximately at ~ 11000 laps.
3. The third interest point is placed where the penetration depth becomes overall constant and the CoF exhibits the second continuous increase.

Moreover, a further uninterrupted test was carried out in order to check the repeatability of the measurements. Based on [2], this second uninterrupted test was performed on the surface at 1.3 mm of height, while the first uninterrupted test was carried out at 6.3 mm of distance from the substrate. Indeed, in this study surfaces at different heights have shown a good reproducibility of the CoF variation during the tests. The second uninterrupted test is given in Figure 57.

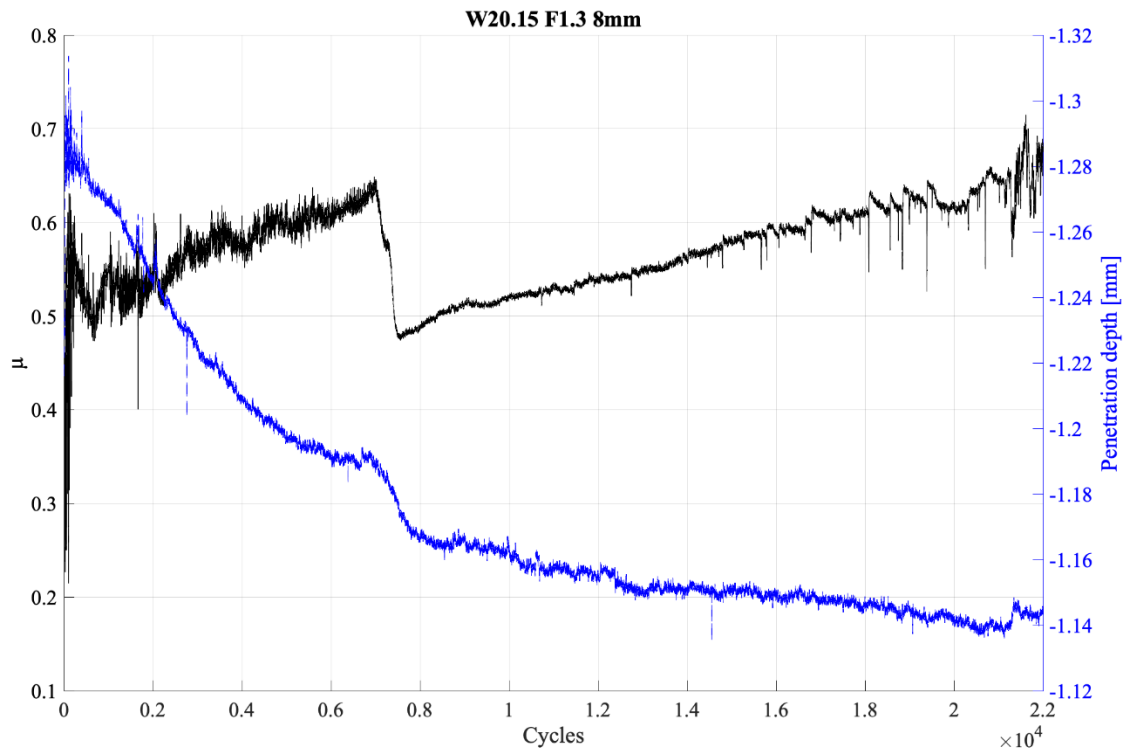


Figure 57. Coefficient of friction and penetration depth for W20.15 F1.3 8mm

Observing both graphs, penetration depth shows similarities. Indeed, in both graphs the penetration depth initially decreases and then stabilizes. The variations of CoF are overall similar, but with few sudden changes missing in the second test. The differences in CoF might be due to the differences observed in [86], but it will be further discussed in section 5. Nevertheless, both show the same stages:

- A first transitional increase of the CoF, followed by a slight decrease and a further continuous increase of it. During this stage of the test, the penetration depth strongly decreases.
- After the continuous increase of CoF, the two graphs (W20.18 H6.3 8mm and W20.15 F1.3 8mm) are different. The CoF curve exhibits more sudden variations in W20.18 H6.3 8mm in comparison to W20.15 F1.3 8mm, but both curves exhibit the remarkable CoF drop (point 2) observed in Figure 56 and Figure 57. Furthermore, the penetration depth curves exhibit the same trend. Both curves

show a sudden increase on the depth, then keeping a constant depth and when the CoF drop occurs, it drops as well.

- After point 2, the CoF exhibits again a continuous increase and its noise is reduced in comparison to the first continuous increase. The increase ends with noisy and similar drops in both graphs. These strange peaks can be observed on the 3<sup>rd</sup> point of interest described before.
- After that, the pattern of the wear behavior is repeated. Nevertheless, this cyclical period cannot be observed with the W20.15 F1.3 8mm test, the early stages are overall similar.

#### 4.3.1.1.2 20N Uninterrupted test

All these tests have been made with a load of 10N, but a further test with a 20N load was carried out on the W20.18 H6.3 surface, in a radius of 11mm.

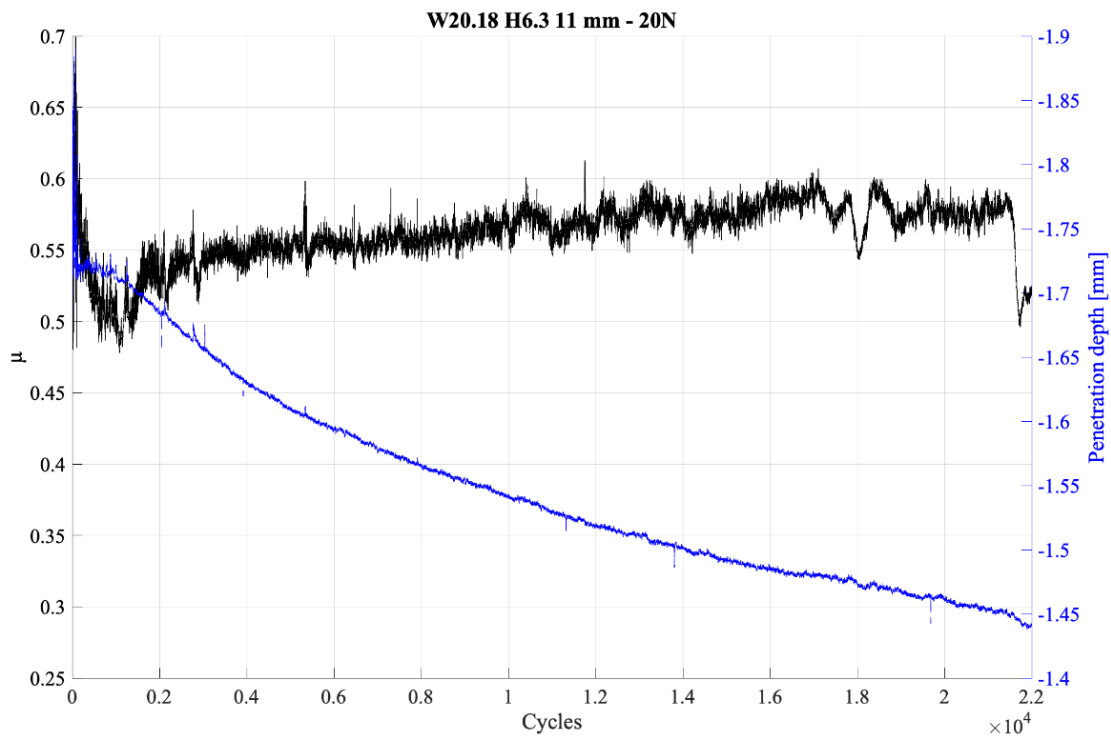


Figure 58. Coefficient of friction and penetration depth for W20.18 H6.3 11mm

Figure 58 exhibits the differences among all the interrupted tests and this one. As observed, the unique similarity is the initial variable changes on the CoF among W20.18 H6.3 11mm and the others. It keeps a constant value of CoF during the whole length of the test, with sudden and short changes at certain times. However, it is concluded that 20N tests do not serve as relevant information for understanding general wear behavior of the material. The excessive load does not allow the material to evolve and practically it gets worn more and more, as will be shown later in section 4.3.3.

#### 4.3.1.2 Interrupted tests

The results of the interrupted tests, based on the points chosen, are given in Figure 59, Figure 60 and Figure 61. The plots are shown with increasing number of cycles.

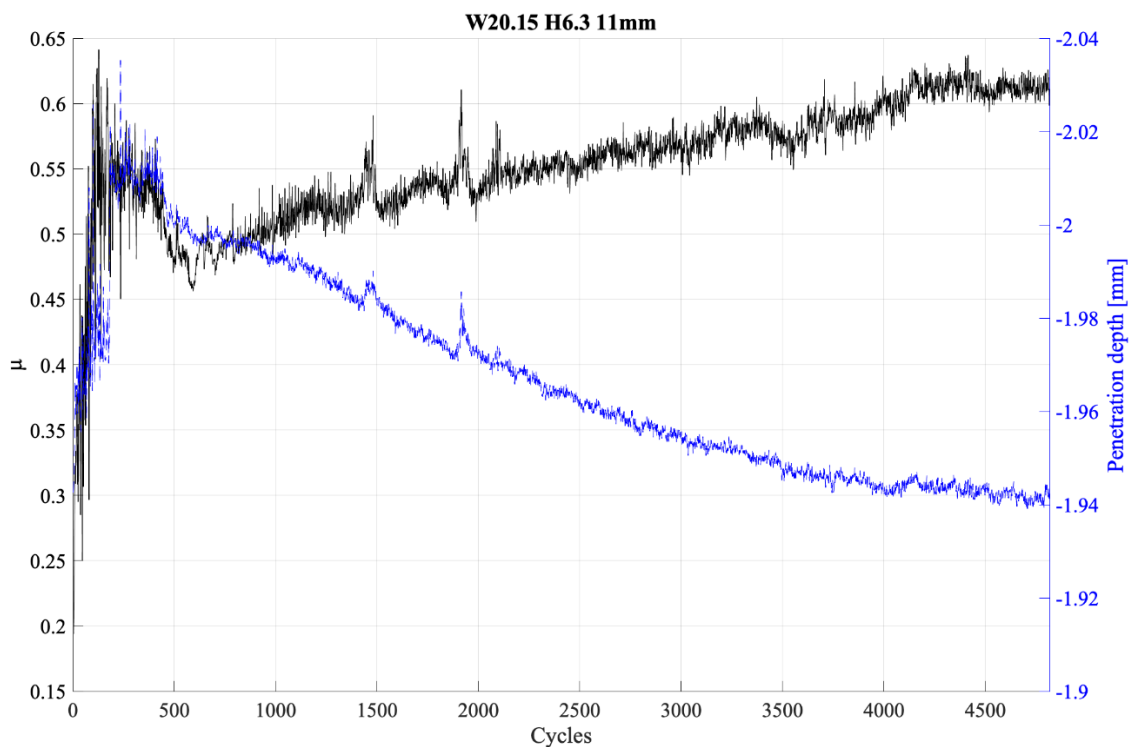


Figure 59. Coefficient of friction and penetration depth for W20.15 H6.3 11mm

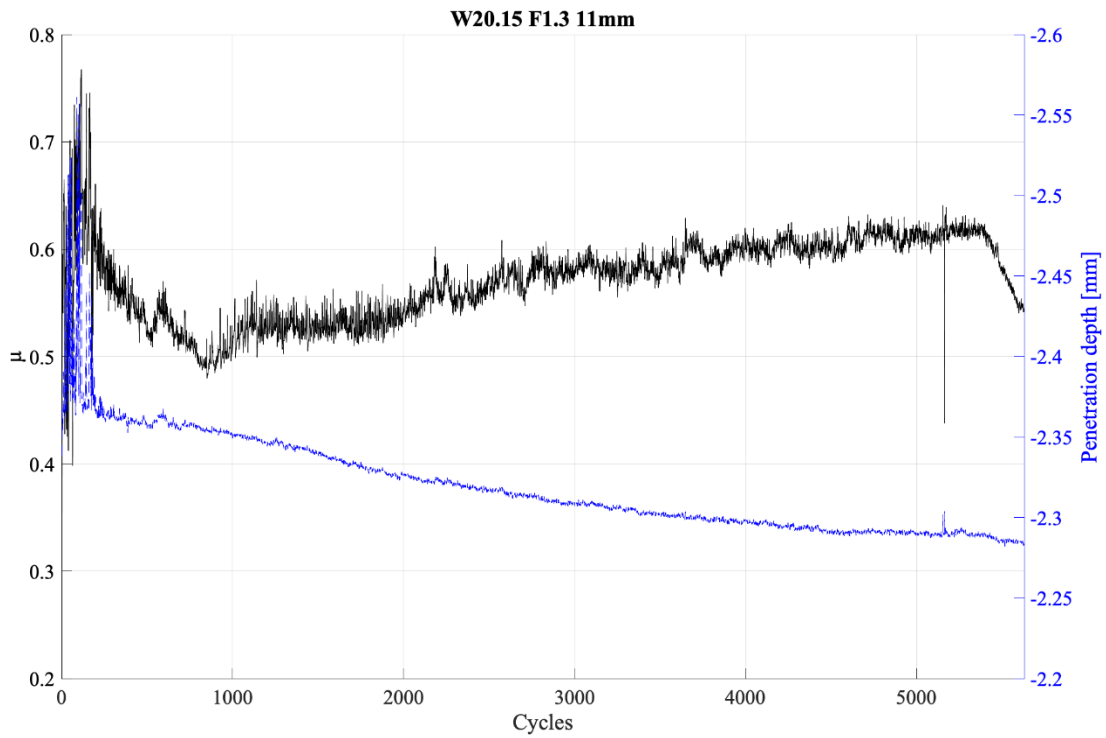


Figure 60. Coefficient of friction and penetration depth for W20.15 F1.3 11mm

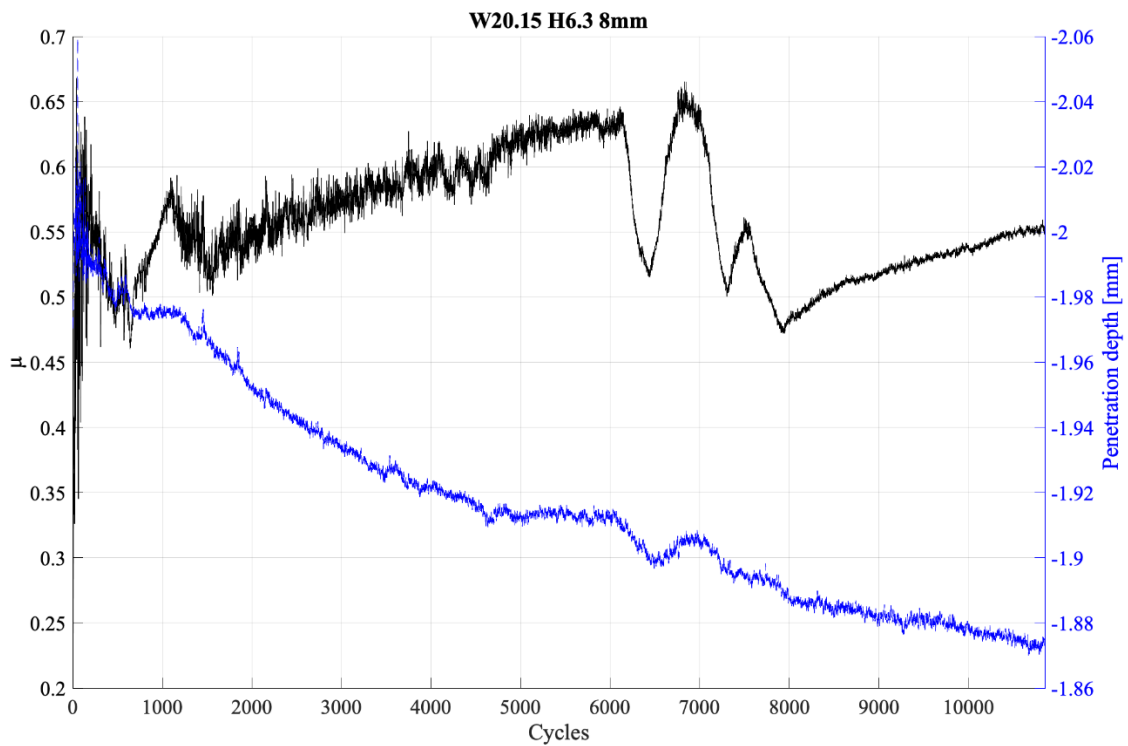


Figure 61. Coefficient of friction and penetration depth for W20.15 H6.3 8mm

Figure 59, Figure 60 and Figure 61 show, as observed for the uninterrupted tests (Figure 56 and Figure 57), the two heights exhibit an overall same evolution, but with differences depending on the height of the tested surface (either 1.3 or 6.3 mm from the substrate). Nevertheless, for any given height, the CoF variation is completely the same.

#### 4.3.2 Profilometer analysis

As stated in the Material and Methods section, after each tribometer test both the specimen and the balls were scanned by the profilometer. Here, the results will be exposed, determining the worn volume and showing visual results of the tracks.

##### 4.3.2.1 Worn tracks

The scans and the relative 3D images are presented hereafter for each tested surface.

### W20.18 H6.3

The test of 8mm in the W20.18 H6.3 surface was made as reference for interrupted tests made on the W20.15 F1.3 and H6.3 surfaces, as it has been stated before. The test at 11mm was the additional measurement made with a load of 20N.

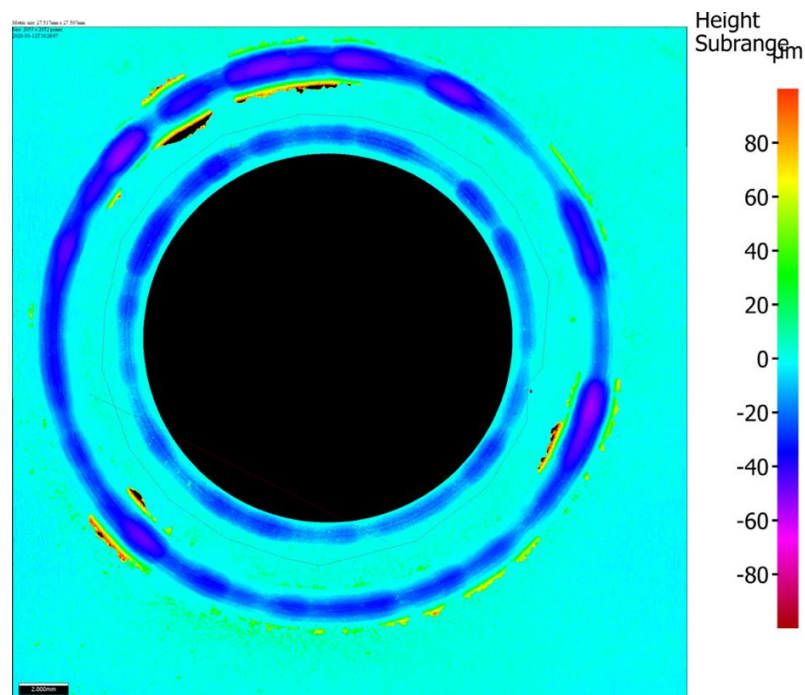


Figure 62. W20.18 H6.3 worn tracks (8 and 11mm) overview

**8mm (uninterrupted)**

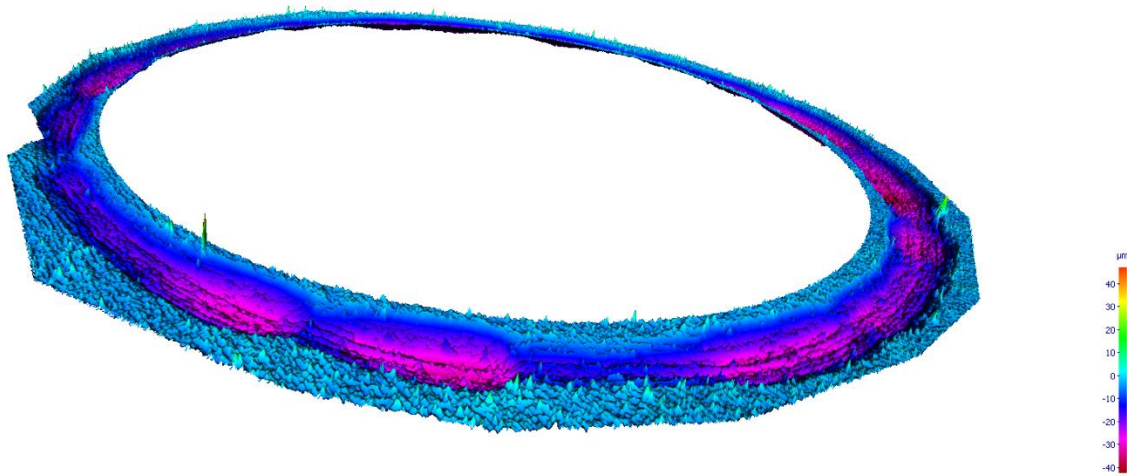


Figure 63. W20.18 H6.3 8mm worn track 3D overview

In Figure 63 a small portion of surface exhibited a defect, giving an optical reflection and it was removed from the worn volume measurement.

**11mm (uninterrupted, 20N load)**

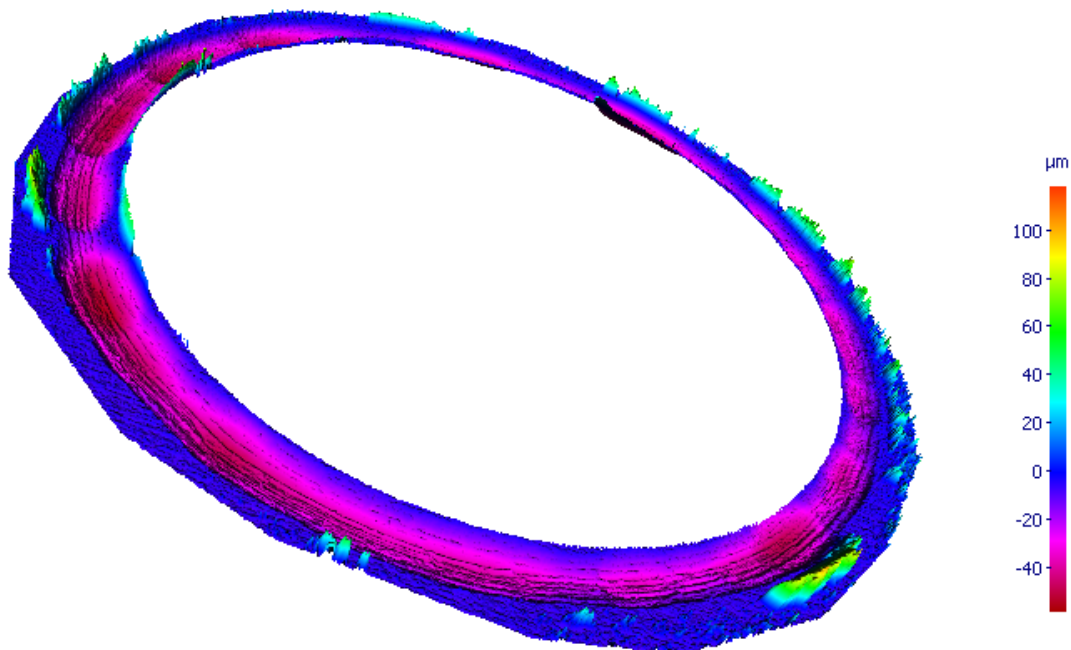


Figure 64. W20.18 H6.3 11mm worn track 3D overview

Huge amount of debris is accumulated on the track sides and the depth of the track is much deeper than any other test performed due to the higher load.

### W20.15 F1.3

This surface presents an uninterrupted test (8 mm) and the second interrupted test (5629 cycles).

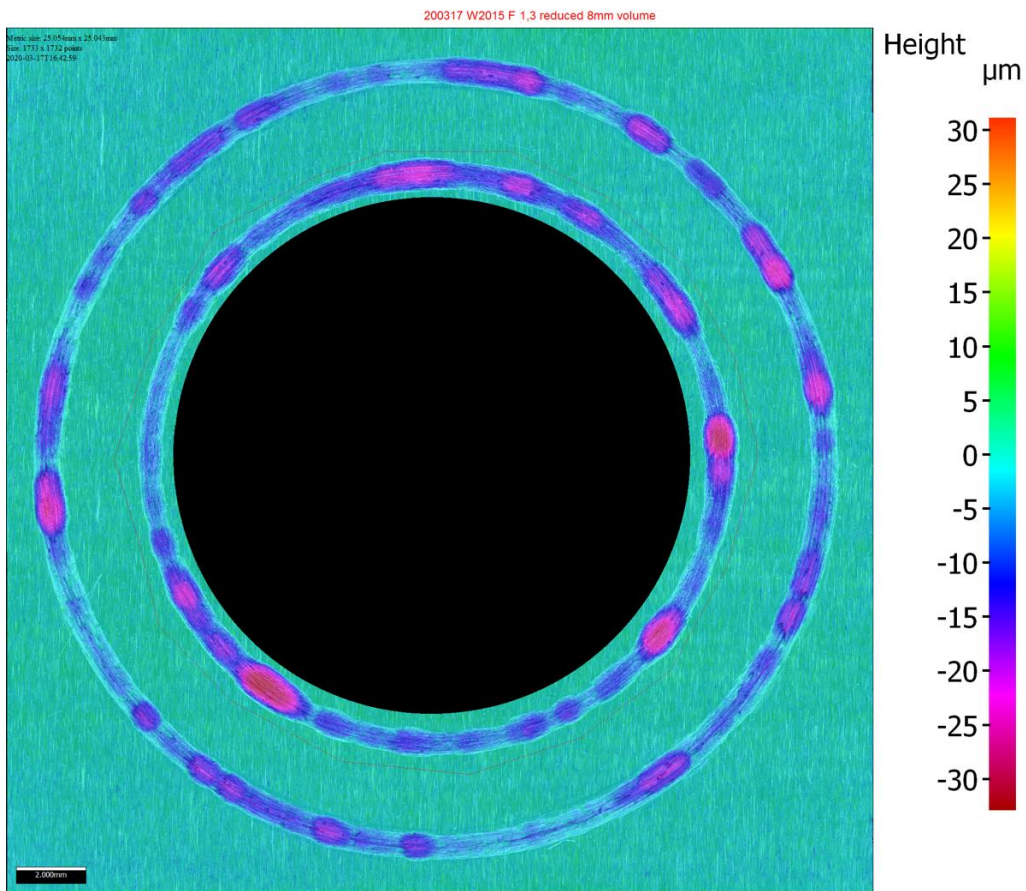


Figure 65. W20.15 F1.3 worn tracks (8 and 11mm) overview



**8mm (uninterrupted)**

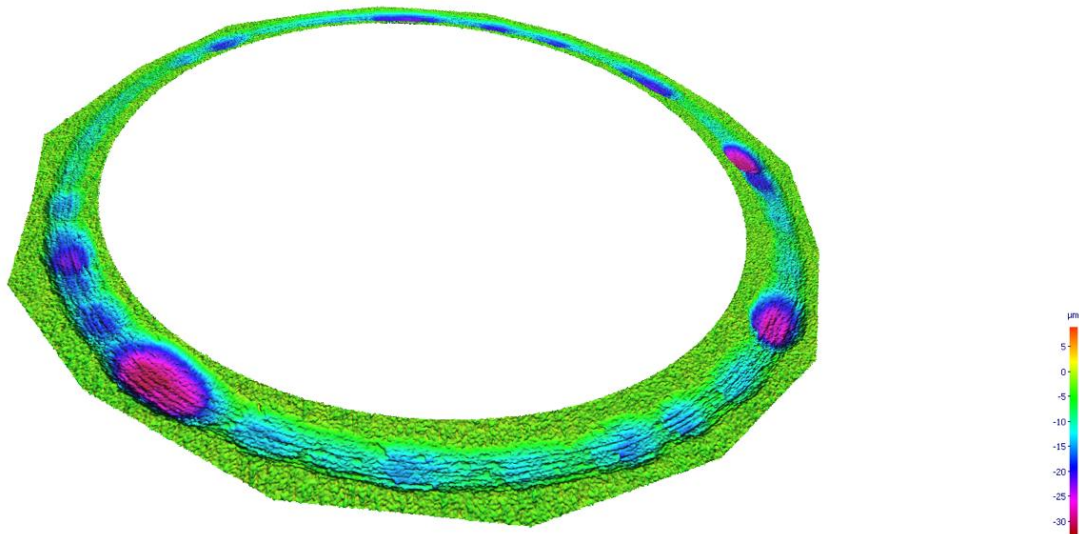


Figure 66. W20.15 F1.3 8mm worn track 3D overview

**11mm (interrupted at 5629 laps)**



Figure 67. W20.15 F1.3 11mm worn track 3D overview

### W20.15 H6.3

This surface was obtained from the deposit as the previous surface, but at 6.3 mm from the substrate. Both tracks are interrupted tests with the stop defined as mentioned in section 4.3. 11mm test exhibits a heterogeneous track, but it may be simply connected to the short number of laps. Instead, 8mm test exhibits a homogenous track width, but with localized deeper zones.

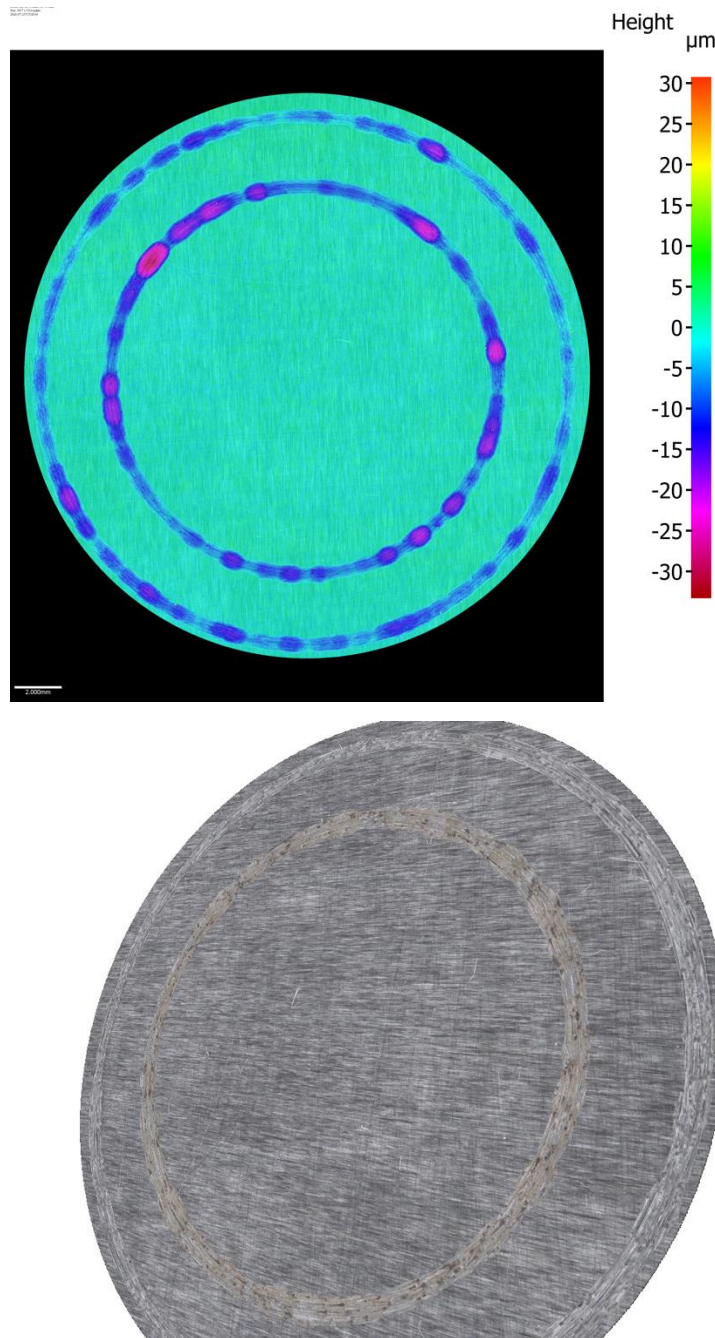


Figure 68. W20.15 H6.3 worn tracks (8 and 11mm) overview

As Figure 68 shows, the 8 mm and the 11 mm tracks exhibit different colors as obtained by the profilometer. Laps are different and it might be the reason of the difference in color. For the 8 mm one the duration of the test was longer than in the 11 mm one, which has a more similar color compared to the general surface color. The principal hypothesis for the color difference is that an oxidative wear becomes an important mechanism occurring at certain stages of the test. As it was stated on the wear mechanisms section, this oxidative wear appears.

**8mm (interrupted at 10855 laps)**

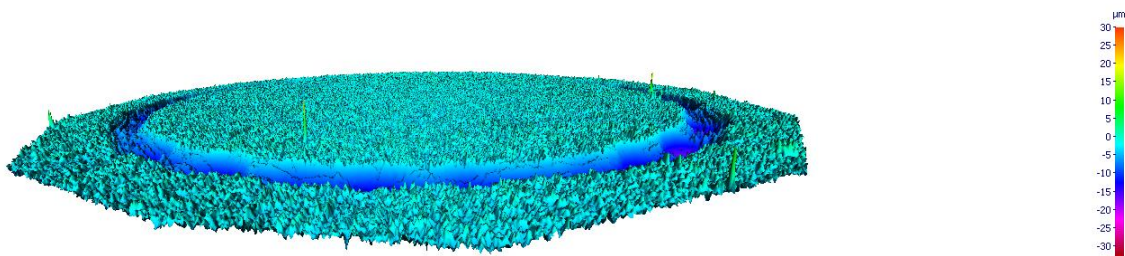


Figure 69. W20.15 H6.3 8mm worn track 3D overview

**11mm (interrupted at 4817 laps)**

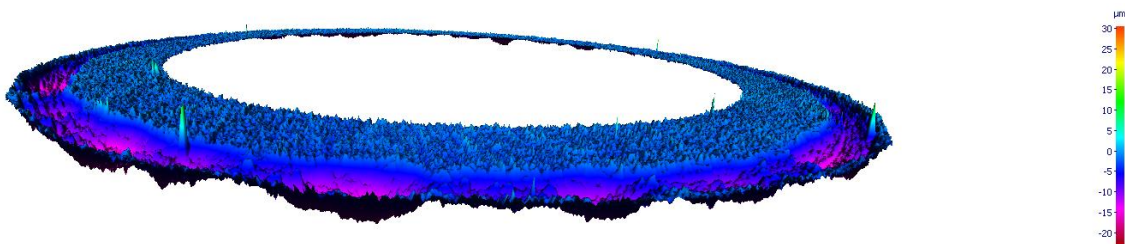


Figure 70. W20.15 H6.3 11mm worn track 3D overview

The results of the measured worn volume are resumed in Table 8 and plotted in Figure 71 as a function of the number of cycles.

Name of the test sample		Test duration [laps]	Worn volume [mm <sup>3</sup> ]
W20.18 H6.3	8 mm	22000	1.101
	11 mm	22000	1.946
W20.15 F1.3	8 mm	22000	0.499
	11 mm	5629	0.490
W20.15 H6.3	8 mm	10855	0.533
	11mm	4817	0.288

Table 8. Worn volume of tracks obtained by the profilometer. NOTE: W20.18 H6.3 11mm belongs to the 20N test

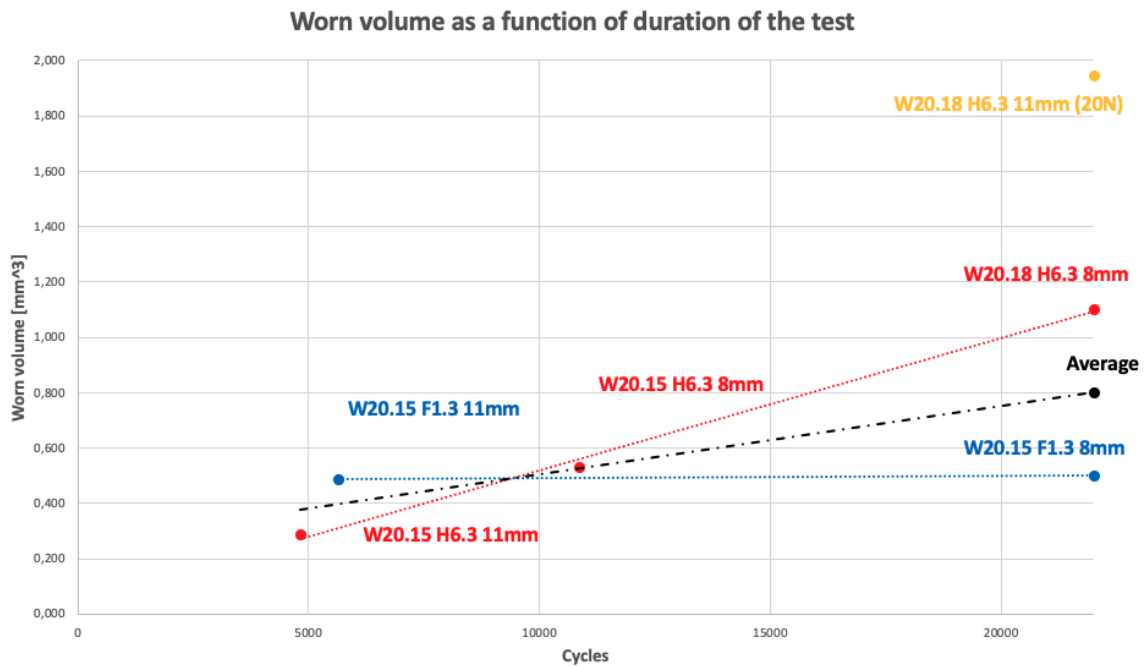


Figure 71. Worn volume of tracks as a function of duration of the test

The plot observable in Figure 71 shows how the worn volume by all means increases as the duration of the test is longer. For F faces tests, the worn volume almost stays flat, while it increases continuously for H faces tests. For both 22000 laps the average value is shown. However, the worn volume depends strictly on the used radius and the consequent different sliding distance. Therefore, in order to correctly compare all the measurements, the wear rates were calculated based on the different sliding distances.

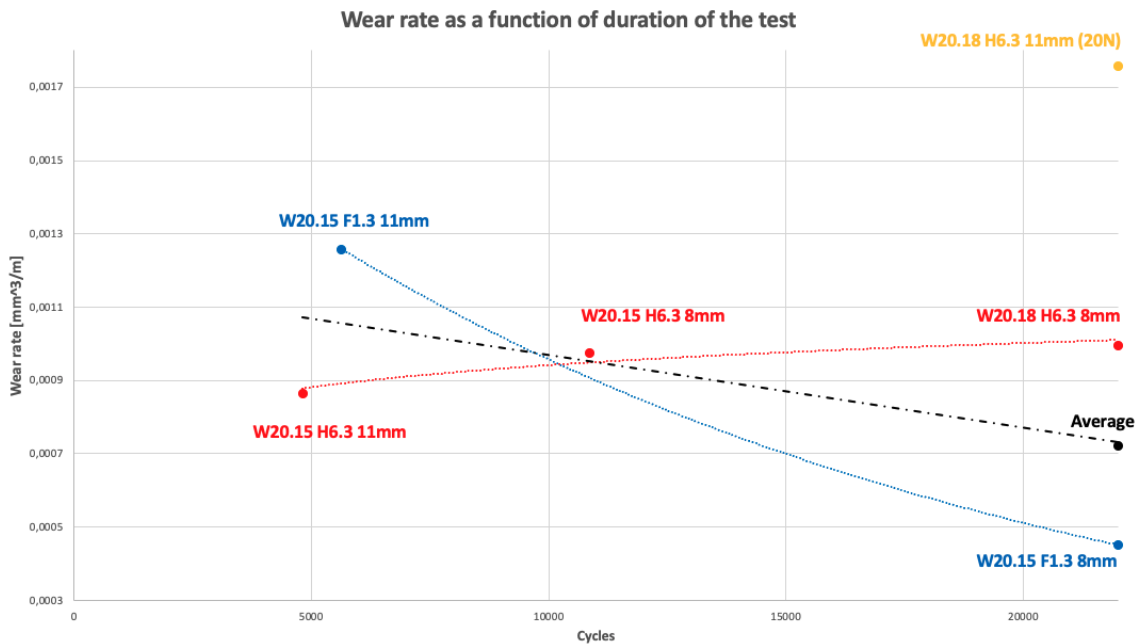


Figure 72. Wear rate of tracks as a function of the duration of the test

As mentioned before, F faces and H faces behave differently. Here this can be confirmed, as wear rate for H faces remains much more constant than for F face. These observations will be further discussed in section 5.

#### 4.3.2.2 Worn balls

The analysis of worn balls was also made by the profilometer. It was more difficult for the profilometer to obtain images as well as for the worn surfaces, due to the high reflectivity and to the spherical shape of the ball. For the calculation of the worn volume, as stated in Material and Methods section, the value needed is the height of the worn volume, observable in Figure 73.

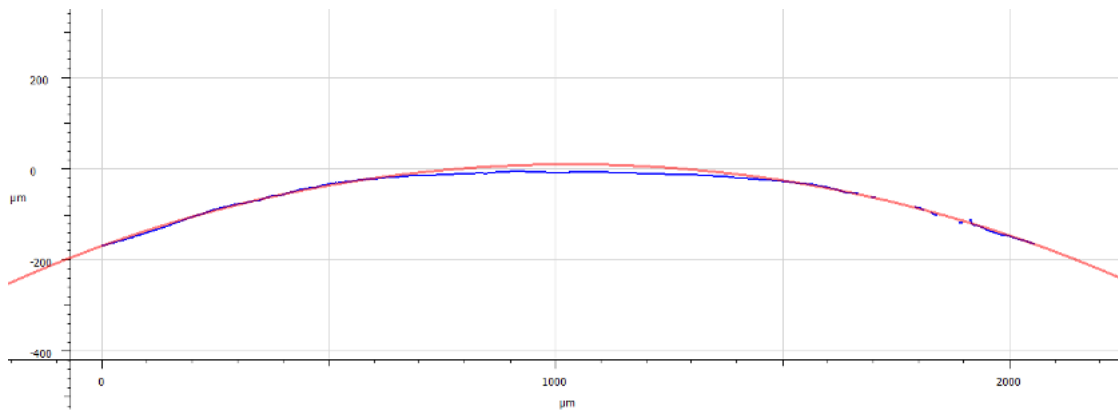


Figure 73. Calibration of the shape of worn balls

The height of the spherical cap is measured, where the red curve is an estimation of the initial shape of the ball and the blue curve is the profile data obtained by the images taken by the profilometer. Using the spherical cap volume equation that was shown before, worn volume of the balls is obtained. In order to have a good estimation, a very close value to 3 mm radius circumference (original radius of the ball) is required. Hence, in Table 9 are shown the results of every test balls' worn volume.

Name of the test sample		Test duration [laps]	Worn volume [mm <sup>3</sup> ]
<b>W20.18 H6.3</b>	<b>8 mm</b>	22000	$3.483 \cdot 10^{-3}$
	<b>11 mm</b>	22000	$10.032 \cdot 10^{-3}$
<b>W20.15 F1.3</b>	<b>8 mm</b>	22000	$3.788 \cdot 10^{-3}$
	<b>11 mm</b>	5629	$4.538 \cdot 10^{-3}$
<b>W20.15 H6.3</b>	<b>8 mm</b>	10855	$1.893 \cdot 10^{-3}$
	<b>11 mm</b>	4817	$1.2127 \cdot 10^{-3}$

Table 9. Worn volume of WC balls obtained by the profilometer. W20.18 H6.3 11mm belongs to the 20N test

As for worn tracks, the data given in Table 9 is visually better observed by the following plot:

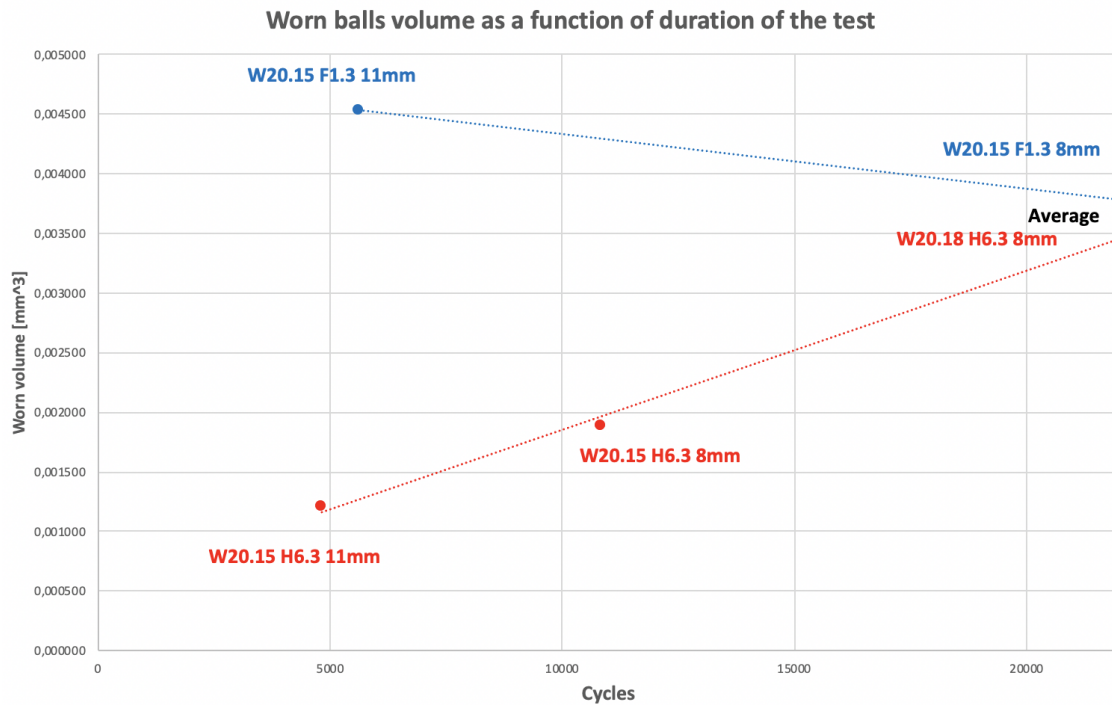


Figure 74. Worn balls volume as a function of the duration of the test

Worn volume of the balls increases with duration of the test for H faces, whereas it decreases for the F face. As for the previous plots, the average value for both 22000 laps test is given. More tests on F faces would be necessary to have a better comprehension of what is happening as only 2 points of data have been extracted.

#### 4.3.3 SEM images

The wear samples, after being analyzed by profilometer, were analyzed using the Scanning Electron Microscopy (SEM). Both BSE (Backscattered Electrons, information about the atomic size), and SE (Secondary Electrons, information about the roughness and morphology) modes were used. The usage of these two modes allows to have a better comprehension of an image taken as two perspectives are analyzed. This type of analysis is fundamental to know what is on surfaces since each wear test was stopped at different position of the CoF curve.

Although the tests were performed in different surfaces (**F**et and **H**ead), the images of the tests are ordered based on the length of the tests, from the shortest test to the

longest tests (22000 cycles), in order to follow the surface situation with the progress of the wear.

#### 4.3.3.1 W20.15 H6.3 11mm – Stopped at 4817 laps

This is the first and shortest interrupted test that was carried out (point 1 in Figure 56). Figure 75 shows a general overview of a part of the track. It shows narrow and shallow grooves, adding to the stacking of debris to the surface containing carbides.

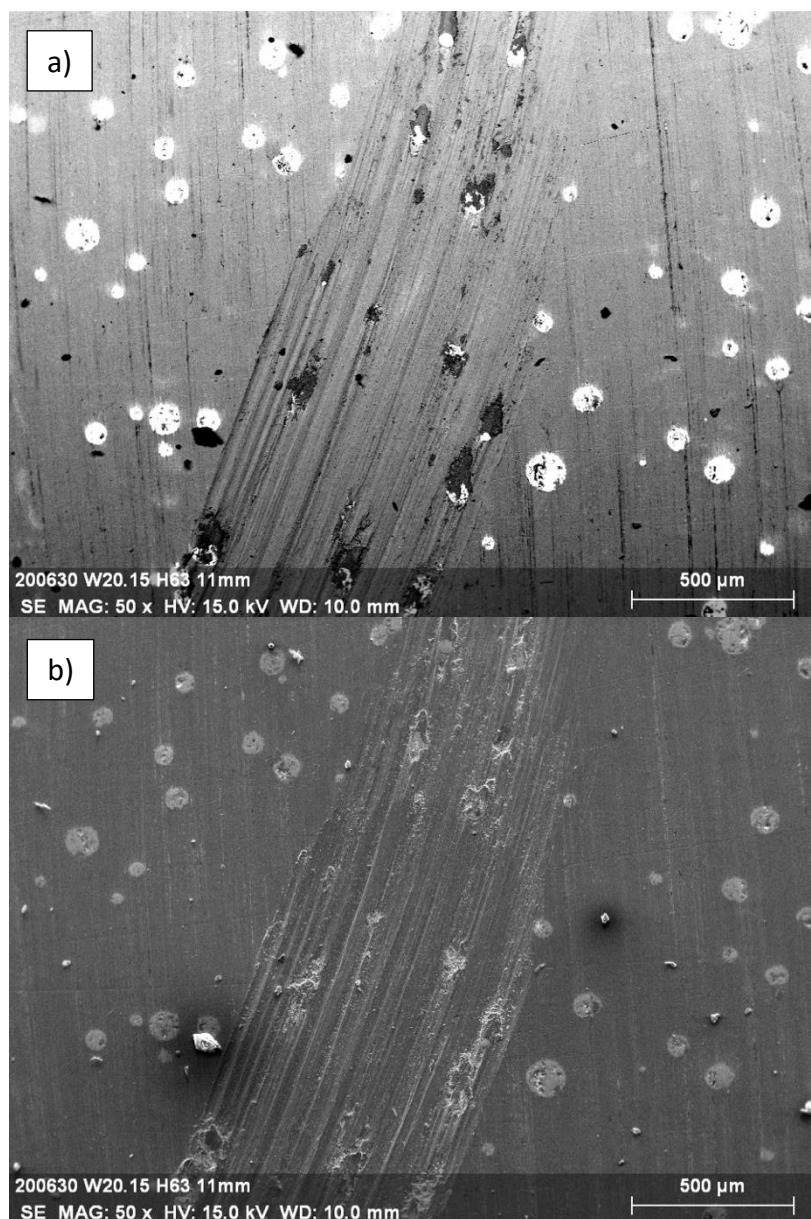


Figure 75. W20.15 H6.3 11mm (Int. at 4817 laps) worn track obtained by a) BSE and by b) SE.



In Figure 75b some bright spots can be observed. These particles are wax and they are caused by the not perfect cleaning of the surface after grinding and they are very difficult to remove. This serves as a note and possibly will be in further images on this analysis.

Figure 76 shows an observation of the called Mechanical Mixed Layer (MML) achieved on the surface. This protective layer is formed after a plastic deformation caused on the matrix during the test which is known to be more resistant to abrasion mechanisms and prevents the matrix from wearing [87].

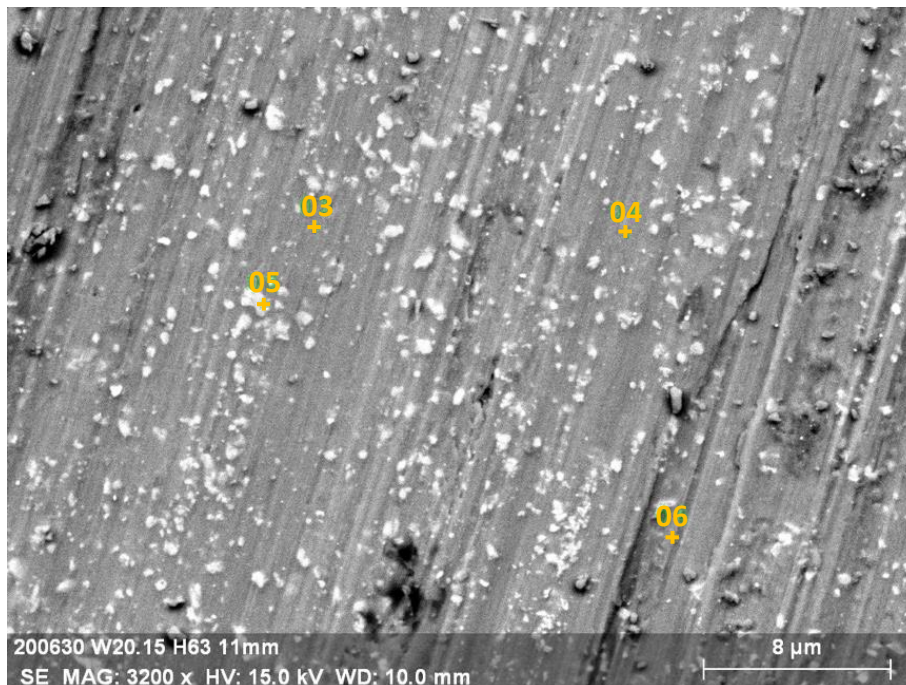


Figure 76. Mechanical Mixed Layer observation on W20.15 H6.3 11mm

Cross section observations could confirm the deformation according to the sliding direction and show its thickness. Figure 76 contains 4 points from which the composition was obtained, shown in Table 10.

wt %	C	O	Cr	Mn	Fe	Ni	Mo	W
Sp. 03	2.16	0.43	13.55	1.03	59.30	10.85	1.4	11.3
Sp. 04	2.55	1.75	13.3	1.02	60.94	12.09	1.32	7.04
Sp. 05	3.06	1.38	15.48	0.99	53.02	9.37	2.96	13.54
Sp. 06	2.33	0.73	13.97	1.11	57.89	11.3	2.20	10.46

Table 10. Chemical composition in wt% obtained from 4 points on Figure 66

The low oxygen content and a high tungsten content indicates that the layer is not oxidized and it is part of the MML since the solidification carbides are fractured and mixed with the matrix. The parts of carbides (high W content) act as a strain hardened. Eventually, this strain gradient can lead to delamination (Figure 75b and Figure 76).

Observing Figure 75 and Figure 77, some parts of the track have different width since the WC carbides particles protect the matrix and consequently the track width is shorter. Where the number of WC carbides is lower, the track width is larger. Furthermore, as observed in [1,2], material is stuck or mechanically locked in front of the WC carbides, according to the sliding direction.

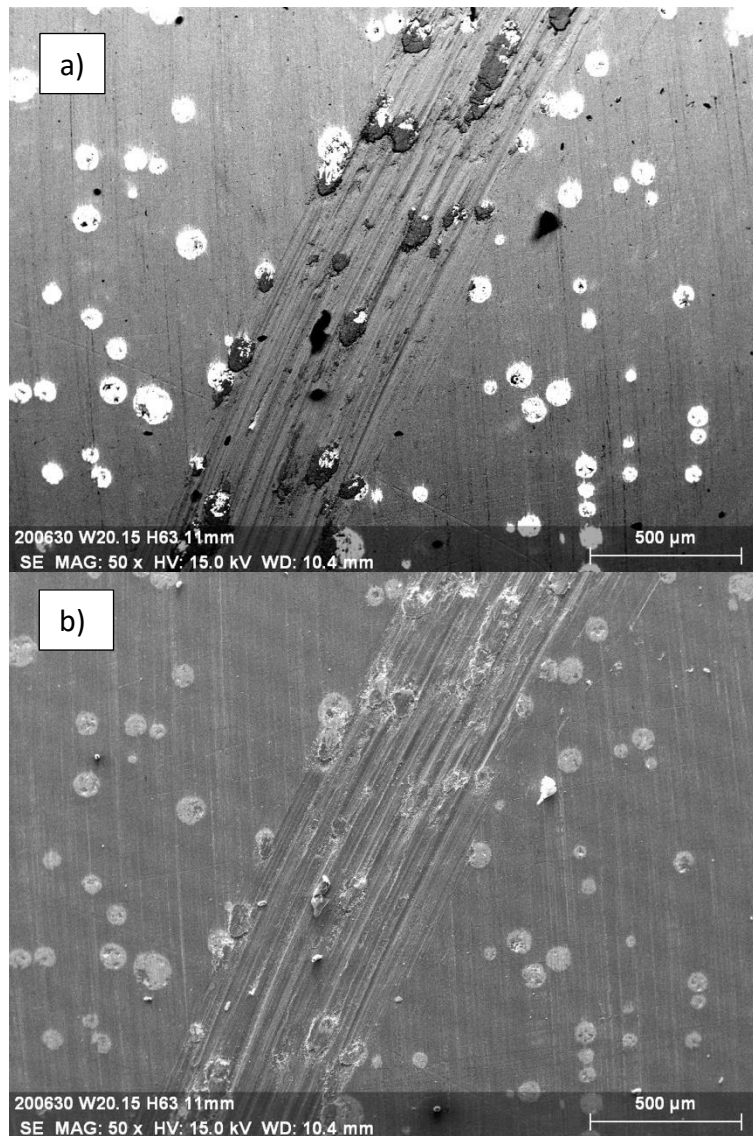


Figure 77. Different track width observed obtained by a) BSE and b) SE modes

Early signs of the tribolayer formation can be observed too, but this formation is only at its first stages, as it has not reached stabilization [88]. Table 11 shows how the darker area of Figure 78 is due to a enriched oxygen content, showing how early signs of the tribolayer protecting the matrix start to appear on the surface due to the continuous sliding. Plastic flowing can be observed as well in Figure 78.

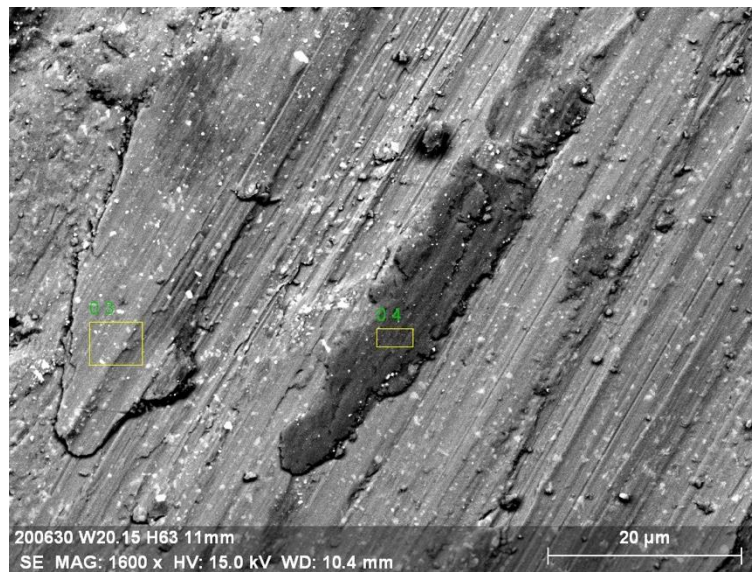


Figure 78. Early tribolayer signs on W20.15 H6.3 11mm. Spectra rectangles 03 and 04 for chemical composition

wt%	C	O	Cr	Mn	Fe	Ni	Mo	W
Sp. 03	2.17	2.81	14.11	1.20	57.73	11.72	1.50	8.75
Sp. 04	1.50	19.79	11.62	1.05	46.80	8.94	1.61	8.69

Table 11. Chemical composition in wt% of 03 and 04 rectangles from Figure 68

#### 4.3.3.2 W20.15 F1.3 11mm – Stopped at 5629 laps

This second interrupted test was just stopped after the first drop of the CoF and it was carried out on face F at 1.3 mm from the substrate. This track shows some differences with the first interrupted test. However, as shown in Figure 79, the adhesion which causes material to be stacked in front of the solidification carbides is also observed. Furthermore, low carbide density areas are also observed to be cleaner of grooves but they are worn more as they are less reinforced.

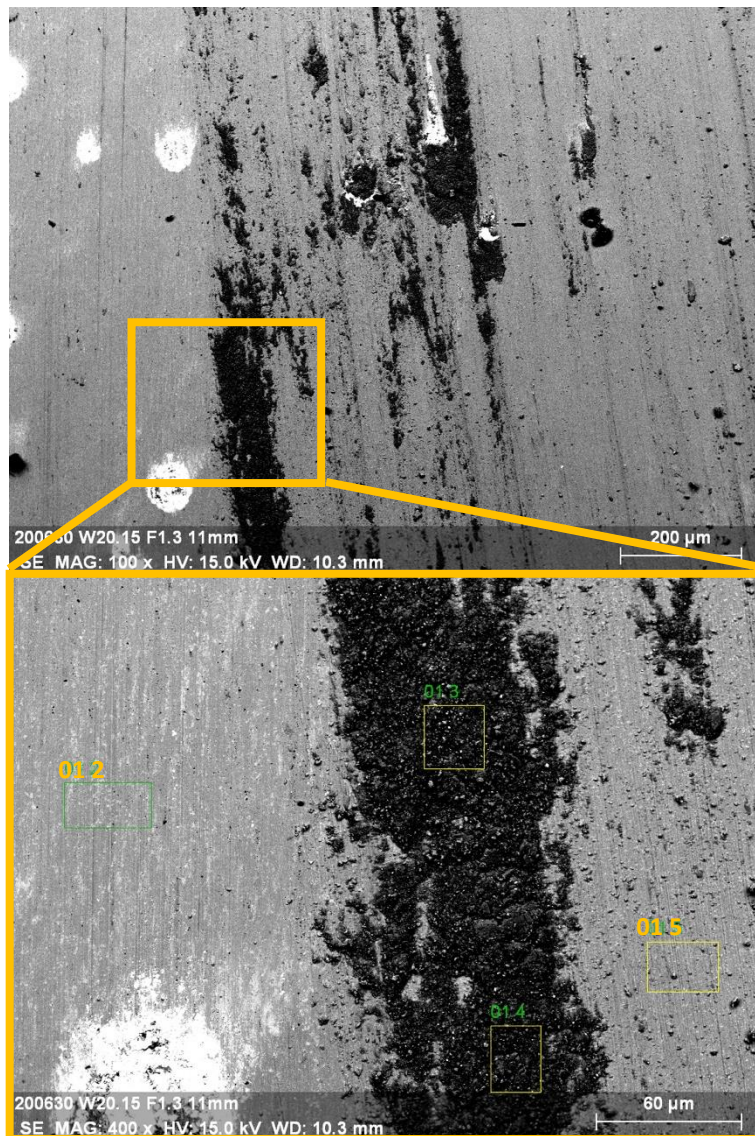


Figure 79. Magnification on a debris zone on one side of the track of W20.15 F1.3 11mm

Regarding to these differences mentioned before, this track shows a higher quantity of debris which is very fine and generally dark (Figure 79). Moreover, Table 12 gives the composition of the rectangles.

wt%	C	O	Cr	Mn	Fe	Ni	Mo	W
Sp. 01 2	2.70	0.46	14.97	1.43	61.73	11.43	2.27	5.02
Sp. 01 3	2.73	32.52	9.77	0.82	38.88	6.29	1.11	7.88
Sp. 01 4	2.98	33.97	10.12	0.66	37.76	6.02	1.38	7.11
Sp. 01 5	2.13	2.18	16.52	1.01	59.63	9.66	1.97	6.90

Table 12. Chemical composition in wt% of 01 2, 01 3, 01 4 and 01 5 rectangles in Figure 79

The darker debris is oxygen-rich debris, while other parts of the matrix exhibit normal values. This type of fine debris is formed in this stage, as this amount of debris was not observed in the previous interrupted test.

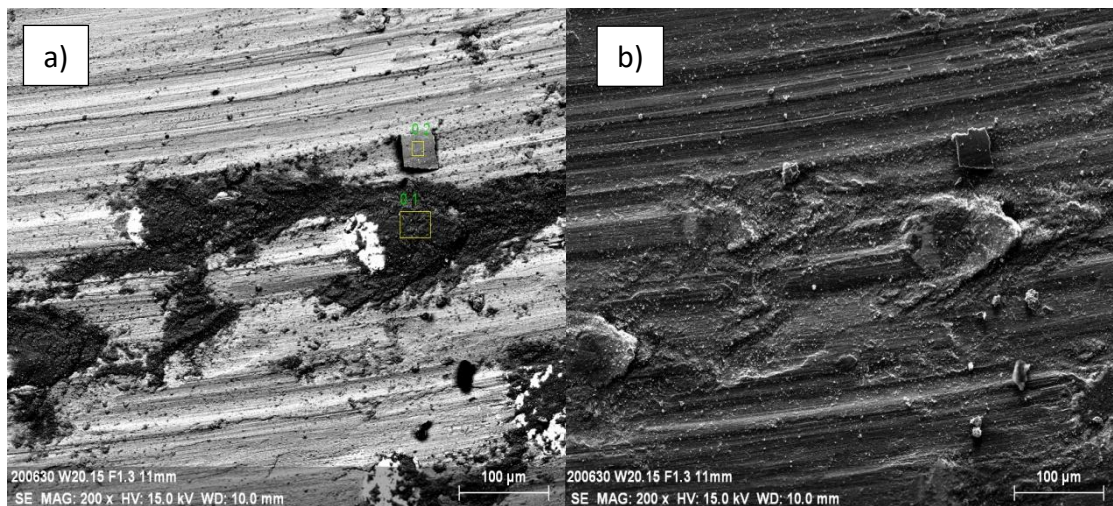


Figure 80. Magnification on different type of oxidized debris on W20.15 F1.3 11mm by a) BSE and b) SE modes

A higher magnification on the material stacked on the front of the WC carbides has also been made. Two different type of debris can be observed on Figure 80a. The chemical composition is given in Table 13 of two different colored debris.

wt%	C	O	Cr	Mn	Fe	Ni	Mo	W
Sp. 01	2.19	31.86	10.81	0.83	39.55	6.28	0.41	7.19
Sp. 02	2.38	18.90	12.06	1.01	44.67	7.30	1.48	12.21

Table 13. Chemical composition in wt% of O1 and O2 rectangles on Figure 80

As stated in [1,2], WC carbides mechanically lock the ball and some material is removed from the counterpart. Indeed, darker debris corresponds to a much more oxidized debris, with less W content. These dark debris in front of the WC carbides are pieces of the WC ball, mixed with debris from the matrix. Grey colored debris are more enriched with tungsten and correspond directly to a piece of WC ball, also due to its regular morphology.

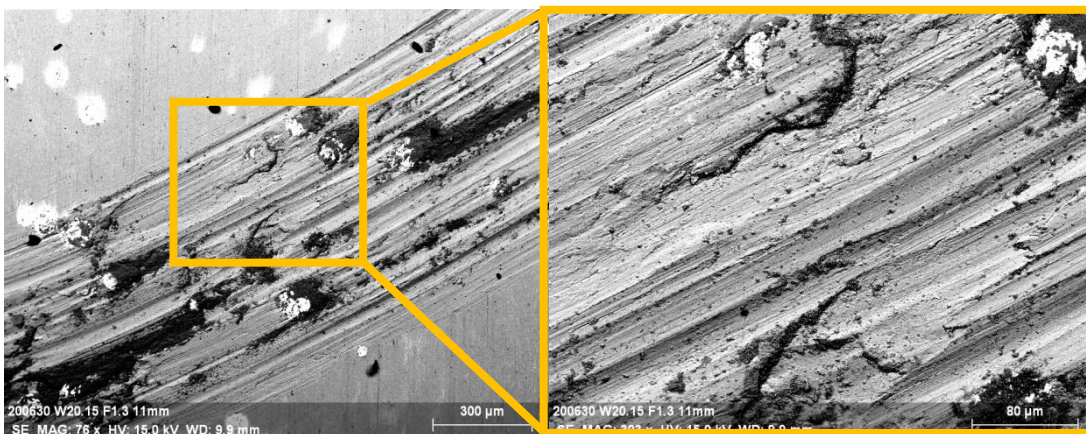


Figure 81. Plastic deformation and delamination on W20.15 F1.3 11mm

Plastic deformation or plastic flowing is also observed on the surface (Figure 81).

#### 4.3.3.3 W20.15 H6.3 8mm – Stopped at 10855 laps

This third interrupted test was stopped when the second increase of CoF occurs (Figure 56). The common characteristics from the previous interrupted tests remain the same: material stacked in front of the solidification carbides and higher wear on low carbide density areas (and vice versa). Grooves are also more visible on high carbide density areas, and now these grooves are larger and wider.

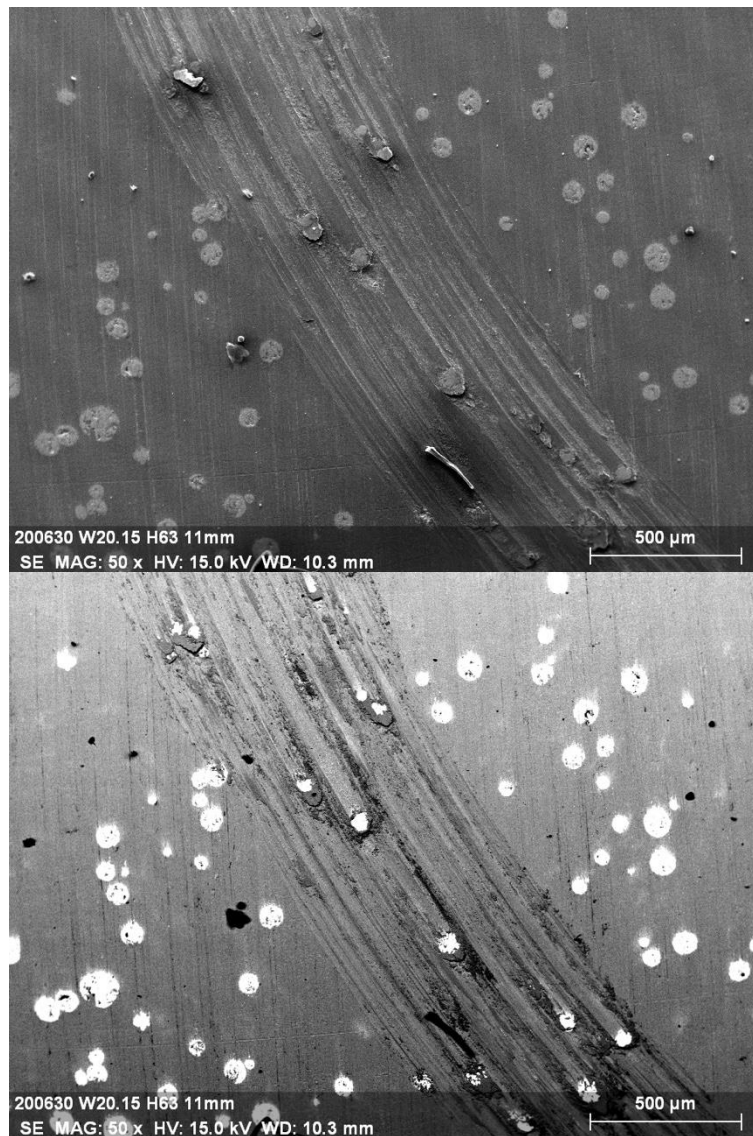
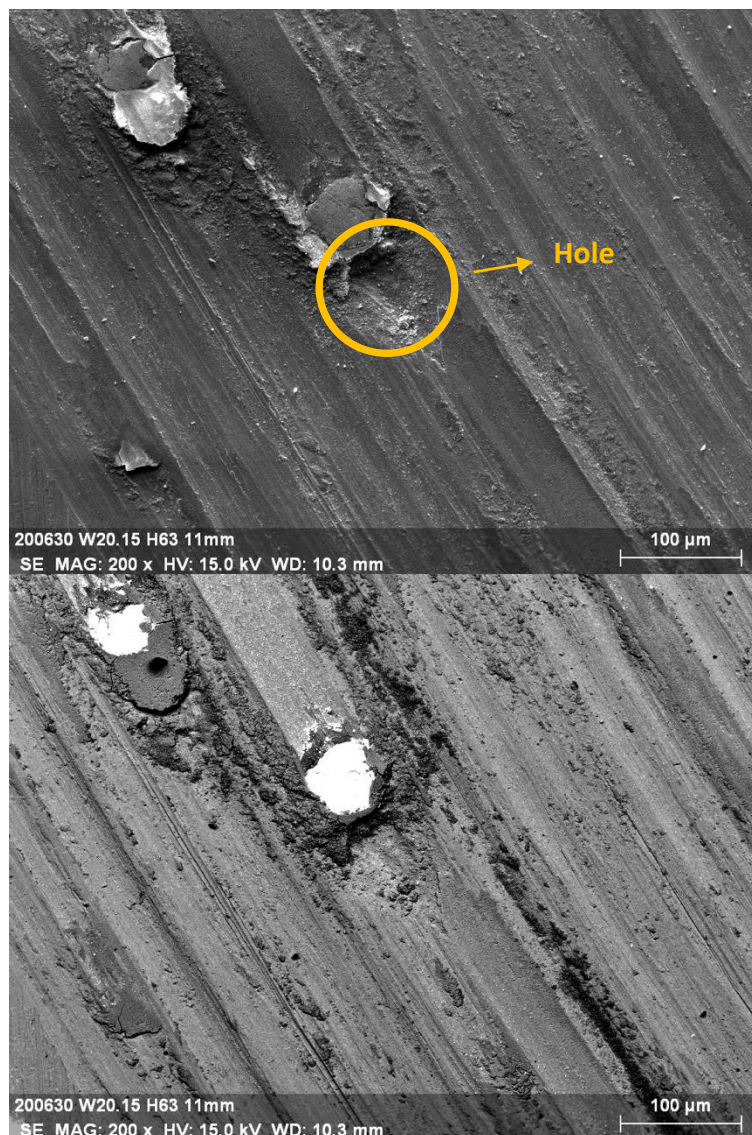


Figure 82. General overview of the W20.15 H6.3 8mm track

A higher magnification on this area is observed on Figure 83.





*Figure 83. Magnification of a hole in front of the solidification carbides*

Holes are observed in front of the WC carbides. These holes are generated by the presence of debris in front of the carbides since the stacked material (debris from the matrix and pieces of WC ball) blocks them. These debris locally abrade the matrix with the progress of the test and their quantity increase. If large quantities of debris are formed some debris can move along the sides of the carbides. This holes could also be observed in the work done by D. Mario in his Master thesis [1].

Figure 84 shows a layer of compacted debris, homogeneously distributed on the surface. This debris form then a tribolayer on the W20.15 H6.3 8mm surface.

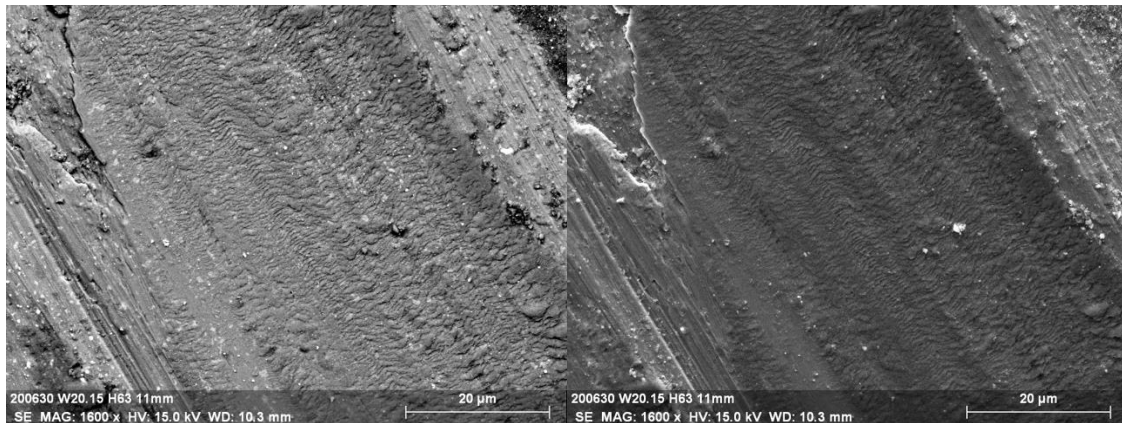


Figure 84. Compact tribolayer observation on W20.15 H6.3 8mm

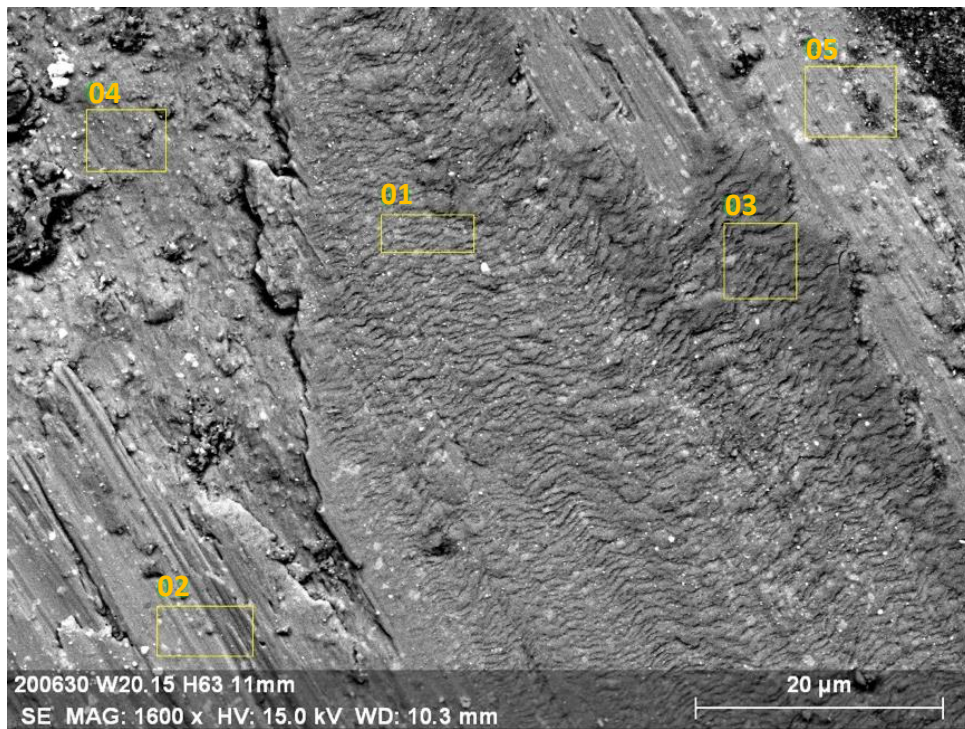


Figure 85. Spectra points in the tribolayer observation on W20.15 H6.3 8mm

wt%	C	O	Cr	Mn	Fe	Ni	Mo	W
Sp. 01	2.13	9.69	12.07	0.96	50.44	11.31	1.83	11.58
Sp. 02	2.21	1.05	14.43	1.02	60.17	11.77	1.80	7.56
Sp. 03	2.24	20.82	10.63	0.59	38.95	5.99	1.13	20.65
Sp. 04	1.87	4.33	13.92	1.07	58.97	11.70	1.60	6.54
Sp. 05	2.98	4.86	15.13	0.78	51.98	8.22	1.83	14.22

Table 14. Chemical composition in wt% of 01, 02, 03, 04 and 05 rectangles in Figure 75

The layer is composed in different type of oxides with some parts richer in tungsten oxides (Sp. 03) and less rich ones (Sp. 01).

As shown in Figure 86, the tribolayer is observed with different contrasts and more or less compacted. Both features are due to the mix of oxides forming locally the tribolayer (Table 15).



Figure 86. Composition zones of different parts of the mix of debris and tribolayer present on W20.15 H6.3 8mm

wt%	C	O	Cr	Mn	Fe	Ni	Mo	W
Sp. 01	2.96	31.67	8.42	0.8	37.10	7.94	1.04	10.08
Sp. 02	2.27	30.63	5.92	0.52	24.48	4.78	0.58	30.82
Sp. 03	2.33	34.05	7.11	0.70	27.06	4.81	0.50	23.45
Sp. 05	2.60	34.83	6.34	0.99	30.38	6.69	0.16	18.01

Table 15. Chemical composition in wt% of zones 01, 02, 03 and 05 selected on Figure 76

All zones studied have almost the same oxygen amount, with changes depending on the matrix or the WC carbides contribution to tribolayer. This layer is a mix of the debris of the combination of both matrix and WC carbides as a consequence, and in this stage the fine debris studied on the second interrupted test (W20.15 F1.3 11mm) is being compacted.

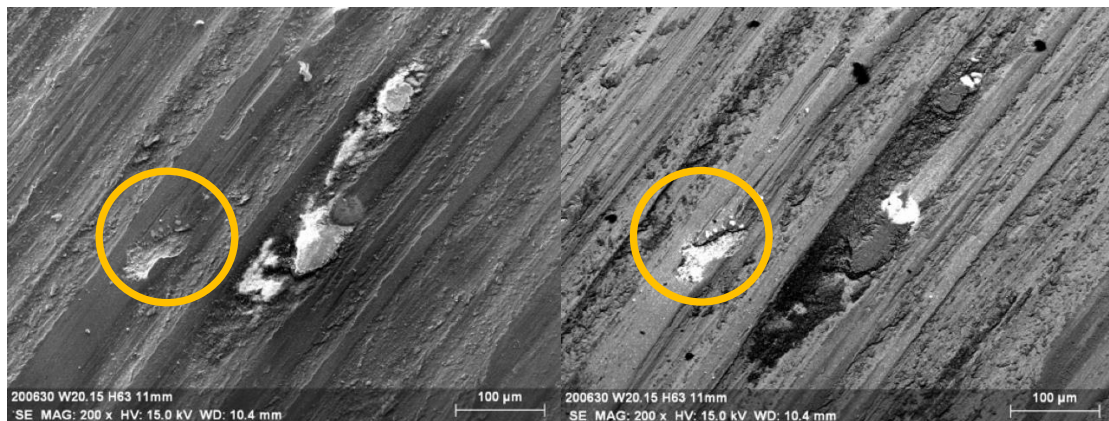


Figure 87. Cracked carbide observation

Moreover, as the length of this test is longer, some carbides start to crack due to the continuous sliding of the ball. As shown in Figure 87, along with the previously mentioned plastic deformation (causing then delamination), abrasion's effects here are easier to observe as the amount of material worn is higher. Observations show that three-body abrasion (due to higher amount of debris spreading through the track) has started here and becomes the most important abrasive mechanism.

#### 4.3.3.4 W20.18 H6.3 8mm – Uninterrupted test

This is the first uninterrupted test that was carried out (Figure 56, Figure 63). As it has already been stated, this test was set to be the reference for the interrupted tests. The test taken out on this surface on 11mm was the one made with a load of 20 N (Figure 56). Consequently, all the surface was completely full of debris coming from this last test. In order to observe the track free from these debris, a strong cleaning with alcohol and compressed air was applied.

Regarding the observations made on this surface, it shows a mix of all mechanisms seen on the interrupted tests i.e. material stacked to the front part of the solidification carbides, deeper and larger grooves (as the test lasted more), some broken carbides, the before mentioned holes before the solidification carbides, a more compaction of the oxides generating the tribolayer and delamination caused by the plastic deformation.

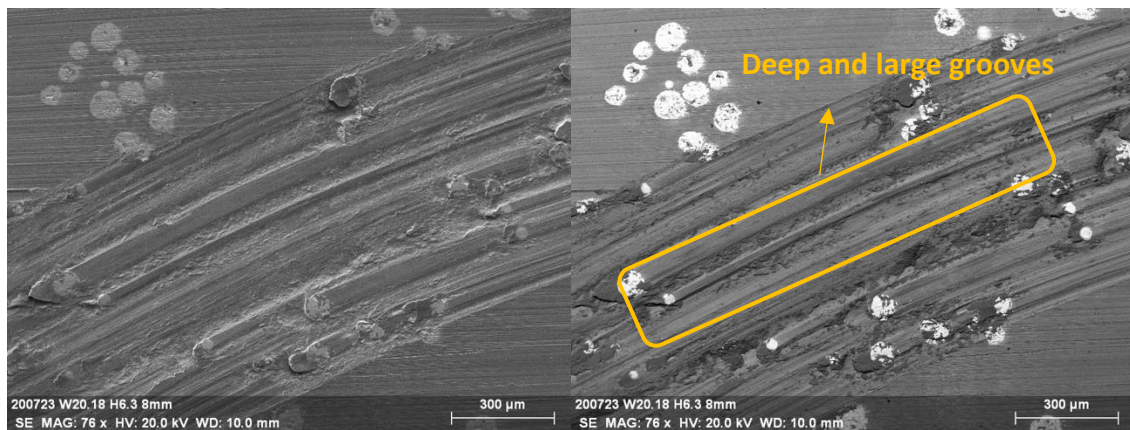


Figure 88. Track overview on W20.18 H6.3 8mm

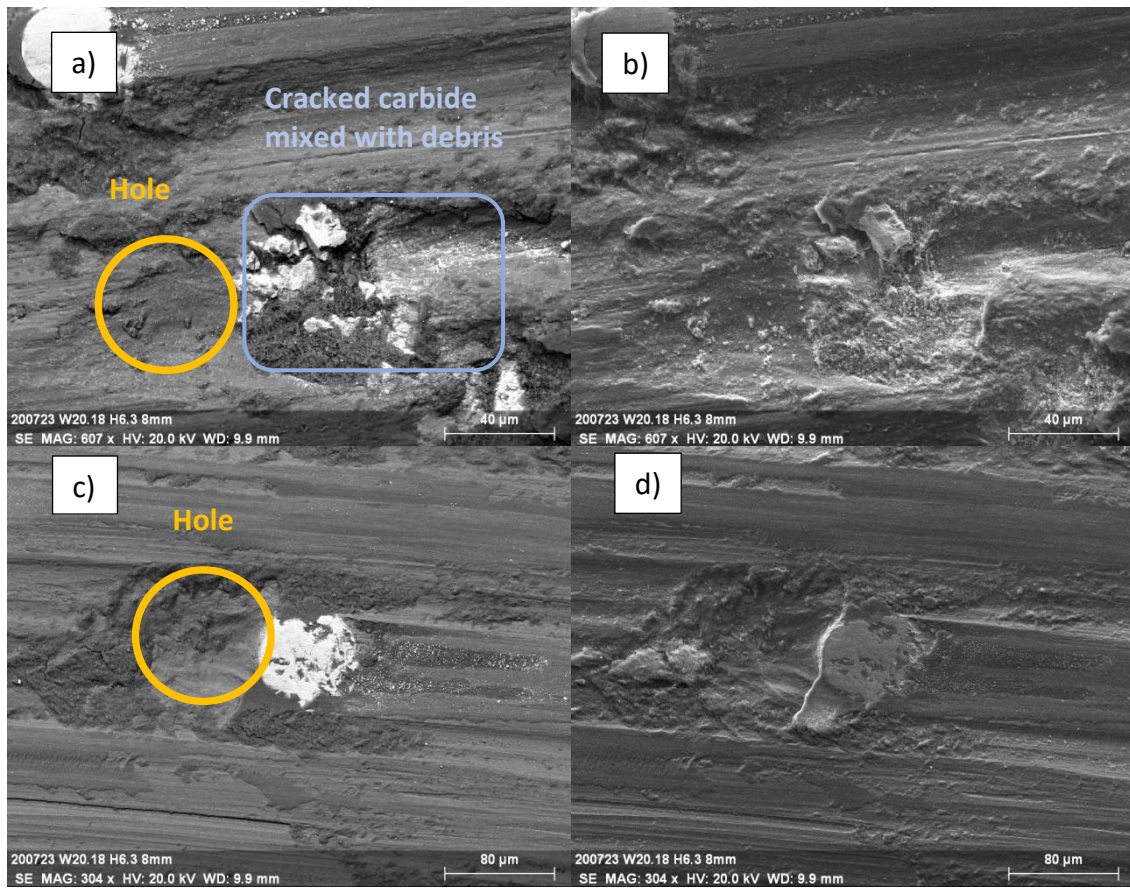


Figure 89. Two carbides magnification. a) BSE and b) SE modes of a cracked carbide with a hole in front. c) BSE and d) SE modes of a carbide with a hole in front



Figure 90. Track width change overview along with a tribolayer overview

Regarding the tribolayer, an interesting spot could be analyzed by the SEM. The strong cleaning modified the surface after test, this treatment cracked some parts of the tribolayer exhibiting that some zone of the it were particularly compacted.

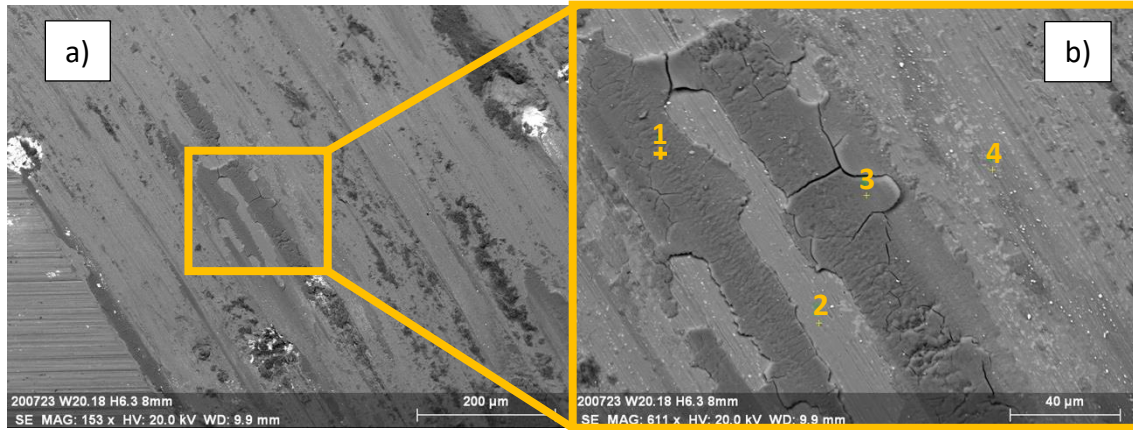


Figure 91. Cracked tribolayer observation with b) 4 points selected for composition

4 points were selected for a chemical composition study on Figure 91b and the data was recovered in Table 16.

wt%	C	O	Cr	Mn	Fe	Ni	Mo	W
Sp. 1	1.92	29.96	8.71	0.60	31.76	5.87	0.88	20.31
Sp. 2	1.71	1.10	14.77	1.08	60.05	10.93	1.84	8.51
Sp. 3	1.77	22.30	10.37	0.79	39.58	7.19	1.09	17.02
Sp. 4	1.99	12.17	12.13	0.94	49.58	9.06	1.20	12.93

Table 16. Chemical composition in wt% of points 1, 2, 3 and 4 from Figure 91b

Point 2 is a part of the matrix that was protected by the tribolayer which was removed from the surface by the cleaning. Its composition shows this area is not oxidized and less worn than the surroundings (Point 4). It can also be observed that the compacted tribolayer exhibits a high and homogeneous W content (Points 1 and 3).

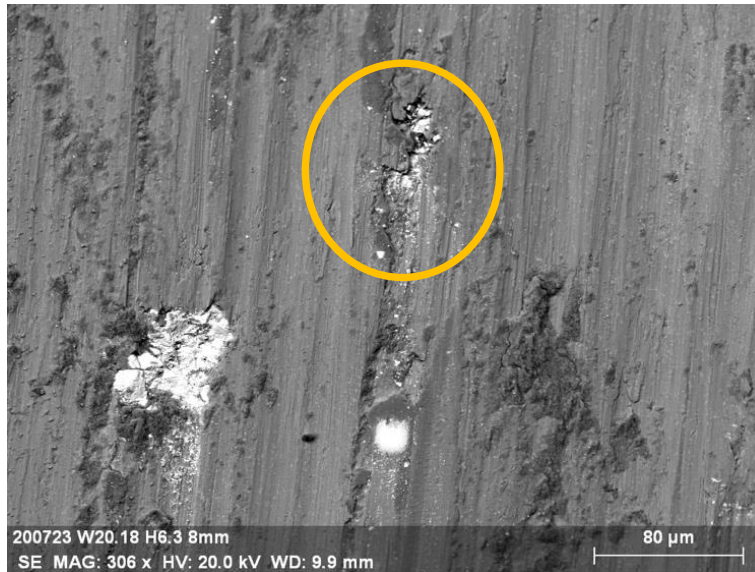


Figure 92. Delamination sign on W20.18 H6.3 8mm

As in the previous uninterrupted tests, delamination caused by plastic deformations is observed as well. This delamination could have occurred in previous stages though.

#### 4.3.3.5 W20.15 F1.3 8mm – Uninterrupted test

This is the second uninterrupted test at 1.3mm from the substrate (Figure 57, Figure 66). In spite of CoF differences between 10N uninterrupted tests on the tribometer results, SEM observations show, generally, the same wear features on this surface and the previous one. Adhesion (stacking of material in front of solidification carbides), abrasion (grooves caused by two- and three-body mechanism) and plastic deformation signs are observed.

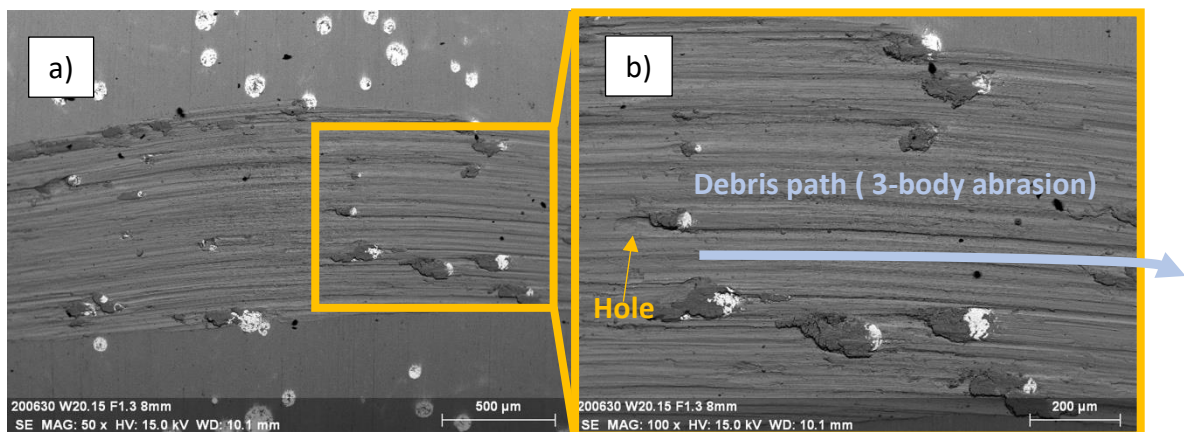


Figure 93. a) Track overview. b) Magnification on a carbide showing the path of the three-body abrasion



Following the results on all the previous surfaces, low carbide density areas are more worn due to the lesser amount of reinforcement, although grooves are less visible as the material is pulled from the surface at the same time. Thus, some parts of the track are narrower than others, as it has been observed in all the surfaces. However, there is no observation of WC carbide pull-out, similar to the interrupted test in this surface for the 11mm radius. Holes in front of the solidification carbide particles are observed too, and a composition map is shown in Figure 94.

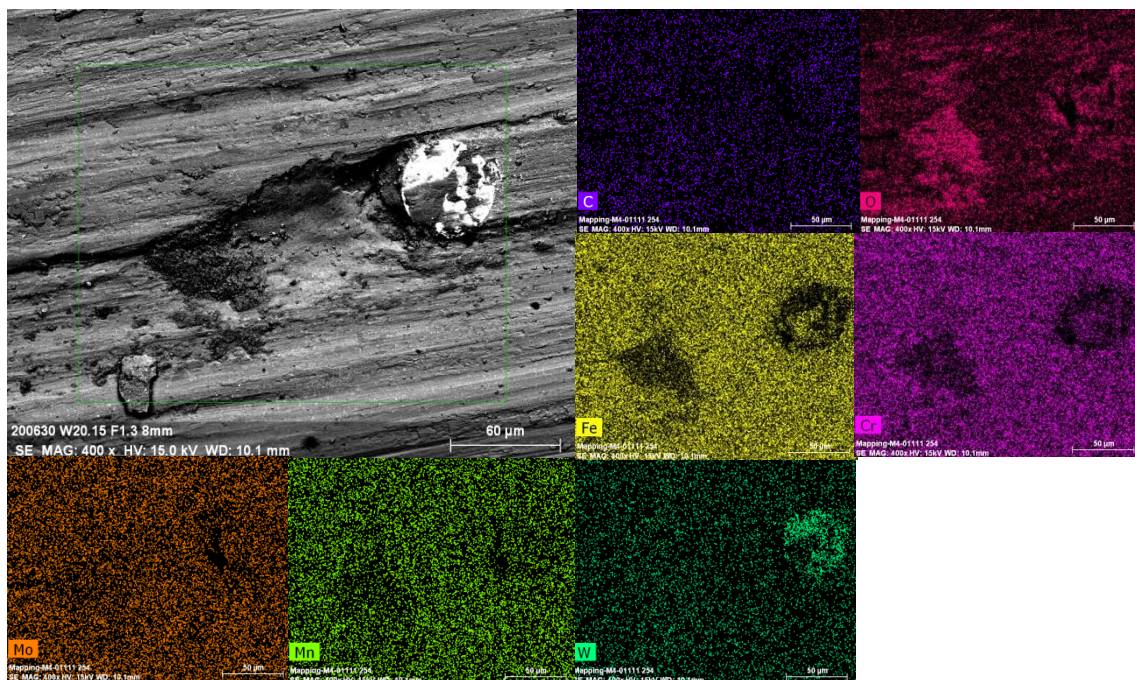


Figure 94. Composition map of a hole in front of a solidification carbide

Oxidized material is mainly in the material stacked and in the hole in front of the WC carbides. In addition, alloying elements are equally spread through the matrix, except for the chromium which is neither on the debris nor near the solidification carbide particle.

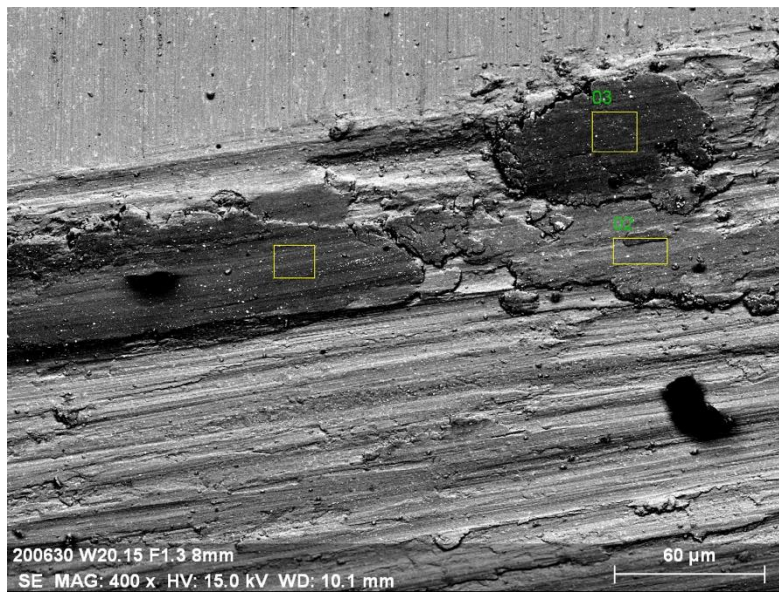


Figure 95. Tribolayer zones for chemical composition analysis

wt%	C	O	Cr	Mn	Fe	Ni	Mo	W
Sp.	1.58	19.90	13.89	0.89	41.53	6.59	1.42	14.21
Sp. 02	1.71	12.11	13.67	0.94	50.93	9.62	1.83	9.20
Sp. 03	1.68	16.91	10.89	0.97	48.95	9.93	1.58	9.10

Table 17. Chemical composition in wt% for zones selected on Figure 85

Results from the composition of the zones selected on the tribolayer are in good agreement with the tribolayer results obtained in other tracks: some compacted debris are enriched in tungsten.

#### 4.3.3.6 W20.18 H6.3 11mm – Uninterrupted test – 20N

This test was the additional and exploratory test of this study. Here, all the wear mechanisms that had been observed in 10N tests are observed as well, but the higher load enhanced their effects. Indeed, the realization of this test caused the 8mm test to be full of debris coming from the high load test and therefore the previously mentioned cleaning considerations had to be made. The images shown below are the ones obtained as the post-mortem state, so the cleaning was made after these images were obtained.

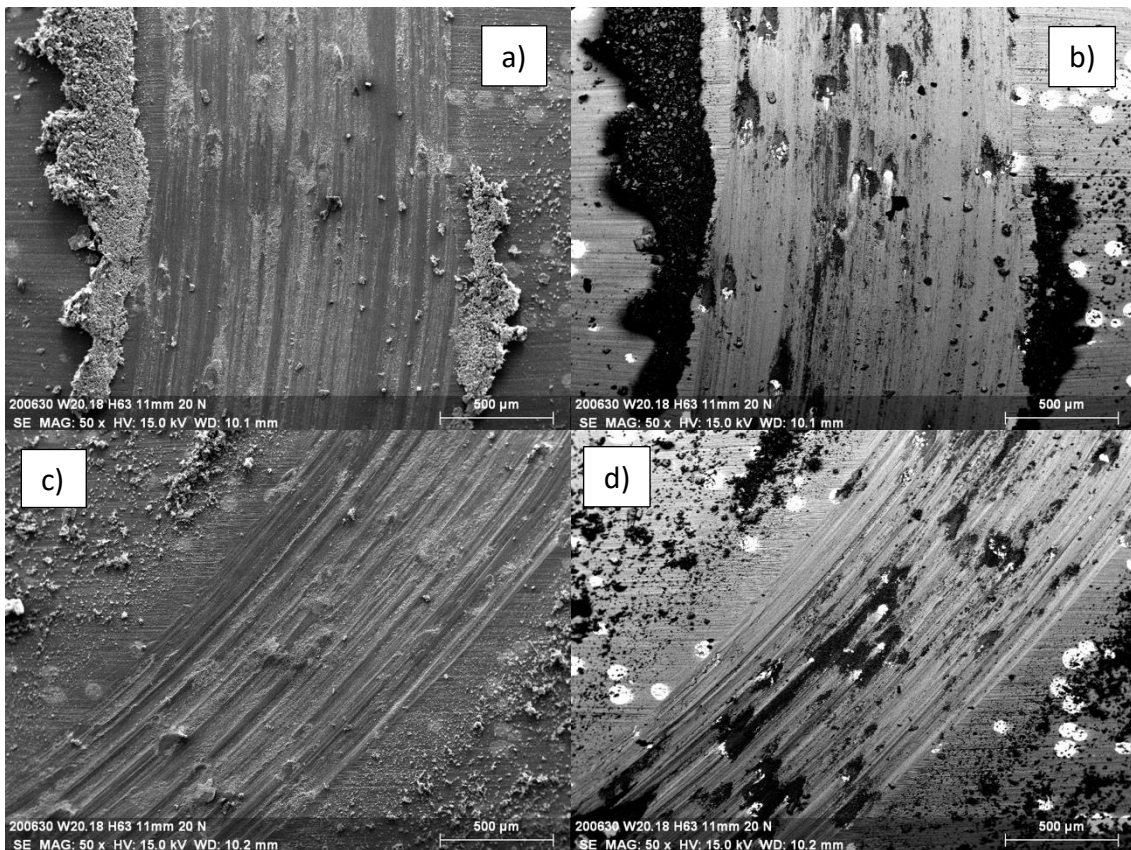


Figure 96. Track overview in different areas in both a) & c) in SE mode and b) & d) in BSE mode

The debris amount generated is elevated, with variations on the size with lot of combinations of coarse and fine debris (Figure 97). The stacked material in front of the carbides also increases a lot, and the grooves observed are deeper, wider and longer as the high load causes a high abrasion.

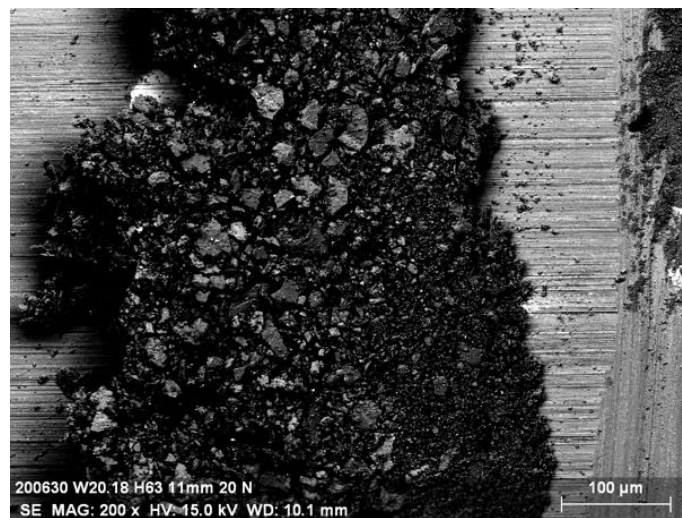


Figure 97. Coarse and fine debris on W20.18 H6.3 11mm track side

## 5 DISCUSSION

### 5.1 Influence of the counterpart on the wear behavior

All tests done lead to an understanding of the general wear behavior of the 316L + 20% WC manufactured by additive manufacturing and what of the role played by the counter body in this behavior. The previous work of [1] serves as a reference in order to assess the influence of the counter body on the wear behavior of this complex composite. Taking into account all the data and information obtained, this section will consider how the material behaves against a WC ball as counter body.

Worn volume and wear rate will be analyzed first since their tendencies were different depending on the height of the surface (section 4.3.2.1). Indeed, H and F faces were used in this study since a previous work highlighted that the wear behavior of this composite against alumina was independent to the height of the surface tested [2]. CoF variation for H (Figure 56, Figure 58, Figure 59, Figure 61) and F faces was similar (Figure 57, Figure 60), but in some parts presented some differences. Furthermore, SEM observations have shown similar wear features at the two considered heights. As observed in section 4.3.2.1, the wear rates of the two heights exhibit different trend (Figure 72). Tests at 6.3mm from the substrate tend to have higher wear rates and to stabilize at longer sliding distances. Instead, tests at 1.3mm from the substrate exhibit an initial high wear rate and then stabilize at longer sliding distances with a value similar to the wear rate of [1], where oxidative wear occurs and a tribolayer was formed, protecting the track. Indeed, the length of the first continuous increase of CoF is longer for the tests at 6.3mm (Figure 57, Figure 59, Figure 60 and Figure 61): unknown for W20.18 H6.3 11mm (as the test was stopped before the drop), ~7000 laps for W20.15 H.6.3 8mm and ~11000 laps for W20.18 H6.3 8mm, whereas ~5800 laps for W20.15 F1.3 11mm and ~7000 laps for W20.15 F1.3 8mm. This first continuous increase of CoF is the most severe wear stage in both surfaces.

Considering the differences observed in the CoF variations (section 4.3.1) and these different trends, the two different heights will be considered separately. The microstructural differences observed in [86] at different heights and the use of the two different counterpart are the two main factors.

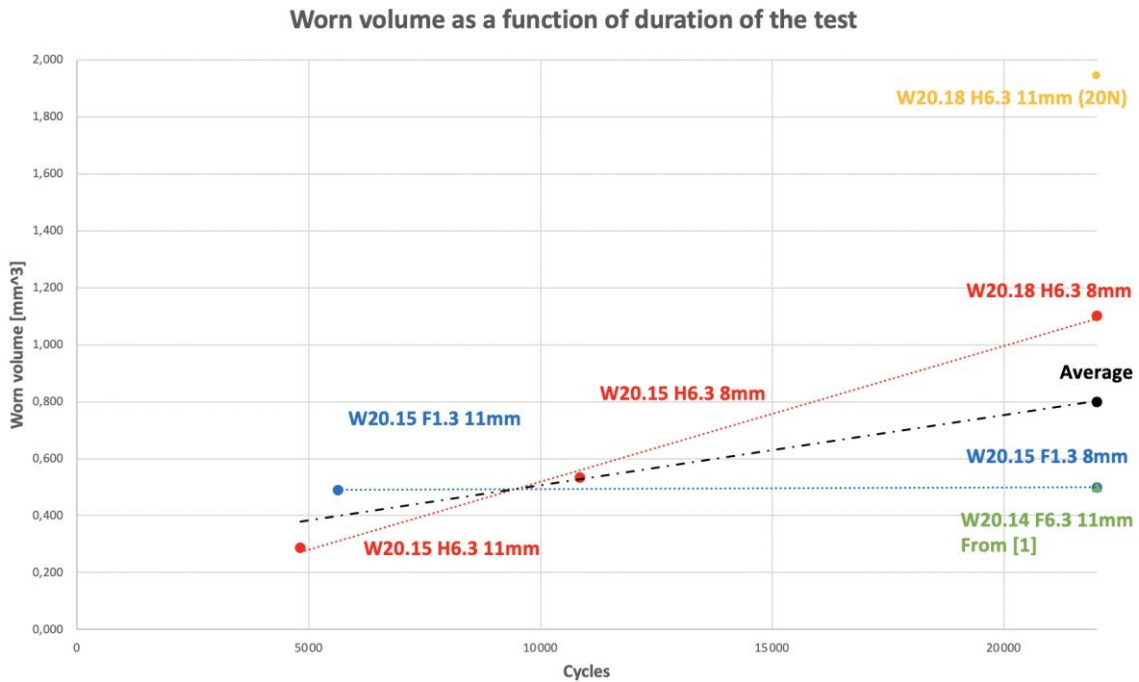


Figure 98. Worn volume as a function of the duration of the test, with D. Mario's uninterrupted test [1] (W20.14 F6.3 11mm)

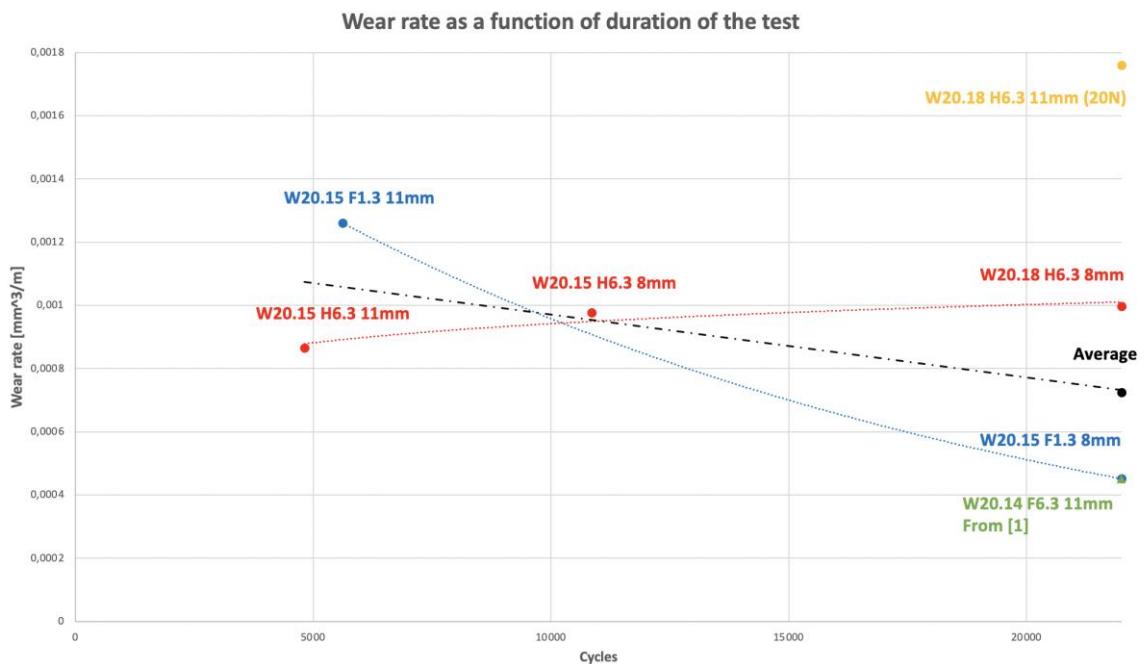


Figure 99. Wear rate as a function of the duration the test, with D. Mario's uninterrupted test [1] (W20.14 F6.3 11mm)

- The main difference is the counter body material. Even though WC and alumina have nearly a similar hardness value (alumina is harder), alumina ( $\text{Al}_2\text{O}_3$ ) is an oxide and thus might lead to a higher enrichment of the tribolayer. That extra oxidized element allows to a faster and more compact tribolayer formation and much more stable oxidative wear stages. Moreover, the alumina ball is highly worn in comparison to the WC due to the mechanical locking or adhesion between WC carbides and ball. This mechanical locking on the WC carbides (Figure 75, Figure 77, Figure 80, Figure 82, Figure 93) decreases the local contact stresses since the contact area increases and the amount of debris is increased in the track [1]. The decrease of the contact stresses leads to a decrease of the delamination occurrence and the high quantity of debris can form a stable tribolayer. On the other hand, WC ball is poorly worn (Table 9), even if the same mechanical locking is observed on the WC carbides of the microstructure. Since the WC ball is not an oxide, its debris is less effective in the formation of a tribolayer. Eventually, the contact area during the tests increases due to the formation of the worn track (Figure 75, Figure 77, Figure 79, Figure 81, Figure 82, Figure 88) and delamination decreases as well in the case of the WC ball. The decrease of the contact stresses allows the stabilization of a tribolayer, but after severe wear at the beginning of the test (Figure 79, Figure 85, Figure 86, Figure 91).
- As mentioned, pin-on disc tests against alumina ball produce a high amount of debris and a high abrasion of the ball itself in contact with the WC carbides. Both phenomena decrease the wear of the 316L+WC due to the enrichment and then formation of a protective tribolayer independently to the height of the surface tested [2]. On the other hand, pin-on-disc tests against WC ball exhibit the same wear phenomena, but with different protective results and thus the microstructural differences (Figure 46, Figure 53) have a higher influence on the wear behavior. The different wear behavior will be further discussed in 5.2.

## 5.2 Elucidation of the wear sequence

Taking into account section 5.1 and the results of section 4, the wear behavior for both faces will be elucidated. Although similar behaviors are observed, different considerations are needed for a better understanding of the composite. As reported in [86], the microstructure of the 316L+20%WC at 1.3mm of distance from the substrate is more heterogeneous in comparison to the microstructure at 6.3mm due to an homogenization effect. WC carbides are well-dispersed in a reinforced austenitic matrix in both heights, but at 1.3mm the matrix is less reinforced by solidification carbides and it is more similar to the clad 316L microstructure [40,86]. On the other hand, at 6.3mm the matrix exhibits an almost continuous network of solidification carbides. The wear resistance of the two matrices is differentiated by the pin-on disc tests against WC ball. Indeed, Figure 50a shows the differences among the first three layers: almost no WC carbides in the first layer (having almost pure deposited 316L), full of WC carbides in the second layer and a stabilization of the powder stream on the third one. Instead, Figure 50b exhibits a more homogeneous microstructure in layers further from the substrate.

### **F faces tests**

The microstructure of the F1.3 face corresponds to the third layer (Figure 50a). Tribometer results of tests carried out at this height (Figure 57 and Figure 60) show a similar main drop of the CoF at 5000-6000 laps, without other variations as observed for H faces (Figure 56, Figure 59, Figure 61). Consequently, based on previous studies and the observations of section 4.3.3, the behavior for F faces can be distinguished in 3 parts.

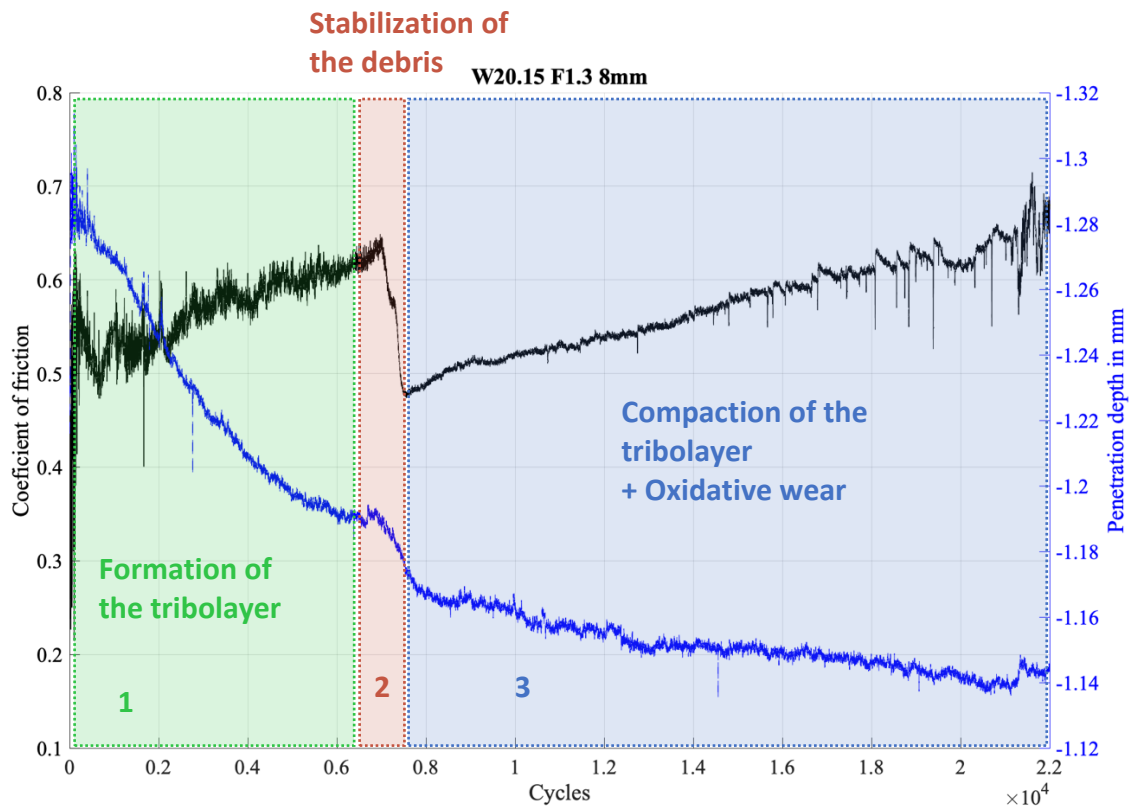


Figure 100. Wear sequence for F faces (Based on W20.15 F1.3 8mm and W20.15 F1.3 11mm)

- 1) The early peak of stage 1, common to both tests, is associated to adhesive wear [89] as at the begin of the test, the first track is created and the surface initial roughness is erased. Later on, debris starts to stack in front of the WC carbides by an adhesive mechanism (Figure 93). After this CoF variability, the system reaches a stable and continuous increase of the CoF, while the penetration depth increases. The debris from the previous wear mechanisms oxidizes in contact with the air and spreads throughout the whole track. As observed in [1], this initial increase of CoF associated with a continuous decrease of the penetration depth is associated to debris that starts to accumulate in certain parts of the track and starts to act as protection (Figure 79). This accumulation of debris may be associated to the first stages of the tribolayer formation. However, the tribolayer could not be seen, mainly because the F test was stopped at this stage. H faces, as it will be explained later, show this same early behavior, and tribolayer signs could be observed, as seen in Figure 78.



- 2) The CoF suddenly drops into a much lower value. Penetration depth remains constant during a short time just before the drop, and after the drop it decreases with a higher slope until the CoF drop finishes. The increase on the penetration depth happening just before the CoF drops is associated to the stabilization of the debris as tribolayer (Figure 79 and Figure 80). The different noise of the two continuous rises (before and after the CoF drop) exhibits a change of the surface conditions as well.
  
- 3) After the main drop, the penetration depth continues to decrease, but it shows constant values in some sections in this last stage. The third stage is associated to the compaction of the tribolayer with mild wear, as shown by the small decrease of the penetration depth. Based on literature, this is due to oxidative wear [57,58]. The tribolayer compacts with the progress of the test and the higher values of CoF represents the higher strain of the tribolayer (Figure 95). In this stage, abrasive wear occurs as well in some parts of the track, as grooves are observed along with plastic delamination (Figure 93). Holes in front of the carbides were also observed, thus reckoning that the debris which do not contribute to the tribolayer starts to act as a 3-body abrasive particle (Figure 94). The wear volume is relatively low since the tribolayer protects both ball and specimen, as it is shown in Figure 71 and in Table 8: worn volume is practically similar while having a difference of 17000 laps.

## H faces tests

Based on this three tribometer results obtained and the SEM observations, the wear sequence for H faces can be assessed, dividing it in 6 stages.

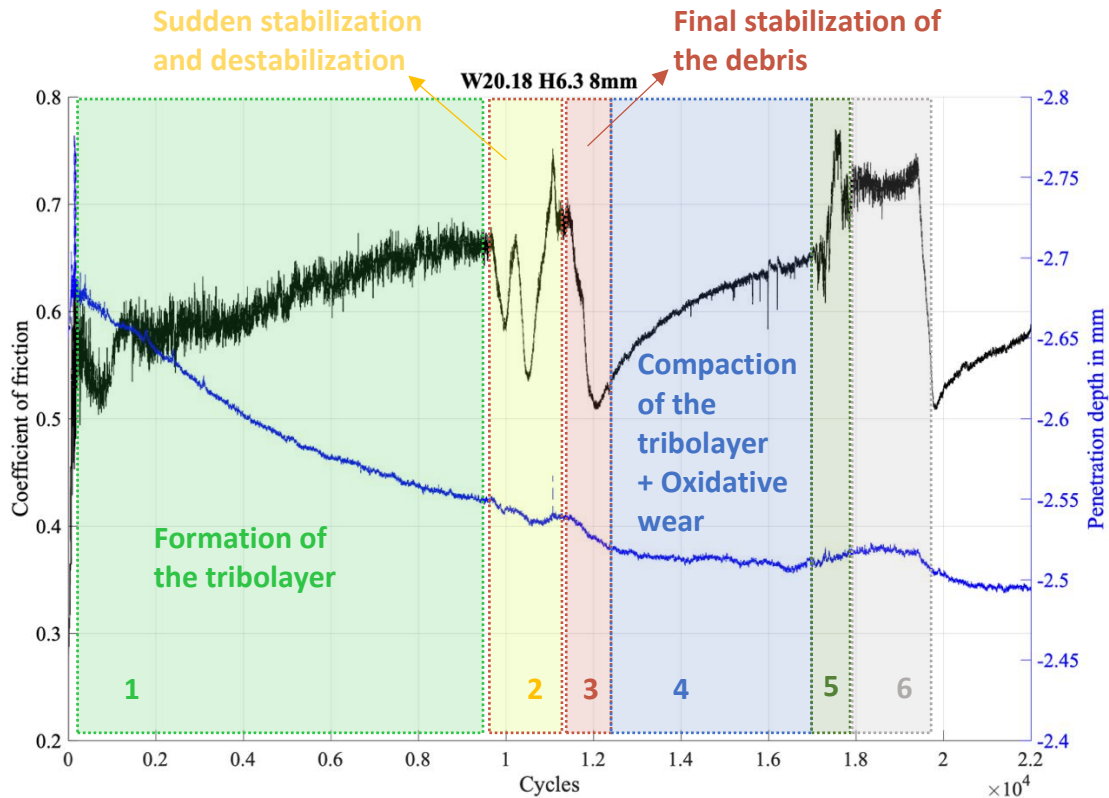


Figure 101. Wear sequence for H faces (Based on W20.15 H6.3 11mm, W20.15 H6.3 8mm and W20.18 H6.3 8mm)

- 1) As already mentioned, the first stage is considered the same for both F and H faces due to the similar CoF and penetration depth evolutions. Indeed, SEM observations show similar features. In this stage, the track is created and initial roughness erased, with first starts of the adhesive wear [89] being presented. Early plastic deformation, which cause delamination, is observed as well with higher occurrence than the 1.3 height due to the solidification carbide presence (Figure 78). Indeed, generally, tests at 6.3mm of height exhibit higher wear rates (Figure 72). This first signs of plastic deformations also cause the MML creation along with the first signs of tribolayer formation (Figure 76 and Figure 78). Fragments of solidification carbides here can enrich the MML and thus increase its strength and the resistance from abrasion. Nevertheless, a high carbide

presence increases the abrasion resistance, but it may decrease the formation of oxidized debris that then enrich the protective oxide layer. Abrasive wear in this first stage is more between abrasive particles belonging to the ball and the intrinsic roughness of the surface, as first shallow and short grooves are observed (Figure 75 and Figure 77).

- 2) Before the main CoF drop, as observed at 1.3mm height, CoF exhibits several sudden variations and then it recovers to the same continuous CoF rise. This variability is caused by the stabilization of the tribolayer, but the latter is not stable due to the oxides that compose it or due to its heterogeneities. SEM observation could not be stopped in this destabilization, but the interruption in the W20.15 F1.3 11mm shows how the oxidized debris is stabilized by SEM observations (Figure 79 and Figure 80). This stage finishes with the formation of either further debris or more homogeneity of the tribolayer on the track.
- 3) Final stabilization occurs with the last main drop of the CoF. This is observable on the penetration depth as well, with the same behavior as in F faces: it increases and just after the drop decreases. The debris is pushed down onto the matrix and its compaction starts. This drop (2<sup>nd</sup> point of interest) of the CoF occurred in different durations of H tests, but they lasted more compared to F faces tests: unknown for W20.15 H6.3 11mm, ~7000 laps for W20.15 H6.3 8mm and ~11000 laps for W20.18 H6.3 8mm; and ~5800 laps for W20.15 F1.3 11mm and ~7000 laps for W20.15 F1.3 8mm.
- 4) The compaction of the tribolayer happens during this stage with a lower noise of the CoF, as in F faces. The constant penetration depth suggest oxidative wear to occur, as the debris compacting gets oxidized and forms a more spread and compact tribolayer (Figure 84, Figure 85 and Figure 86). Indeed, with the progress of the test, the wear rates stabilize for the H faces as well. The tribolayer is protecting the surface at this stage.

- 5) Based on [1], tribolayer breaks down. The previous compaction of the tribolayer reaches a threshold limit in thickness and strain [57,90] causing it to break. The breakage is not uniform along the whole track, causing high noise of the CoF.
  
- 6) Abrasive particles coming from the tribolayer breakdown abrade the surface and the CoF increases, as the ball is in contact with the surface. This is associated to three-body abrasion, as longer and deeper grooves appear on the surfaces. Moreover, the holes where stacked material used to be are also observed, and contribute to this abrasion mechanism. Meanwhile, the penetration depth in this stage is almost constant. The quantity of debris formed in this stage is high. It oxidizes and the formation of the tribolayer restarts. This stage ends with a final drop on the CoF to the same value as the one observed after the first drop, corresponding to the stabilization of a new tribolayer. The wear behavior now restarts in loop from 4).

## 6 CONCLUSIONS

The final goal of this study was to determine how the counter body influences the wear behavior of a laser clad 316L + 20% WC composite, based on previous works [1,2]. Several pin-on-disc wear tests were carried out to assess the wear behavior of the composite and recognize the differences among the previous works. The composite was microstructurally characterized and passed through a Vickers microhardness test. In that respect, it has been shown that:

- Confirming previous studies [2,86], samples have different carbide quantity and thus a different microstructure considering where the sample is grinded for wear tests. Consequently, there are differences in mechanical properties between these different heights due to the heat accumulation during fabrication of the deposit.
- These microstructural variations and thus different mechanical properties lead to discrepancies of the wear behaviors as function of the distance from the substrate. WC counter body ball is capable to enhance these differences due to its nature and behavior in contact with the complex microstructure of the 316L+WC composite. On the other hand, alumina ball hid these microstructural differences since it depends to highly enrich the tribolayer during pin-on disc test [2].
- Microstructures at 1.3mm from the substrate have a similar wear behavior to the one observed in [1], where alumina was used as counter body, since the tests reach the stabilization of the tribolayer in short time and the wear rates decrease at the increase of the sliding distance. On the other hand, samples at 6.3mm from the substrate show different wear behavior with more variability of the CoF. The differences are due to the different reinforced matrix and a high carbide presence may create more resistance to abrasion, but less tendency to form oxidized debris for the tribolayer enrichment. However, both surfaces showed

similar wear patterns (adhesion, plastic deformation, two- and three-body abrasion, cracked carbides).

## 7 PERSPECTIVES

The usage of 316L+WC composite fabricated by laser cladding do have better wear performance than the pure 316L. The flexibility that a widely used steel combined with the WC particles reinforcement allows better performances on parts. The reinforcement acts protecting the parent steel and the wear is significantly improved, particularly if WC is used as counterpart, having less wear volume for both counter-body and samples.

Firstly, further tests need to be carried out to confirm this thesis result, hence confirm if there is different wear behavior depending on the height of the sample being tested. Furthermore, it would be interesting to check results in different heights between tests using alumina and WC as counterparts, since the results reported in [1] are at the same height. The MML observation this work has reported is not complete so cross section cuts would be reasonable to be made if reproducibility is achieved in newer tests made with WC as counter body. In addition, higher concentration of WC in samples will be an attractive new area to research.

These tests were performed at room temperature, so high temperature tests would be very viable in order to put parts in the same conditions they could withstand in many industrial applications.

## 8 REFERENCES

- [1] D. Mario, Room temperature wear behavior of laser clad 316L + WC composite coating, Université de Liège, 2019.
- [2] M. Nordera, Correlation between wear properties and microstructure of the 316L + 10 % WC composite, Université de Liège, 2020.
- [3] D. Herzog, V. Seyda, E. Wycisk, C. Emmelmann, Additive manufacturing of metals, *Acta Mater.* 117 (2016) 371–392.  
<https://doi.org/10.1016/j.actamat.2016.07.019>.
- [4] E. Toyserkani, A. Khajepour, S. Corbin, *Laser Cladding*, 1st ed., CRC Press, 2005.
- [5] C. Qiu, M. Al Kindi, A.S. Aladawi, I. Al Hatmi, A comprehensive study on microstructure and tensile behaviour of a selectively laser melted stainless steel, *Sci. Rep.* 8 (2018) 1–16. <https://doi.org/10.1038/s41598-018-26136-7>.
- [6] W.E. Frazier, Metal additive manufacturing: A review, *J. Mater. Eng. Perform.* 23 (2014) 1917–1928. <https://doi.org/10.1007/s11665-014-0958-z>.
- [7] V. Petrovic, R. Niñerola, Powder recyclability in electron beam melting for aeronautical use, *Aircr. Eng. Aerosp. Technol.* 87 (2015) 147–155.  
<https://doi.org/10.1108/AEAT-11-2013-0212>.
- [8] M. Galati, L. Iuliano, A literature review of powder-based electron beam melting focusing on numerical simulations, *Addit. Manuf.* 19 (2018) 1–20.  
<https://doi.org/10.1016/j.addma.2017.11.001>.
- [9] L.A. Dobrzanski, A.D. Dobrzanska-Danikiewicz, A. Achteлик-Franczak, L.B. Dobrzanski, M. Szindler, T.G. Gawel, Porous Selective Laser Melted Ti and Ti6Al4V Materials for Medical Applications, *Powder Metall. - Fundam. Case Stud.* (2017). <https://doi.org/10.5772/65375>.
- [10] J.E. Ruiz, M. Cortina, J.I. Arrizubieta, A. Lamikiz, Study of the influence of shielding gases on Laser Metal Deposition of Inconel 718 superalloy, *Materials (Basel)*. 11 (2018). <https://doi.org/10.3390/ma11081388>.
- [11] K. Zhang, W. Liu, X. Shang, Research on the processing experiments of laser metal deposition shaping, *Opt. Laser Technol.* 39 (2007) 549–557.  
<https://doi.org/10.1016/j.optlastec.2005.10.009>.



- [12] R.M. Mahamood, E.T. Akinlabi, M. Shukla, S. Pityana, Laser metal deposition of Ti6Al4V: A study on the effect of laser power on microstructure and microhardness, *Lect. Notes Eng. Comput. Sci.* 2203 (2013) 994–999.
- [13] D. Novichenko, A. Marants, L. Thivillon, P. Bertrand, I. Smurov, Metal matrix composite material by direct metal deposition, *Phys. Procedia.* 12 (2011) 296–302. <https://doi.org/10.1016/j.phpro.2011.03.038>.
- [14] T. Petrat, B. Graf, A. Gumenyuk, M. Rethmeier, Laser metal deposition as repair technology for a gas turbine burner made of inconel 718, *Phys. Procedia.* 83 (2016) 761–768. <https://doi.org/10.1016/j.phpro.2016.08.078>.
- [15] J.I. Arrizubieta, J.E. Ruiz, S. Martinez, E. Ukar, A. Lamikiz, Intelligent nozzle design for the Laser Metal Deposition process in the Industry 4.0, *Procedia Manuf.* 13 (2017) 1237–1244. <https://doi.org/10.1016/j.promfg.2017.09.043>.
- [16] R.M. Mahamood, E.T. Akinlabi, Effect of Laser Power and Powder Flow Rate on the Wear Resistance Behaviour of Laser Metal Deposited TiC/Ti6Al4V Composites, *Mater. Today Proc.* 2 (2015) 2679–2686. <https://doi.org/10.1016/j.matpr.2015.07.233>.
- [17] G.K.L. Ng, A.E.W. Jarfors, G. Bi, H.Y. Zheng, Porosity formation and gas bubble retention in laser metal deposition, *Appl. Phys. A Mater. Sci. Process.* 97 (2009) 641–649. <https://doi.org/10.1007/s00339-009-5266-3>.
- [18] R.M. Mahamood, E.T. Akinlabi, Scanning speed and powder flow rate influence on the properties of laser metal deposition of titanium alloy, *Int. J. Adv. Manuf. Technol.* 91 (2017) 2419–2426. <https://doi.org/10.1007/s00170-016-9954-9>.
- [19] S.H. Oliari, A.S.C. Monteiro D’Oliveira, M. Schulz, Additive Manufacturing of H11 with Wire-Based Laser Metal Deposition, *Soldag. e Insp.* 22 (2017) 466–479. <https://doi.org/10.1590/0104-9224/SI2204.06>.
- [20] C.G. Papakonstantinou, P. Balaguru, R.E. Lyon, Comparative study of high temperature composites, *Compos. Part BEngineering.* 32 (2001) 637–649. [https://doi.org/10.1016/S1359-8368\(01\)00042-7](https://doi.org/10.1016/S1359-8368(01)00042-7).
- [21] A.N. Nakagaito, S. Iwamoto, H. Yano, Bacterial cellulose: The ultimate nanoscalar cellulose morphology for the production of high-strength composites, *Appl. Phys. A Mater. Sci. Process.* 80 (2005) 93–97.

- <https://doi.org/10.1007/s00339-004-2932-3>.
- [22] Z. Zheng, B. Xu, L. Huang, L. He, X. Ni, Novel composite of Co/carbon nanotubes: Synthesis, magnetism and microwave absorption properties, *Solid State Sci.* 10 (2008) 316–320. <https://doi.org/10.1016/j.solidstatesciences.2007.09.016>.
- [23] R.L. Deuis, C. Subramanian, J.M. Yellup, Dry sliding wear of aluminium composites - A review, *Compos. Sci. Technol.* 57 (1997) 415–435. [https://doi.org/10.1016/S0266-3538\(96\)00167-4](https://doi.org/10.1016/S0266-3538(96)00167-4).
- [24] UPV-EHU Course notes, *Materiales Estructurales: Comportamiento en Servicio y Mecánica de Fráctura*, 2017.
- [25] K.K. Chawla, *Composite materials*, Springer International Publishing, 2009. <https://doi.org/10.1007/978-0-387-74365-3>.
- [26] M.P. Behera, T. Dougherty, S. Singamneni, Conventional and additive manufacturing with metal matrix composites: A perspective, *Procedia Manuf.* 30 (2019) 159–166. <https://doi.org/10.1016/j.promfg.2019.02.023>.
- [27] M. Yakout, M.A. Elbestawi, Additive Manufacturing of Composite Materials : An Overview, 6th Int. Conf. Virtual Mach. Process Technol. (VMPT), Montréal. (2017) 1–8. <https://doi.org/10.1016/B978-0-12-803581-8.04165-5>.
- [28] L. Dubourg, D. Ursescu, F. Hlawka, A. Cornet, Laser cladding of MMC coatings on aluminium substrate: Influence of composition and microstructure on mechanical properties, *Wear.* 258 (2005) 1745–1754. <https://doi.org/10.1016/j.wear.2004.12.010>.
- [29] J. Nurminen, J. Näkki, P. Vuoristo, Microstructure and properties of hard and wear resistant MMC coatings deposited by laser cladding, *Int. J. Refract. Met. Hard Mater.* 27 (2009) 472–478. <https://doi.org/10.1016/j.ijrmhm.2008.10.008>.
- [30] T. Sourmail, H.K.D.H. Bhadeshia, *Stainless Steels*, Univ. Cambridge. (n.d.). [https://www.phase-trans.msm.cam.ac.uk/2005/Stainless\\_steels/stainless.html](https://www.phase-trans.msm.cam.ac.uk/2005/Stainless_steels/stainless.html) (accessed April 10, 2020).
- [31] 316-316L-317L Specification Sheet, (n.d.). <https://www.sandmeyersteel.com/images/316-316l-317l-spec-sheet.pdf> (accessed April 11, 2020).
- [32] CES Edupack, (2019).

- [33] Q. Fang, W. Bai, J. Yang, X. Xu, G. Li, N. Shi, M. Xiong, H. Rong, Qusongite (WC): A new mineral, *Am. Mineral.* 94 (2009) 387–390.  
<https://doi.org/10.2138/am.2009.3015>.
- [34] A.S. Kurlov, A.I. Gusev, Tungsten carbides and W-C phase diagram, *Inorg. Mater.* 42 (2006) 121–127. <https://doi.org/10.1134/S0020168506020051>.
- [35] A.S. Kurlov, A.I. Gusev, Tungsten Carbides: Structure, Properties and Application in Hardmetals, 2013. <https://doi.org/10.1007/978-3-319-00524-9>.
- [36] A. Levy, A. Miriyev, N. Sridharan, T. Han, E. Tuval, S.S. Babu, M.J. Dapino, N. Frage, Ultrasonic additive manufacturing of steel: Method, post-processing treatments and properties, *J. Mater. Process. Technol.* 256 (2018) 183–189.  
<https://doi.org/10.1016/j.jmatprotec.2018.02.001>.
- [37] A. Saboori, M. Toushekhah, A. Aversa, M. Lai, M. Lombardi, S. Biamino, P. Fino, Critical Features in the Microstructural Analysis of AISI 316L Produced By Metal Additive Manufacturing, *Metallogr. Microstruct. Anal.* 9 (2020) 92–96.  
<https://doi.org/10.1007/s13632-019-00604-6>.
- [38] W. Wang, M. Wang, Z. Jie, F. Sun, D. Huang, Research on the microstructure and wear resistance of titanium alloy structural members repaired by laser cladding, *Opt. Lasers Eng.* 46 (2008) 810–816.  
<https://doi.org/10.1016/j.optlaseng.2008.05.015>.
- [39] M. Ziętała, T. Durejko, M. Polański, I. Kunc, T. Płociński, W. Zieliński, M. Łazińska, W. Stępniewski, T. Czujko, K.J. Kurzydłowski, Z. Bojar, The microstructure, mechanical properties and corrosion resistance of 316 L stainless steel fabricated using laser engineered net shaping, *Mater. Sci. Eng. A.* 677 (2016) 1–10. <https://doi.org/10.1016/j.msea.2016.09.028>.
- [40] A. Yadollahi, N. Shamsaei, S.M. Thompson, D.W. Seely, Effects of process time interval and heat treatment on the mechanical and microstructural properties of direct laser deposited 316L stainless steel, *Mater. Sci. Eng. A.* 644 (2015) 171–183. <https://doi.org/10.1016/j.msea.2015.07.056>.
- [41] K. Saeidi, X. Gao, Y. Zhong, Z.J. Shen, Hardened austenite steel with columnar sub-grain structure formed by laser melting, *Mater. Sci. Eng. A.* (2015).  
<https://doi.org/10.1016/j.msea.2014.12.018>.

- [42] Y. Zhong, L. Liu, S. Wikman, D. Cui, Z. Shen, Intragranular cellular segregation network structure strengthening 316L stainless steel prepared by selective laser melting, *J. Nucl. Mater.* 470 (2016) 170–178.  
<https://doi.org/10.1016/j.jnucmat.2015.12.034>.
- [43] Y.M. Wang, T. Voisin, J.T. McKeown, J. Ye, N.P. Calta, Z. Li, Z. Zeng, Y. Zhang, W. Chen, T.T. Roehling, R.T. Ott, M.K. Santala, P.J. Depond, M.J. Matthews, A. V. Hamza, T. Zhu, Additively manufactured hierarchical stainless steels with high strength and ductility - Supplementary information, *Nat. Mater.* 17 (2018) 63–70.  
<https://doi.org/10.1038/NMAT5021>.
- [44] T. Maurizi Enrici, A. Mertens, M. Sinnaeve, J.T. Tchuindjang, Elucidation of the solidification sequence of a complex graphitic HSS alloy under a combined approach of DTA and EBSD analyses, *J. Therm. Anal. Calorim.* 13 (2019).  
<https://doi.org/10.1007/s10973-019-09093-9>.
- [45] Y. Luan, N. Song, X. Kang, D. Li, A study of the carbides in high-speed steel rolls, *Mater. Sci. Forum.* 638–642 (2010) 3356–3361.  
<https://doi.org/10.4028/www.scientific.net/MSF.638-642.3356>.
- [46] E. Mancini, Studio delle eterogeneità microstrutturali in un rivestimento composito a matrice metallica di acciaio inossidabile 316L e carburo di tungsteno, (2017).
- [47] M. Boccalini, H. Goldenstein, Solidification of high speed steels, *Int. Mater. Rev.* 46 (2001) 92–115. <https://doi.org/10.1179/095066001101528411>.
- [48] P. Ding, G. Shi, S. Zhou, As-cast carbides in high-speed steels, *Metall. Trans. A.* 24 (1993) 1265–1272. <https://doi.org/10.1007/BF02668195>.
- [49] X. Zhou, F. Fang, L.I. Gang, J. Jiang, Morphology and properties of M<sub>2</sub>C eutectic carbides in AISI M2 steel, *ISIJ Int.* 50 (2010) 1151–1157.  
<https://doi.org/10.2355/isijinternational.50.1151>.
- [50] X. Zhou, X. Yin, F. Fang, J. Jiang, W. Zhu, Influence of rare earths on eutectic carbides in AISI M2 high speed steel, *J. Rare Earths.* 30 (2012) 1075–1078.  
[https://doi.org/10.1016/S1002-0721\(12\)60181-1](https://doi.org/10.1016/S1002-0721(12)60181-1).
- [51] S. Liu, Y. Zhou, X. Xing, J. Wang, X. Ren, Q. Yang, Growth characteristics of primary M<sub>7</sub>C<sub>3</sub> carbide in hypereutectic Fe-Cr-C alloy, *Sci. Rep.* 6 (2016) 1–8.

<https://doi.org/10.1038/srep32941>.

- [52] Y.J. Oh, W.S. Ryu, C. Sung, I.H. Kuk, J.H. Hong, Grain boundary filmlike Fe-Mo-Cr phase in nitrogen-added type 316L stainless steels, *J. Mater. Res.* 14 (1999) 390–397. <https://doi.org/10.1557/JMR.1999.0057>.
- [53] T. Maurizi Enrici, O. Dedry, F. Boschini, J. Tchoufang Tchuindjang, A. Mertens, Microstructural and Thermal Characterization of 316L+WC Composite Coatings Obtained by Laser Cladding, *Adv. Eng. Mater.* 13 (2020) 1–12. <https://doi.org/10.1002/adem.202000291>.
- [54] A.W.B. G. W. Stachowiak, Abrasive, Erosive and Cavitation Wear, in: *Eng. Tribol.*, 2014: pp. 525–576. <https://doi.org/10.1016/b978-0-12-397047-3.00011-4>.
- [55] K. Kato, K. Adachi, Wear mechanisms, in: B. Bhusha (Ed.), *Mod. Tribol. Handb.*, CRC Press, 2001: pp. 273–299.
- [56] A.W.B. G. W. Stachowiak, Adhesion and Adhesive Wear, in: *Eng. Tribol.*, 2014: pp. 577–596. <https://doi.org/10.1016/b978-0-12-397047-3.00012-6>.
- [57] A.W.B. G. W. Stachowiak, Corrosive and Oxidative Wear, in: *Eng. Tribol.*, 2014: pp. 597–620. <https://doi.org/10.1016/b978-0-12-397047-3.00013-8>.
- [58] M. Vardavoulias, The role of hard second phases in the mild oxidational wear mechanism of high-speed steel-based materials, *Wear.* 173 (1994) 105–114. [https://doi.org/10.1016/0043-1648\(94\)90262-3](https://doi.org/10.1016/0043-1648(94)90262-3).
- [59] J.M. Challen, L.J. McLean, P.L.B. Oxley, Plastic deformation of a metal surface in sliding contact with a hard wedge: its relation to friction and wear, *Proc. R. Soc. Lond. A. Math. Phys. Sci.* 394 (1984) 161–181.
- [60] A.W.B. G. W. Stachowiak, Fatigue Wear, in: *Eng. Tribol.*, 2014: pp. 621–645. <https://doi.org/10.1016/b978-0-12-397047-3.00014-x>.
- [61] M. Gągol, A. Przyjazny, G. Boczka, Wastewater treatment by means of advanced oxidation processes based on cavitation – A review, *Chem. Eng. J.* 338 (2018) 599–627. <https://doi.org/10.1016/j.cej.2018.01.049>.
- [62] I. Tzanakis, A. Georgoulas, M. Hadfield, N. Kotsovinos, Cavitation erosion damage of scroll steel plates by high-speed gas working fluid, *Int. J. Comput. Methods Exp. Meas.* 2 (2014) 168–183. <https://doi.org/10.2495/CMEM-V2-N2-168-183>.

- [63] C. Donnet, A. Erdemir, Historical developments and new trends in tribological and solid lubricant coatings, *Surf. Coatings Technol.* 180–181 (2004) 76–84.  
<https://doi.org/10.1016/j.surfcoat.2003.10.022>.
- [64] L.J. O'Donnell, G.M. Michal, F. Ernst, H. Kahn, A.H. Heuer, Wear maps for low temperature carburised 316L austenitic stainless steel sliding against alumina, *Surf. Eng.* 26 (2010) 284–292.  
<https://doi.org/10.1179/026708410X12550773057901>.
- [65] S.Q. Wang, L. Wang, Y.T. Zhao, Y. Sun, Z.R. Yang, Mild-to-severe wear transition and transition region of oxidative wear in steels, *Wear.* 306 (2012) 311–320.  
<https://doi.org/10.1016/j.wear.2012.08.017>.
- [66] D. Gu, J. Ma, H. Chen, K. Lin, L. Xi, Laser additive manufactured WC reinforced Fe-based composites with gradient reinforcement/matrix interface and enhanced performance, *Compos. Struct.* 192 (2018) 387–396.  
<https://doi.org/10.1016/j.compstruct.2018.03.008>.
- [67] X. Tong, F.H. Li, M. Kuang, W.Y. Ma, X.C. Chen, M. Liu, Effects of WC particle size on the wear resistance of laser surface alloyed medium carbon steel, *Appl. Surf. Sci.* 258 (2012) 3214–3220. <https://doi.org/10.1016/j.apsusc.2011.11.066>.
- [68] A. Jourani, S. Bouvier, Friction and Wear Mechanisms of 316L Stainless Steel in Dry Sliding Contact: Effect of Abrasive Particle Size, *Tribol. Trans.* 58 (2015) 131–139. <https://doi.org/10.1080/10402004.2014.955229>.
- [69] L. Fan, Y. Dong, H. Chen, L. Dong, Y. Yin, Wear Properties of Plasma Transferred Arc Fe-based Coatings Reinforced by Spherical WC Particles, *J. Wuhan Univ. Technol. Mater. Sci. Ed.* 34 (2019) 433–439. <https://doi.org/10.1007/s11595-019-2070-6>.
- [70] F. Bartolomeu, M. Buciumeanu, E. Pinto, N. Alves, O. Carvalho, F.S. Silva, G. Miranda, 316L stainless steel mechanical and tribological behavior—A comparison between selective laser melting, hot pressing and conventional casting, *Addit. Manuf.* 16 (2017) 81–89.  
<https://doi.org/10.1016/j.addma.2017.05.007>.
- [71] G. jiang Li, Q. Peng, C. Li, Y. Wang, J. Gao, S. yuan Chen, J. Wang, B. luo Shen, Effect of DC plasma nitriding temperature on microstructure and dry-sliding

- wear properties of 316L stainless steel, *Surf. Coatings Technol.* 202 (2008) 2749–2754. <https://doi.org/10.1016/j.surfcoat.2007.10.002>.
- [72] L. Song, G. Zeng, H. Xiao, X. Xiao, S. Li, Repair of 304 stainless steel by laser cladding with 316L stainless steel powders followed by laser surface alloying with WC powders, *J. Manuf. Process.* (2016).  
<https://doi.org/10.1016/j.jmapro.2016.08.004>.
- [73] J. Domitner, M. Aigner, T. Stern, A. Paar, C. Sommitsch, L. Elizondo, Thermomechanical Wear Testing of Metal Matrix Composite Cladding for Potential Application in Hot Rolling Mills, *Steel Res. Int.* 1900478 (2019).  
<https://doi.org/10.1002/srin.201900478>.
- [74] CSM Instruments, CSM Technical Features - HIGH TEMPERATURE TRIBOMETER (THT), (n.d.).
- [75] V. Saikko, A multidirectional motion pin-on-disk wear test method for prosthetic joint materials, *J. Biomed. Mater. Res.* 41 (1998) 58–64.  
[https://doi.org/10.1002/\(SICI\)1097-4636\(199807\)41:1<58::AID-JBM7>3.0.CO;2-P](https://doi.org/10.1002/(SICI)1097-4636(199807)41:1<58::AID-JBM7>3.0.CO;2-P).
- [76] B.Y. Peng, X. Nie, Y. Chen, Effects of surface coating preparation and sliding modes on titanium oxide coated titanium alloy for aerospace applications, *Int. J. Aerosp. Eng.* 2014 (2014). <https://doi.org/10.1155/2014/640364>.
- [77] A. Iakovlieva, H. Kuszewski, O. Vovk, S. Boichenko, K. Lejda, M. Jakubowski, Experimental study on antiwear properties for blends of jet fuel with bio-components derived from rapeseed oil, *Eastern-European J. Enterp. Technol.* 5 (2015) 20. <https://doi.org/10.15587/1729-4061.2015.51682>.
- [78] T. Miyajima, Y. Tanaka, Y. Iwai, Y. Kagohara, S. Haneda, S. Takayanagi, H. Katsuki, Friction and wear properties of lead-free aluminum alloy bearing material with molybdenum disulfide layer by a reciprocating test, *Tribol. Int.* 59 (2013) 17–22.  
<https://doi.org/10.1016/j.triboint.2012.07.017>.
- [79] F. Alam, A. Kumar, A.K. Patel, R.K. Sharma, K. Balani, Processing, Characterization and Fretting Wear of Zinc Oxide and Silver Nanoparticles Reinforced Ultra High Molecular Weight Polyethylene Biopolymer Nanocomposite, *Jom.* 67 (2015) 688–701. <https://doi.org/10.1007/s11837-015->

1358-z.

- [80] Höganäs, (2020). <https://www.hoganas.com> (accessed May 5, 2020).
- [81] STRUERS, (2020). [www.struers.com](http://www.struers.com) (accessed May 9, 2020).
- [82] Olympus Corporation, Olympus BX Series, (n.d.).
- [83] Alicona Imaging GmbH, Alicona Focus-Variation, (n.d.).  
<https://www.alicon.com/en/focus-variation/> (accessed May 9, 2020).
- [84] Alicona Imaging GmbH, Alicona InfiniteFocus G5 plus, (n.d.).  
<https://www.alicon.com/en/products/infinitefocus/> (accessed May 9, 2020).
- [85] EMCO Test Prüfmaschinen GmbH, EMCO Test M1C010/M1C100, (2005).
- [86] T.M. Enrici, O. Dedry, D. Mario, H. Paydas, J. Tchoufang, A. Mertens, Mechanical properties of multiple-layer 316L + WC composite deposit fabricated by directed energy deposition: Influence of heat accumulation, *Submitt. to Addit. Manuf.* (n.d.).
- [87] J. Li, Z. Zhao, P. Bai, H. Qu, M. Liang, H. Liao, L. Wu, P. Huo, Tribological behavior of TiC particles reinforced 316Lss composite fabricated using selective laser melting, *Materials (Basel)*. 16 (2019). <https://doi.org/10.3390/ma12060950>.
- [88] A. Lanzutti, E. Marin, K. Tamura, T. Morita, M. Magnan, E. Vaglio, F. Andreatta, M. Sortino, G. Totis, L. Fedrizzi, High temperature study of the evolution of the tribolayer in additively manufactured AISI 316L steel, *Addit. Manuf.* 34 (2020) 101258. <https://doi.org/10.1016/j.addma.2020.101258>.
- [89] L.J.O. Donnell, *Tribology of 316L Austenitic Stainless Steel*, 2010.
- [90] A. Kapoor, F.J. Franklin, Tribological layers and the wear of ductile materials, *Wear*. 245 (2000) 204–215. [https://doi.org/10.1016/S0043-1648\(00\)00480-4](https://doi.org/10.1016/S0043-1648(00)00480-4).